Tampere University

ANTTI T. AHO

# Monolithically Integrated Wavelength Locked and High-Brightness Laser Diodes

Tampere University Dissertations 517

Tampere University Dissertations 517

ANTTI T. AHO

# Monolithically Integrated Wavelength Locked and High-Brightness Laser Diodes

ACADEMIC DISSERTATION
To be presented, with the permission of
the Faculty of Engineering and Natural Sciences
of Tampere University,
for public discussion in the lecture room S2
of the Sähkötalo building, Korkeakoulunkatu 3, Tampere,
on 4 December 2021, at 12 o'clock.

ACADEMIC DISSERTATION
Tampere University, Faculty of Engineering and Natural Sciences
Finland

| | | |
|---|---|---|
| *Responsible supervisor and Custos* | Professor Mircea Guina<br>Tampere University<br>Finland | |
| *Supervisor* | Adjunct Professor Jukka Viheriälä<br>Tampere University<br>Finland | |
| *Pre-examiners* | Professor Stephen Sweeney<br>University of Surrey<br>United Kingdom | Professor Panja-Riina Luukka<br>Lappeenranta University of Technology<br>Finland |
| *Opponent* | Professor Matthieu Roussey<br>University of Eastern Finland<br>Finland | |



Cover design: Roihu Inc.

ISBN 978-952-03-2202-1 (print)
ISBN 978-952-03-2203-8 (pdf)
ISSN 2489-9860 (print)
ISSN 2490-0028 (pdf)
http://urn.fi/URN:ISBN:978-952-03-2203-8

PunaMusta Oy – Yliopistopaino
Joensuu 2021

# PREFACE

This thesis is the result of the work carried out by the author as a part of a research group at Optoelectronics Research Centre (ORC), formerly Tampere University of Technology and currently Tampere University, from 2016 to 2020, and in part going back even further. I wish to acknowledge the financial support in context of the research projects 3D-LIDAR, EyeLase, RangeImager and FP7 ECSEL DENSE by Business Finland, Academy of Finland, and the European Union, and personal financial support from HPY Research Foundation, Finnish Foundation for Technology Promotion, KAUTE Foundation, Emil Aaltonen's Foundation, and Jenny and Antti Wihuri Foundation.

Great colleagues were the most important aspect that made ORC a good place to work. I would like to thank my supervisor Prof. Mircea Guina for the opportunity to work with semiconductor lasers, and my instructor Adj. Prof. Jukka Viheriälä for his extremely thorough and hands-on support with writing this thesis, the publications included in it, and in general most of the work that I've ever done at ORC since 2009. I'm also grateful to my colleagues Dr. Topi Uusitalo and Dr. Heikki Virtanen for both academic peer support and friendship in general. A special thanks goes to the support staff who've kept the machines running and samples in order even with limited resources: M.Sc. Ilkka Hirvonen, M.Sc. Mervi Koskinen, M.Sc. Jarno Reuna, Ms. Maija Karjalainen, Ms. Mariia Bister, and Mr. Bengt Pena Holmström, to name a few. Dr. Antti Härkönen had always good advice to give on virtually any field of engineering when problems presented themselves. There's also a surprising amount of paperwork and bureaucracy involved with working in the university setting, and Mrs. Anne Viherkoski, Mrs. Marketta Myllymäki, and Mrs. Eija Heliniemi were of invaluable help in cutting through the red tape. Mr. Timo Lindqvist and others from the physics workshop crafted and modified dozens of mechanical parts for research with micrometre precision. Out of my fellow master's and doctoral students especially M.Sc. Riku Isoaho, M.Sc. Heidi Tuorila, and

M.Sc. Joel Salmi have provided crucial peer support to keep the motivation up during the years. Many nutritious lunches, often involving fish, were had with Ilkka, Dr. Turkka Salminen, and Adj. Prof. Antti Tukiainen, and many great games of badminton and/or floorball were played with Dr. Sanna Ranta and others from Suliszät and Hokizät.

Finally, I'd like to thank my parents for their support and guidance throughout my life, as well as dear Oona, my friends, and everyone else who has been important to me over the years for balancing my life with something more important than the academia and work.

Turku, August 2021
Antti Aho

# ABSTRACT

This thesis presents the fabrication and characterization of high brightness laser diodes with monolithically integrated wavelength locking. The work focuses on two wavelength ranges, 1.5 μm and 1.18 μm, relevant to specific application targets. The lasers emitting around 1.5 μm are primarily aimed at eye-safe LIDAR (*li*ght *d*etection *a*nd *r*anging, a group of 3D scanning technologies) applications. 1.18 μm wavelength region is important for frequency doubling into yellow–orange wavelength range. These wavelengths have especially medical applications and are practically unreachable with direct emission using current semiconductor material technology.

Application requirements are approached using two component variants: tapered distributed Bragg reflector laser diodes (tapered DBR-LDs) and broad area DBR-LDs. In both variants, the wavelength locking DBR element is integrated monolithically on the same chip as the active region, enabling smaller component assembly footprints and cost-effective fabrication. Tapered DBR-LDs comprise three sections: tapered mode expansion and power amplification section, ridge waveguide section providing lateral mode filtering, and DBR grating section providing longitudinal mode filtering. Broad area DBR-LDs comprise wide active region and DBR grating. The tapered design provides better beam quality for the applications where a Gaussian beam is required, while the broad area design provides higher output power and easier device operation with a reduced beam quality.

1.18 μm tapered DBR-LDs reached a continuous wave (CW) output power of 4.04 W, while 1.5 μm tapered and broad area DBR-LDs reached pulsed peak output powers of 4.6 W and 6.1 W, respectively. Wavelength locking reduced temperature change induced wavelength drift to 0.1 nm/°C and spectral full width at half-maximum to 0.3 nm or below. The results are compared quantitatively to results published by others. At the time of publication, these results progressed the state of the art in their own respective categories and have served as the stepping stone for further research and results in the field of high-brightness, wavelength locked lasers.

# TIIVISTELMÄ

Tämä väitöskirja esittelee tutkimustuloksia monoliittisesti aallonpituuslukittujen suuren kirkkauden laserdiodien valmistuksesta ja karakterisoinnista. Tutkimuksen aiheena on kahdella sovelluskohteiden mukaan valitulla aallonpituusalueella, 1,5 μm ja 1,18 μm, toimivat laserdiodit. Aallonpituusalueen 1,5 μm laserdiodit on suunnattu erityisesti silmäturvallisiin LIDAR-sovelluksiin (*li*ght *d*etection *a*nd *r*anging, "valotutka", joukko erilaisia 3D-skannausteknologioita). Aallonpituuden 1,18 μm diodit ovat tärkeitä taajuuskahdennettuja kelta–oransseja lasereita varten, joita käytetään erityisesti lääketieteellisissä sovelluksissa. Näitä aallonpituuksia on hyvin vaikeaa tuottaa diodilaserin suoralla emissiolla käytössä olevien puolijohdemateriaalien ominaisuuksien vuoksi, ja taajuuskahdennuksella tätä rajoitusta saadaan kierrettyä.

Sovellusvaatimusten täyttämiseksi on tutkittu kahta erilaista laserdiodiarkkitehtuuria, kapenevia hajautetun Braggin peilin lasereita (kapeneva DBR) ja leveitä hajautetun Braggin peilin lasereita (leveä DBR). Molemmissa komponenttityypeissä hajautettu Braggin peili on liitetty sirun aktiiviseen alueeseen monoliittisesti, jolloin laseria komponenttina käyttävistä järjestelmistä saadaan pienikokoisempia ja järjestelmien valmistus on edullisempaa. Kapenevat DBR-laserit koostuvat kolmesta osasta: kolmiomaisesta optisen moodin laajennusosasta, harjanneaaltojohdeosasta, joka suodattaa pois korkeampia poikittaisia moodeja, ja hajautetusta Braggin peilistä, joka valitsee yhden pitkittäisen optisen moodin. Leveissä DBR-lasereissa on leveä aktiivialue sekä hajautettu Braggin peili. Kapenevissa DBR-lasereissa on parempi säteenlaatu sellaisia sovelluksia varten, joissa tarvitaan Gaussista lasersädettä, kun puolestaan leveissä DBR-lasereissa on suurempi teho, helpompi käytettävyys ja huonompi säteenlaatu.

1,18 μm laserit tuottivat suurimmillaan 4,04 W tehon. Kapenevat ja leveät 1,5 μm DBR-laserit tuottivat parhaimmillaan 4,6 W ja 6,1 W tehon. Aallonpituuslukitus vähensi lämpötilan muutoksesta johtuvan aallonpituussiirtymän arvoon 0,1 nm/°C ja spektrin puoliarvonleveyden arvoon 0,3 nm tai sen alle. Väitöskirjan tuloksia ver-

taillaan kvantitatiivisesti muiden julkaisemiin tuloksiin. Julkaisuaikanaan nämä tulokset edustivat alansa huippua ja ovat sittemmin johtaneet uuteen tutkimukseen ja tuloksiin korkeatehoisten, aallonpituuslukittujen laserien saralla.

# CONTENTS

## *List of Figures*

## *List of Tables*

# ABBREVIATIONS

| | |
|---|---|
| AR | antireflection (coating), a coating designed to reduce the reflectance of an interface at a certain wavelength range |
| BA-LD | broad-area laser diode, a diode laser that is laterally multi-mode |
| BPP | beam parameter product |
| COD | catastrophic optical damage |
| CW | continuous wave (as opposed to pulsed) |
| DBR | distributed Bragg reflector, a structure providing periodic feedback |
| DBR-LD | distributed Bragg reflector laser diode, a diode laser utilizing a DBR grating |
| DC | duty cycle |
| DFB | distributed feedback |
| DFB-LD | distributed feedback laser diode |
| EDFA | erbium-doped fiber amplifier |
| FF | far field, the emission angle distribution of output power |
| FP | Fabry-Perot, perhaps the simplest laser configuration consisting of a cavity with two mirrors |
| FWHM | full width at half-maximum, the measure of the width of a peak taken at half-maximum amplitude |
| GaAs | gallium-arsenide, a semiconductor |
| HPDL | high-power diode laser |

| | |
|---|---|
| ILV | current (I), optical power (L), and voltage (V) characteristics of a component |
| InP | indium-phosphide, a semiconductor |
| LIDAR | light detection and ranging, technology to obtain 3D data of the surroundings |
| LOC | large optical cavity |
| MEMS | microelectromechanical system, a group of technologies that enables microscopic manipulation of small objects |
| MPE | maximum permissible exposure, the highest power allowed due to safety concerns (usually in $\mathrm{J\,cm^{-2}}$ or $\mathrm{W\,cm^{-2}}$) |
| MSR | mode suppression ratio |
| NA | numerical aperture, dimensionless number describing the range of angles where light can enter or exit a system |
| NIL | nanoimprint lithography |
| OPA | optical phased array, technology to redirect beam emission by controlling the phase difference of light in adjacent waveguides |
| PCB | printed circuit board |
| PECVD | plasma enhanced chemical vapour deposition |
| QW | quantum well |
| RWG | ridge waveguide |
| SEM | scanning electron microscope |
| SHG | second harmonic generation |
| SNR | signal-to-noise ratio |
| ToF | time of flight, method to estimate distance based on signal return time delay |
| UV | ultraviolet |
| VCSEL | vertical cavity surface emitting laser |

# SYMBOLS

| | |
|---|---|
| $d$ | beam diameter |
| $d_0$ | beam waist diameter |
| $\Gamma$ | confinement factor |
| $I_{th}$ | threshold current |
| $\kappa$ | coupling coefficient |
| $L$ | radiance |
| $\lambda$ | wavelength |
| $\Lambda$ | grating period |
| $M^2$ | beam quality factor |
| $n$ | refractive index |
| $\omega$ | beam radius |
| $\omega_0$ | beam waist radius |
| $T_0$ | threshold current characteristic temperature |
| $T_1$ | slope efficiency characteristic temperature |
| $\theta$ | beam divergence half-angle |
| $\theta_{FULL}$ | beam divergence full-angle |

# ORIGINAL PUBLICATIONS

PubI A. T. Aho, J. Viheriälä, V.-M. Korpijärvi, M. Koskinen, H. Virtanen, M. Christensen, T. Uusitalo, K. Lahtonen, M. Valden and M. Guina. High-Power 1180-nm GaInNAs DBR Laser Diodes. *IEEE Photonics Technology Letters* 29.23 (2017), 2023–2026. DOI: 10.1109/LPT.2017.2760038.

PubII A. T. Aho, J. Viheriälä, H. Virtanen, T. Uusitalo and M. Guina. High-Power 1.5- μm Broad Area Laser Diodes Wavelength Stabilized by Surface Gratings. *IEEE Photonics Technology Letters* 30.21 (2018), 1870–1973. DOI: 10.1109/LPT.2018.2870304.

PubIII A. T. Aho, J. Viheriälä, M. Koskinen, T. Uusitalo, J. Reuna and M. Guina. High-Power 1.5 μm Tapered Distributed Bragg Reflector Laser Diodes for Eye-Safe LIDAR. *IEEE Photonics Technology Letters* 32.19 (2020). DOI: 10.1109/LPT.2020.3019845.

PubIV V.-M. Korpijärvi, J. Viheriälä, M. Koskinen, A. T. Aho and M. Guina. High-power temperature-stable GaInNAs distributed Bragg reflector laser emitting at 1180 nm. *Optics Letters* 41.4 (2016). DOI: 10.1364/OL.41.000657.

### *Author's contribution*

All the publications included in this thesis are the result of the work done by many people. The thesis author has contributed to them in the following way:

Publication I The thesis author designed and procured the photolithography and nanoimprint lithography masks used in the fabrication, participated in component packaging, designed and controlled the

anti-reflection coatings in an iterative fabrication process, designed the measurement procedures, designed and procured custom hardware to make samples compatible with existing characterization systems, designed and implemented new characterization setups, performed all device characterization except for the high-current tapered DBR ILV measurement, analyzed the characterization results, wrote the first version of the manuscript, and coordinated the publication process.

Publication II — The thesis author designed and procured the photolithography and nanoimprint lithography masks used in the fabrication, designed the anti-reflection coatings, designed and procured suitable hardware to make the anti-reflection coating system compatible with the samples, packaged the components, designed the measurement procedures, designed and procured custom hardware to make samples compatible with existing characterization systems, designed and implemented new characterization setups, performed the device characterization, analyzed the characterization results, wrote the first version of the manuscript, and coordinated the publication process.

Publication III — The thesis author designed and procured the photolithography and nanoimprint lithography masks used in the fabrication, designed the anti-reflection coatings, participated in component packaging, designed the measurement procedures, designed and procured custom hardware to make samples compatible with existing characterization systems, designed and implemented new characterization setups, performed most of the device characterization, analyzed the characterization results, wrote the first version of the manuscript, and coordinated the publication process.

Publication IV — The thesis author participated in the component packaging, contributed to the characterization and analysis, and took part in manuscript preparation. This publication was also included in the doctoral thesis of Dr. Ville-Markus Korpijärvi.

# 1 INTRODUCTION AND SCOPE

Since their original demonstration in 1960 [1], lasers have become a ubiquitous and versatile technology. They are used in industrial welding [2], telecommunication systems [3], medicine [4], spectroscopy [5], consumer electronics [6, 7], and many other fields. The wide spread of laser applications has been enabled by the diversity of distinct laser technologies. The term laser is a general concept where light is amplified in a cavity through the process of stimulated emission, and there are multiple technical implementations how this can be achieved. For applications requiring high power, such as welding, solid-state and gas lasers with tens of kilowatts of output power are available [8]. Consumer DVD and Blu-Ray players utilize cheap and compact mass-producible diode lasers [9, 10]. Molecular dynamics during chemical reactions can be imaged using massive X-ray free-electron lasers that can be several kilometers in length [11].

In many cases, where the affordability of the laser enables the spread of the application, or where the application requires compactness, the optimal solution is a diode laser. Diode lasers are based on semiconductor materials with the ability to generate stimulated photons when an excited electron relaxes from the conduction band to the valence band. Semiconductors often provide high gain, enabling compact cavities, and existing mass-manufacturing methods make it possible to cost effectively produce large volumes of small semiconductor chips. The market volume of high-power diode lasers (HPDLs) is large, and often these lasers are the most appropriate solution when high-power light sources are needed. Conventional HPDLs, found in most HPDL applications, are realized with the most simple cavity layout where the cavity is formed between two parallel facets of a semiconductor chip with an electrically pumped wide stripe running on top of it. Although such broad-area laser diodes (BA-LDs) are excellent in many applications, they suffer from limitations in brightness and spectral intensity: the laser beams they produce cannot be collimated or focused well, and the optical power is spread over a large spectrum of wavelengths.

This thesis addresses how to enhance the properties of HPDLs by increasing their radiance and spectral intensity by integrating appropriate elements monolithically on the semiconductor chips, as well as using novel material systems as the basis: previously proven design solutions, such as tapered waveguides, broad-area waveguides, and gratings, are taken and combined together with new material systems in order to meet specific targets. Such compact, cost-effective laser diodes providing high power, good beam quality and narrow spectrum could be ideal light sources in many applications. Table 1.1 shows the suitability of various diode laser technologies for different application requirements. In this thesis, two particularly attractive application cases, LIDAR and second harmonic generation (SHG), are addressed. Due to application requirements, the work is based around two wavelengths, 1.18 μm and 1.5 μm.

**Table 1.1** Suitability of various laser diode technologies for application requirements. The technologies are explained in more detail in chapter 2.

| | | **Application requirement** | | |
|---|---|---|---|---|
| | | Wavelength locking | Power | Brightness |
| **Technology** | RWG-LD | - | + | ++ |
| | DBR-LD | ++ | + | ++ |
| | DBR-BA | ++ | ++ | - |
| | Tapered RWG | - | ++ | ++ |
| | Tapered DBR | ++ | ++ | ++ |

**LIDAR** is a method, analogous to radar, utilizing electromagnetic radiation for consecutive ranging of distance and using the data to construct a 3D image of the target or the surroundings. LIDAR can be utilized in many applications, such as forestry [12], oceanography [13], meteorology [14], geology [15], and glaciology [16], as well as in engineering applications such as architectural modeling [17] and object detection and recognition for automation [18]. The LIDAR systems can be terrestrial [19], airborne [19], or maritime [20]. Most compact LIDAR systems can even be mounted on handheld electronics [21].

In a most basic implementation, a LIDAR comprises a laser and a detector. The laser emits a short, nanosecond scale laser pulse towards the target. When the pulse hits the target, some of it is scattered towards the detector, and the distance to the target can be calculated from the time difference between the emission of the pulse and the detection of scattered light. This kind of LIDAR and many of its embodiments

are classified under the term time of flight (ToF). In practice, in order to operate over longer distances and construct a 3D image, additional components are required e.g. to increase the collection efficiency of the scattered light and to vary the pointing direction of the laser and the sensor. Other LIDAR variants not based on the ToF principle can, for example, utilize single frequency continuous-wave (CW) lasers and measure the velocity of the target from the Doppler-shifted frequency difference between the emitted and received light.

Different LIDAR applications have varying requirements for the lasers utilized as light sources. The lasers developed in this thesis are primarily aimed to serve in a particular implementation of automotive LIDAR [22, 23], an application that is at the moment a rich sub-field of LIDAR development because of the vast commercial potential. This type of use of LIDAR has been a focus of research due to the advent of self-driving cars and other autonomous vehicles. For vehicle automation, LIDAR is a key option for environmental mapping and obstacle detection alongside other technologies such as cameras and radar.

The other main target application of this thesis, SHG [24, 25], also known as frequency doubling, is a phenomenon discovered soon after the first laser was reported. In SHG, two photons of the same wavelength interact with a nonlinear optical medium, and a new photon with twice the frequency is generated. For SHG, the structure of the optical medium must be without inversion symmetry, and for this reason a special material, such as lithium triborate ($LiB_3O_5$) or periodically poled lithium niobate (PPLN) crystal, is required. Due to its nonlinear nature, the SHG response of the medium scales quadratically with the intensity of the incident optical field.

Perhaps the simplest and most familiar application of SHG is simply converting laser light with wavelength $\lambda$ to light with wavelength $\lambda/2$, i.e. doubling its frequency. This is what happens, for example, in green laser pointers [26]. Other applications include characterizing ultrashort laser pulses by autocorrelating them inside an SHG medium (frequency-resolved optical gating, SHG-FROG [27]), and using the ability of suitable microscopy samples to generate SHG signals to obtain improved imaging resolution as well as other advantages (second-harmonic imaging microscopy [28]).

## 1.1 Requirements for LIDAR applications

As with most engineering solutions, automotive LIDAR implementations have to balance between technological and economical trade-offs. The laser used in a LIDAR system has to have enough output power to generate sufficient backscattering from the target for the detector to pick it up, but the power consumption of the laser must not be excessive and the scanning beam must be safe for other road users. The smaller the LIDAR module is, the easier it is to fit into vehicles without awkward structural or aesthetic drawbacks, but miniaturization also places constraints on the laser technologies used. The wavelength of the laser must be selected so that there is not too much atmospheric absorption, but this also means more background radiation from the sun and reduced signal-to-noise ratio.

One absolute necessity for LIDARs to be used in traffic is that they are eye-safe. This poses a wavelength-dependent restriction on the output power of the LIDAR laser. According to the IEC 60825 safety standard [29], in the wavelength range from visible to near-infrared and a pulse length of 1 ns, the highest allowed maximum permissible exposure (MPE) in $\mathrm{J\,cm^{-2}}$ is approximately in the band from 1500 nm to 1800 nm. However, many current LIDAR systems operate in the range 800 nm to 1000 nm [30, 31], where the equivalent MPE is rougly six orders of magnitude lower. One explanation for this is the availability of inexpensive and high performance diode lasers and detectors in this wavelength range, and in some cases even the more restricted output power is sufficient. Usually, submicron wavelength range HPDLs are used in line scanning LIDAR implementations. BA-LDs (such as the one in [PubII]) have a good beam quality in the fast axis direction and poor beam quality in the slow axis direction, and thus a sharp scanning line can be formed from their output beam.

Scenarios where the relaxed output power constraints of e.g. 1500 nm LIDAR systems would be handy include weather conditions with reduced visibility: rain, fog, and snow: these longer wavelengths have been reported to penetrate fog and rain better [32]. Moreover, the simple fact that more photons can be launched towards the target before reaching the eye-safety limit also helps to receive a higher signal level when a large part of the emitted light is lost during the propagation. LIDAR performance in adverse weather is critical for the development of autonomous vehicles, since they need to be able to perform reliably also in these challenging but

common conditions. These limitations in existing LIDAR implementations and the demand for all-weather automotive LIDAR systems have driven the HPDL development in this thesis.

**Fig. 1.1** Artist's depiction of a LIDAR working in challening weather conditions. [33]

Wavelengths around 1500 nm are also suitable for LIDAR use in terms of atmospheric transmission, since there is very little absorption in the wavelength range from 1500 nm to 1800 nm [34]. This, however, means that there is also a high background noise level originating from solar radiation, shown in Fig. 1.2, which is a problem on a sunny day since it may overwhelm the actual signal. To reduce this effect, a bandpass filter may be applied to the receiver of the LIDAR system. This way only the wavelengths that are emitted by the laser reach the detector, and most of the background noise is eliminated. The wavelength filtering must be done in a way that ensures that the emission wavelength of the laser, which can be affected by e.g. the operating temperature and random wafer quality variation during the laser fabrication process, is always within the passband of the filter. **Thus, a laser with a narrow, stable and predictable emission wavelength provides the best basis for background noise filtering. This kind of laser is demonstrated in [PubII, PubIII].**

Unlike in currently used solutions with emission in the 900 nm range, at 1.5 μm point scanning is the preferred LIDAR scanning approach instead of line scanning. Cheap Si-based detectors allow cost-efficient detector arrays necessary for line scanning at near-infrared [30], but for InGaAs technology, required above approximately 1.2 μm, such detector arrays are expensive. Thus, a low-cost 1.5 μm LIDAR system is limited to a single-pixel detector and point scanning. [36] Point scanning, also called 2D scanning, can be implemented with various technologies. The most common ways to direct the laser beam are mechanical (e.g. rotating or oscillating mirrors or

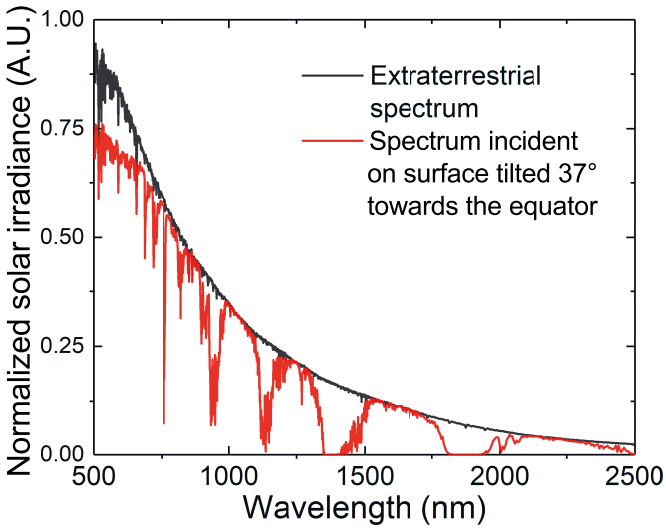


**Fig. 1.2** Extraterrestrial solar spectrum and spectrum incident on a ground-level surface tilted 37° towards the equator and facing the sun under standard atmosphere. Adapted from [35].

prisms), microelectromechanical (MEMS, millimeter-scale mirrors rotated by electrostatic, magnetic, thermal or piezoelectric actuators), and optical phased arrays (OPA, controlling the phase of light in adjacent waveguides to produce constructive interference in the desired direction) [31].

Especially in 2D point scanning, the beam quality of the laser is important from the perspective of the spatial resolution of the LIDAR [37]. **The better the beam quality is, the better the beam can be collimated and thus a smaller spot size can be achieved at the target. Demonstration of such a laser for eye-safe LIDAR motivated [PubIII].** Other factors affecting the spatial resolution include the frame rate of the LIDAR system and the pulse repetition rate of the laser. If a high spatial resolution (i.e. more data points) is wanted, generating a single scan frame takes a longer time, which lowers the frame rate. A higher pulse repetition rate on the other hand enables faster scanning.

Another way to utilize high-power and narrow spectral width diode lasers for LIDAR is to use them as seed lasers for erbium-doped fiber amplifiers (EDFAs) [38] operating around 1550 nm. Fiber amplifiers enable much higher peak output power than any diode laser, over 100 kW [39]. The availability of high optical power at

an eye-safer wavelength, compared to sub-micron wavelengths, enables weather LIDAR implementations utilizing e.g. flash LIDAR, gated imager and line scanning methods. Since the cost of the fiber amplifier system is anyway rather high and beyond the realm of mass producible consumer products, the added cost of an InGaAs detector array required for these LIDAR approaches is tolerable. However, there is a strong drive to push down cost and footprint of fiber laser and detector to enable its use in automotive LIDAR in the future.

Operating the EDFA in the gain saturation regime using a high seed power improves the performance by reducing the noise caused by spontaneous emission [40], and fewer amplifier steps would be required in an amplifier cascade system [41] enabling less bulky and cheaper lasers. The amplifiers maintain the emission wavelength of the seed laser and may even reduce the spectral width through gain narrowing [42], retaining the ability to use narrow bandpass filters at the LIDAR receiver.

Typically seed lasers in ns-pulsed fiber lasers are based on simple laterally single-mode waveguides and allow output powers below 100 mW. Around 1060 nm wavelength, however, tapered DBR lasers have enabled the coupling of 3.5 W optical power (with 65 % coupling efficiency) into single mode fibers [43], indicating that ns-pulsed 1.55 μm tapered lasers could be ideal for seeding the EDFA in LIDAR applications. **This has motivated [PubIII] and subsequent work. For single mode fiber coupling, a tapered laser design with a high beam quality is required for efficient coupling of light into the optical fiber.**

### LIDAR wavelength considerations

Laser emission wavelength has three parameters that affect LIDAR operation: center wavelength, spectral width, and wavelength stability.

The center wavelength has both qualitative and quantitative effects on the LIDAR system. At wavelengths shorter than approximately 1.1 μm silicon based detectors can be used. Si detection technology is well established and cheap thanks to its proliferation in consumer goods like digital cameras. Cheap Si detector arrays enable the use of LIDAR implementations that detect light from multiple points simultaneously, like line scanning and flash LIDAR. The selected center wavelength also determines the material system used in the laser diode: AlGaAs/GaAs and InGaAs/GaAs based lasers can be used with Si detectors while InGaAsP/InP lasers

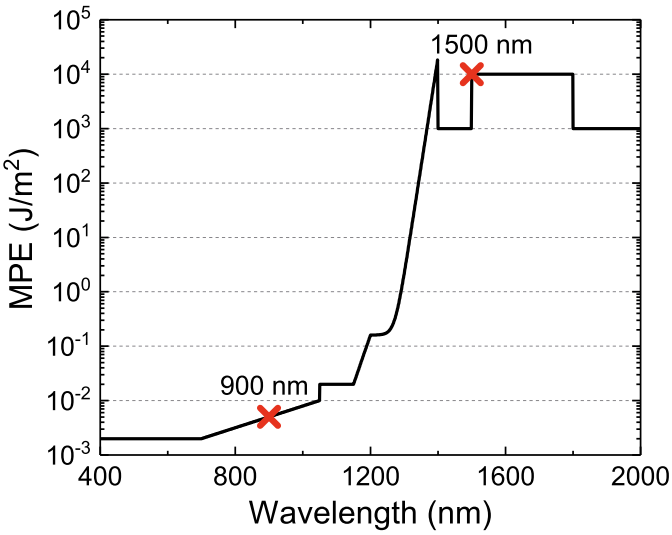


**Fig. 1.3** Maximum permissible exposure at the human cornea for various wavelengths for 50 ns long pulses. [29] Note over six orders of magnitude difference between 1.5 µm and 900 nm ranges.

emit longer wavelengths that require more expensive InGaAs based detectors.

An important aspect of the center wavelength from the point of view of LIDAR, and one of the main themes of this thesis, is that the eye-safety power limits are highly wavelength dependent. The corneal MPE ratings for 50 ns pulses is shown in Fig. 1.3. The shape of the curve results largely from the optical transmittance of the human eye, since the retina is highly vulnerable to damage from optical radiation. The wavelength range above 1400 nm is often labeled as eye-safe due to the strong absorption of light by the cornea and the lens at these wavelengths [44].

The main impact of the spectral width of the laser used in a LIDAR system results from the filters that can be used in combination with the detectors. The detectors themselves, both Si and InGaAs in their respective wavelength ranges, have broad wavelength responsitivities, and purely from the point of view of LIDAR operation also broad wavelength bands could be used. However, a broad detection band also collects more background radiation which reduces the signal-to-noise ratio (SNR). Since the LIDAR is wanted to be operated in a wavelength range where atmospheric absorption is low, the background radiation level will be high. If the emitted power can be squeezed into a narrow wavelength range, the background radiation outside

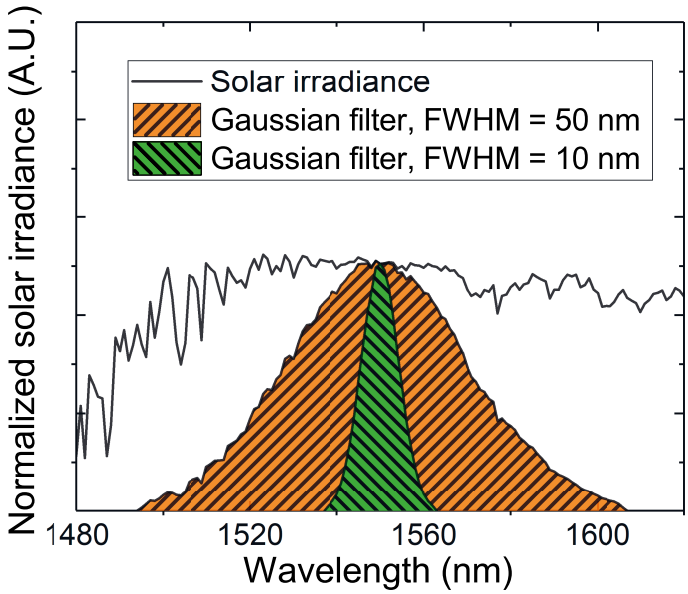


**Fig. 1.4** Transmitted solar background radiation around 1550 nm when 50 nm FWHM or 10 nm FWHM Gaussian bandpass filter is used. The narrower filter reduces the transmitted radiation by 79 %. The solar irradiance is based on AM1.5 spectrum [35].

this range (and some suitable margin) can be filtered out by using a combination of short pass and long pass filters. Fig. 1.4 shows the transmitted background radiation when either a 50 nm full-width at half-maximum (FWHM) or a 10 nm FWHM Gaussian bandpass filter is used around the center wavelength 1550 nm. In the latter case the transmitted background radiation is reduced by 79 %.

In order to utilize as narrow passband filters as possible to improve the SNR, having a narrow emission spectrum is not alone sufficient. The peak gain wavelength of the QW shifts as a function of temperature (e.g. for the used 1.5 μm material the rate of shift is approximately 0.5 nm/°C [PubII]), and since the ambient temperature conditions in a consumer automotive environment can vary from −40 °C to 80 °C, without any stabilizing mechanism the detector passband would have to be unnecessarily wide.

## 1.2 Requirements for second harmonic generation

Although diode lasers have many advantages, such as mass-producibility, compactness, high output power and ease of operation through electrical pumping, one distinct disadvantage is that there are some wavelength ranges where feasible semiconductor gain materials have not been discovered. Earlier, for example, blue was such a wavelength range, and the invention of a high-efficiency gain material for the blue wavelength range [45, 46] was considered such a breakthrough that the inventors were eventually awarded with the Nobel Prize in physics [47]. In the yellow–orange wavelength range, direct lasing using a semiconductor gain material has only been achieved under temperatures [48] or pressure conditions [49] which are challenging to maintain in application use, or by optical pumping [50]. Lasers in this wavelength range have many applications e.g. in the medical field [51–53].

An alternative way to use diodes to produce laser light in the challenging wavelengths is to use a frequency doubling scheme. If the target wavelength is $\lambda_t$, a laser diode with emission wavelength $2\lambda_t$ is used and a part of the emitted light is converted to the correct wavelength using second harmonic generation (SHG). This method has been used to produce, for example, high yellow output power using a vertical-external-cavity surface-emitting laser with a semiconductor gain chip [54].

For the second harmonic generation process to be efficient, the incident beam has to satisfy two parameters:

1. The beam must have high brightness [55, 56].
2. Most of the output power must be confined to a narrow wavelength range [57].

Requirement 1 results from the feature that the SHG conversion efficiency increases with the incident optical power. Thus, the efficiency can be increased by focusing the beam tightly inside the nonlinear medium. However, due to the behaviour of Gaussian beams [58], focusing the beam tightly in the middle of the medium causes a large divergence outside of the beam waist, and thus the overall efficiency decreases. In order to obtain the maximum overall conversion efficiency, the beam waist and divergence must be optimized according to the properties of the medium used. For Gaussian beams, the optimum beam waist radius $\omega_0$ can be

calculated as

$$\omega_0 = \sqrt{\frac{\lambda_0 L}{2\xi\pi n_0}}, \tag{1.1}$$

where $\lambda_0$ is the fundamental wavelength, $L$ is the length of the crystal, $\xi$ is the focusing parameter ($\xi = 2.84$ for quasi phase matched crystals), and $n_0$ is the crystal refractive index at the fundamental wavelength [56]. Brightness (sometimes referred to as radiance) $L$ is a useful quantity for determining the quality of the laser source for high power density focusing and collimation, defined as [55]

$$L = \frac{P}{\pi\omega_0^2 \pi\theta^2}, \tag{1.2}$$

where $P$ is the optical power over, and $\theta$ is the divergence angle, incorporates all these features required for obtaining a high SHG conversion efficiency. It is also tightly related to the laser beam quality factor $M^2$ defined as

$$\theta = M^2 \frac{\lambda}{\pi\omega_0}, \tag{1.3}$$

where $\lambda$ is the wavelength. Using $M^2$, radiance can be written as

$$L = \frac{P}{M^4 \lambda^2}. \tag{1.4}$$

Requirement 2 arises from the challenge that, due to normal dispersion in the nonlinear medium (i.e. the refractive index decreases with increasing wavelength), the incident light and the frequency-doubled light start to go out of phase when propagating along the optical axis in the medium [59]. This phase mismatch reduces the efficiency of the SHG conversion. One solution to this is quasi-phase-matching (QPM) the medium [60] by fabricating it so that one of the crystalline axes is inverted periodically along the optical axis. However, QPM only works for a particular, narrow acceptance wavelength band [57], which can be tuned by changing the temperature of the nonlinear crystal [61].

**The conclusion that can be made based on requirements 1 and 2 is that a laser suitable for SHG should have high output power, good beam quality, and narrow and stable emission wavelength.**

At the time the work for this thesis was started, around 2015–2016, high-power

sources with good beam quality were not available in the wavelength range from 1154 nm to 1240 nm. With frequency doubling these wavelengths can be used to obtain wavelengths from yellow to orange which have e.g. medical applications [62]. Wavelengths approaching 1200 nm could be obtained with GaInAs/GaAs laser diodes which are highly efficient at shorter wavelengths, but extending the wavelength by increasing the In content causes high strain in the quantum well and required the use of strain compensation layers to make the component operational. An alternative way to reach this challenging wavelength range was to add a small amount of nitrogen to the structure. Compared to GaInAs/GaAs structure, GaInNAs/GaAs has reduced strain and improved carrier confinement, leading to better performance. Due to the requirements of SHG, the dilute nitride material was first tested with a distributed Bragg reflector laser diode (DBR-LD) [PubIV] and later with tapered DBR-LD [PubI].

### SHG wavelength considerations

SHG has tighter spectral width requirements than ToF LIDAR. The wavelength acceptance bandwidth depends on the nonlinear material, the fundamental wavelength, and the length of the crystal. For example, for periodically poled lithium niobate, at 1 μm fundamental wavelength and 1 cm crystal length, the wavelength acceptance bandwidth is approximately 0.02 nm [63], although various techniques have been presented to increase the bandwidth [64]. Knowing the material properties of the nonlinear medium, the FWHM acceptance bandwidth $\Delta\lambda$ can be calculated as

$$\Delta\lambda = \frac{0.443\lambda_0}{L}\left|\frac{n_{SH}-n_0}{\lambda_0}+\frac{\partial n_0}{\partial \lambda_0}+\frac{\partial n_{SH}}{\partial \lambda_{SH}}\right|^{-1}, \tag{1.5}$$

where $\lambda_0$ and $\lambda_{SH}$ are respectively the fundamental and the frequency doubled wavelengths, $L$ is the length of the crystal, and $n_0$ and $n_{SH}$ are respectively the refractive index at the fundamental and frequency doubled wavelengths [57].

The desired center wavelength of the fundamental SHG light is determined by the application, and the SHG crystal poling period is matched accordingly with fine tuning performed by controlling the temperature of the crystal. The wavelength stability requirement follows from the wavelength acceptance band of the used SHG technique. If the wavelength shifts by half of the FWHM acceptance bandwidth

from the peak efficiency wavelength, the SHG efficiency drops to half.

### Considerations related to the choice of SHG crystals

Nonlinear crystals can be divided into three categories depending on their ability to confine incident light: 2D, 1D, and 0D. Waveguide crystals confine light both in horizontal and vertical directions (2D), and are best suited for small power operation, since the light can be kept tightly confined along a long distance for increased conversion efficiency. At high powers, the tight confinement of light at the input facet easily damages the crystal facet. For example, the non-tapered laser in publication IV would be a rather ideal source for a waveguide crystal but e.g. the multi-watt level tapered laser in [PubI] could damage such a crystal. 1D crystals offer a planar waveguide. This enables confinement in one direction along the length of the crystal while enabling higher input powers compared to 2D confining crystals. Finally, 0D crystals offer no confinement at all. This makes coupling of light the easiest compared to 1D and 0D crystals since there is no small waveguide that needs to be targeted with the input beam, but the beam diverges inside the crystal so a tight focus along a long distance cannot be achieved. 1D and 0D crystals need multi-watt power levels from the laser diode, such as the one in [PubI], because otherwise the optical field intensity inside the crystal is too low for efficient non-linear conversion. Table 1.2 lists state-of-the-art results obtained with different crystal types.

**Table 1.2** State-of-the-art results with different nonlinear crystal types.

| Crystal | SHG power (W) | Pump power (W) | Pump wavelength (nm) | Ref. and notes |
|---|---|---|---|---|
| 0D | 1.5 | 9.3 | 1062 | [65] |
| 0D | 3.7 | 9.5 | 1063 | [66], two cascaded crystals |
| 1D | 1.07 | 4.1 | 1064 | [67] |
| 2D | 0.86 | 2.03 | 1178 | [68] |

## 1.3 Overview of the publications and the state of the art

Table 1.3 describes the application targets that have been studied and their relation to publications I–IV. Publications I–III present results from high brightness and/or high power wavelength locked lasers, while publication IV, although first in tempo-

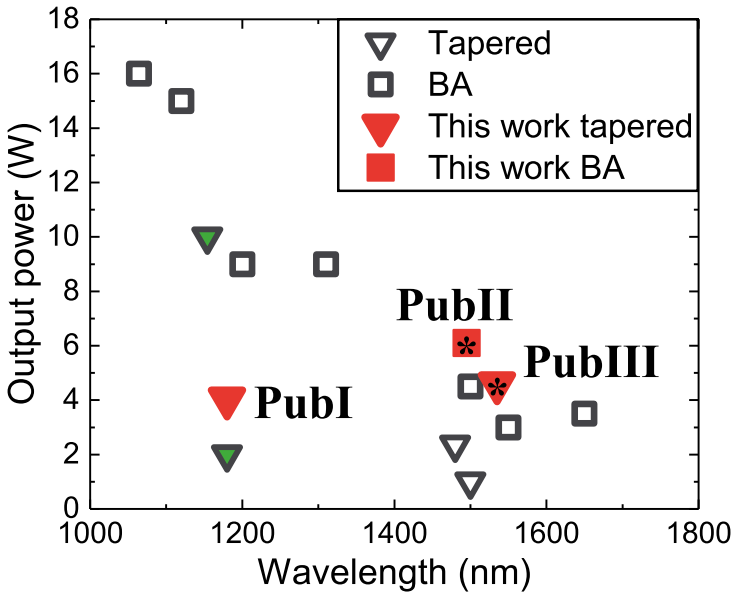


**Fig. 1.5** State-of-the-art published and commercial results from tapered [69–72] and broad-area laser diodes [73–77] and the results discussed in this thesis as a comparison [PubI, PubII, PubIII]. Marker with green fill indicates wavelength locked (external) result. Marker with asterisk (*) indicates pulsed operation.

ral sense, is listed last with the first results from wavelength locking. In addition to the included publications, chapter 4 shows recent results that are still unpublished but demonstrate further optimized brightness compared to published results.

**Table 1.3** Research targets and their link to wavelengths and applications addressed in each publication.

| | | **Wavelength and application** | |
|---|---|---|---|
| | | 1.18 μm for yellow-orange lasers | 1.5 μm for eye-safe LIDAR |
| Target | High power | Pub I | Pub II, Pub III |
| | High brightness | Pub I, Pub IV, In Progress | Pub III, In Progress |
| | Wavelength locking | Pub I, Pub IV | Pub II, Pub III |

Finally, Fig. 1.5 shows a comparison between state-of-the-art results and the results reported in the publications included in this thesis for both tapered and broad area lasers aimed at both LIDAR and SHG.

# 2 RELEVANT BACKGROUND ON LASER TECHNOLOGY

## 2.1 General laser operating principle

Laser, originally an acronym of light amplification by stimulated emission of radiation, is a device that circulates photons in a cavity containing a gain medium that produces more photons through stimulated emission. A simple laser comprises two mirrors to form the cavity with the gain medium in between, shown in on the left side in Fig. 2.1. In order for the stimulated emission to take place and the laser to function, the gain medium must be excited and a population inversion must be achieved. This means that there has to be more particles in the excited state than in the ground state, so that stimulated emission becomes more probable than the absorption of the photons. When the population inversion is achieved and a photon interacts with an excited particle of the medium, the excitation is relaxed and a new photon with an identical wavelength, phase, and direction is generated. When the reflectance of one of the cavity mirrors is reduced below 100 %, some photons escape the cavity on each round-trip, forming the output beam of the laser.

In edge-emitting semiconductor lasers, which are the focus of this thesis, the semiconductor acts both as the cavity and the gain medium of the laser. The opposite facets of the semiconductor chip, cleaved along crystal lattice planes, act as the mirrors. The as-cleaved facets of common semiconductors used in lasers, such as GaAs and InP, have a reflectance of about 30 % in air. The gain is provided by electrons $e^-$ in the conduction band of the semiconductors relaxing into the valence band. The valence band is populated by holes $h^+$, i.e. pseudo-particles resulting from missing electrons, and in stimulated emission the excited electrons recombine with the holes as shown on the right panel in Fig. 2.1. Excitation of the gain medium is usually achieved through electrical pumping by injecting an electric current through the

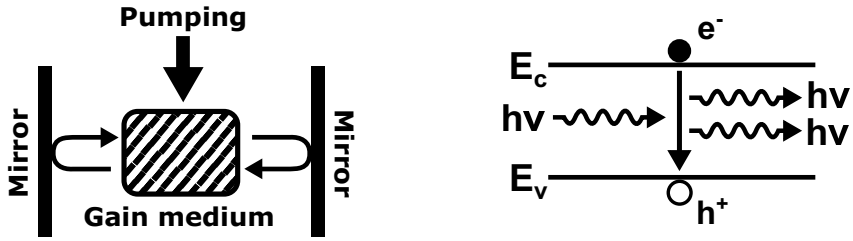


**Fig. 2.1** Left: Schematic model of a laser. Light circulates between the mirrors and is amplified through stimulated emission by the gain medium. The amplification is made possible by the excitation of the medium through pumping. Right: Stimulated emission in semiconductor. Excited electron $e^-$ recombines with the hole $h^+$ when an incident photon with energy $h\nu$ interacts with the system. As a result a new photon with identical energy, phase, and direction is generated.

semiconductor layer structure.

The semiconductor structure of a laser consists of multiple thin semiconductor layers on top of a thicker semiconductor substrate. The lasers discussed in this thesis are mostly based on a double-heterostructure type called a quantum well (QW), shown in Fig. 2.2. The QW is a thin layer with a thickness in the range of the de Broglie wavelength of the injected electrons and holes, so that the electron and hole energy states in the conduction and valence bands, respectively, become discrete. The energy difference between the lowest conduction band state and the highest valence band state is called the band gap, and it is equal to the energy of the photons that are generated when an electron and a hole recombine in a particular structure. The layer structure is designed so that the conduction band minimum and the valence band maximum are situated in the QW layer, meaning that the injected electrons in the conduction band and the holes in the valence band see the QW as a potential well and become trapped, improving the recombination efficiency. Surrounding the QW are cladding layers providing carrier confinement, waveguide layers (also called optical confinement layer, OCL) providing optical guiding perpendicular to the semiconductor growth direction, meaning that the refractive indices of the layers are selected so that the photons generated in the quantum well are guided parallel to the quantum well plane, and contact layers to improve current conduction and reduce the resistance between the contact metal and the semiconductor. The semiconductor layers on the substrate are grown epitaxially, i.e. so that the atoms forming the grown layers adopt the crystal lattice structure of the substrate.

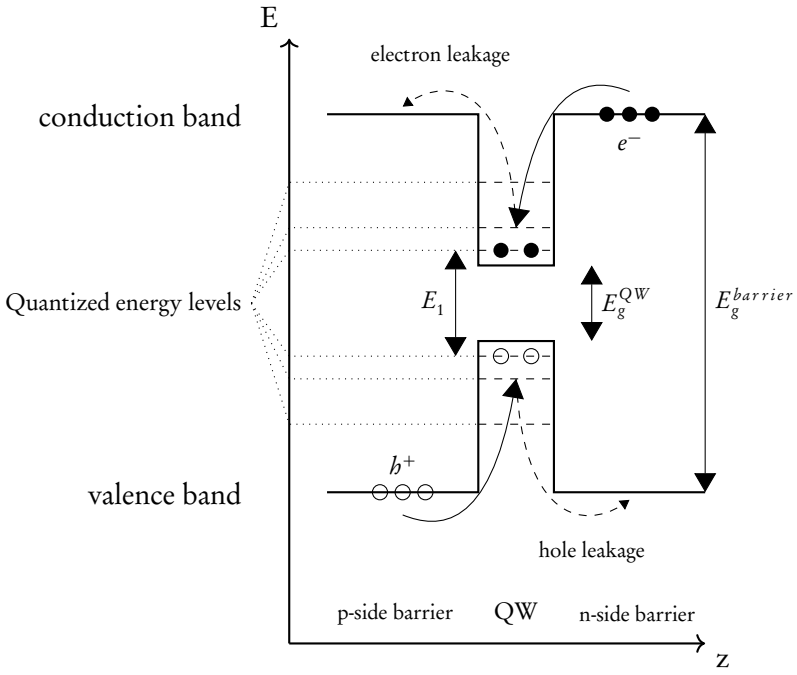


**Fig. 2.2** Band structure in the quantum well and barrier layers. z is the direction perpendicular to the plane of the wafer. $E_g$ are the band gaps for the QW and the barrier layers. $E_1$ is the recombination energy when an electron relaxes. [78]

## 2.2 Cavity modes

The optical field inside the laser cavity can only have certain spatial resonances due to the wave nature of light. These resonances are called modes. The modes of the laser are divided into longitudinal and transverse components. The longitudinal modes are defined by the axis of the cavity and result from the condition for constructive and destructive interference.

The emission spectrum of a laser is determined by two factors: the gain available for modes of the active region and the supported (passive) cavity modes. The gain bandwidth describes the range of wavelengths that can be amplified by the gain medium. For semiconductor lasers the gain bandwidth is usually continuous, bell-shaped, and several tens of nanometers wide, depending on the active region.

A cavity confined between two reflecting mirrors is called a Fabry-Perot (FP) cavity. In this kind of cavity the supported cavity modes result from the constructive

and destructive interference of different wavelengths inside the cavity. Wavelengths $\lambda$ for which the optical round-trip length of the cavity $2nL$ is an integer multiple, interfere constructively:

$$m\lambda = 2nL, \tag{2.1}$$

where $m$ is an integer, $L$ is the length of the cavity and $n$ is the effective refractive index of the cavity. Conversely, if the optical round-trip length of the cavity equals $(m+1/2)\lambda$, the interference is destructive and these wavelengths are attenuated. The distance $\Delta\lambda$ between the constructive interference peaks follows the FP etalon free spectral range:

$$\Delta\lambda(\lambda) = \frac{\lambda^2}{2n(\lambda)L}. \tag{2.2}$$

The combined effect of the gain bandwidth and the supported cavity modes is a comb-like emission spectrum shown on the left side in Fig. 2.3. The start, the end and the envelope of the comb in wavelength space are determined by the gain bandwidth and the spacing of the peaks by the cavity. Gain clamping occurs when the primary mode starts to lase [79]. Often the cavity is so long that the neighbouring peaks start to overlap in spectral measurements and only the envelope of the peaks is seen, unless an extremely high resolution is used.

In a FP laser cavity, all resonant cavity modes are almost equally supported by the cavity since the reflectance of each mode at both mirrors is approximately equal, varied only by the dispersion of the effective refractive index of the mode at the facet of the cavity, whose effect is usually negligible. In high power diode lasers the cavities are usually so long that many resonant modes fit inside the gain bandwidth, and the result is a wide emission spectrum.

Lasers exhibit frequency noise $\Delta\nu$ that broaden the output spectrum. In diode lasers the fundamental limit for spectral linewidth is given by spontaneous emission and carrier density fluctuations [80]. This limit can be calculated using the famous Schawlow-Townes equation [81]

$$\Delta\nu = \frac{4\pi h\nu(\Delta\nu_c)^2}{P_{out}}, \tag{2.3}$$

where $h\nu$ is the photon energy, $\Delta\nu_c$ is the resonator bandwidth, and $P_{out}$ is the output power. In practice, the linewidths of physical lasers are usually much higher.

Transverse modes, as depicted on the right side in Fig. 2.3, result from the optical

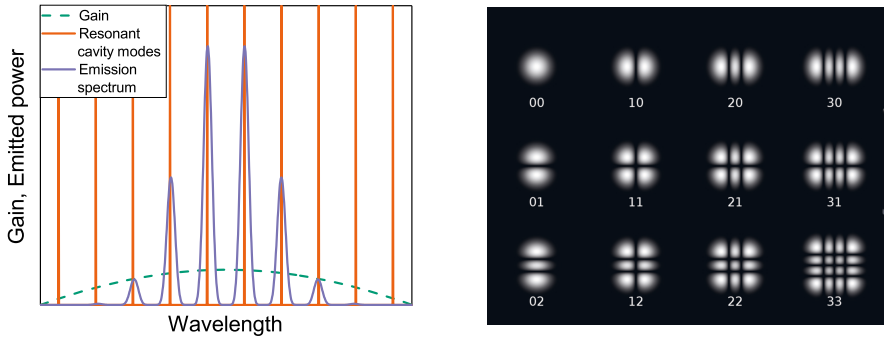


**Fig. 2.3** Left: Emission spectrum determined by the gain bandwidth of the gain medium and the resonant cavity modes. Right: Spatial energy distribution of transverse Hermite-Gaussian modes [82].

confinement provided by the semiconductor layer structure in the vertical direction and the ridge waveguide in the horizontal direction. The primary, Gaussian mode, labeled $TEM_{00}$ and shown in the top left corner on the right side in Fig. 2.3, is usually the only desired mode since it can be collimated and focused in an optimal way. The way to limit the lasing to only the fundamental mode is usually to induce enough losses to the other modes to suppress the gain they experience.

## 2.3 Wavelength locking with Distributed Bragg reflector

Many applications require a more narrow spectrum than provided by FP-LD. There are multiple ways to select a mode or a group of modes in diode lasers. Generally, if only one mode is predominantly lasing, the laser is called single mode. If the mode-selection mechanism allows only a few modes to lase in a fixed wavelength region, the laser is called wavelength locked because the mode selection locks the emission wavelength of the laser in a range preventing it from shifting freely along the gain spectrum.

The gain bandwidth arises from the material properties of the used semiconductor material. In order to affect the resonant cavity modes, the cavity mode spacing should be altered by design so that only one mode fits inside the gain bandwidth, or at least that the modes adjacent to the centermost mode are so far away that they

have so little gain that their intensity is negligible compared to the primary mode, or by suppressing unwanted modes inside the gain bandwidth. Since eq. (2.2) shows that the only way to increase the spacing of the modes is to reduce the length of the cavity or the refractive index, we opted to work with mode suppression because our applications require high powers, and short cavities with a small mode volume make obtaining high power difficult.

Elements locking the wavelength can be monolithically integrated on same chip that provides the gain. Such elements tend to be periodic structures manipulating feedback, gain or loss that different modes experience. Cavity elements can be inserted also outside of the gain chip forming a so called external cavity laser. A common approach is to have a narrow band reflector positioned on front of the gain chip to provide mode selection while the back facet of the gain chip provides another end of the cavity with wavelength insensitive reflection. Such lasers use, for example, gratings embedded in the out-coupling fiber or in a volume crystal. Both approaches allow fixed wavelength narrow band reflection. Wavelength tunable external cavity lasers are achieved typically by using an external grating with the ability to select the reflection wavelength by adjusting the angle of the grating with respect to incident beam.

Distributed reflectance achieved with a monolithically integrated grating is the basis of two important edge emitting diode laser types: the distributed feedback laser diode (DFB-LD) [83] in which the distributed feedback (DFB) covers the whole cavity, and the distributed Bragg reflector laser diode (DBR-LD) [84] in which one or both of the cavity mirrors are replaced with a distributed Bragg reflector (DBR). The primary difference between these two device types is that in a DFB-LD the grating region also provides gain for the laser while in a DBR-LD the grating is passive.

DBR laser affects the intensity distribution of the resonant modes by making the mirror reflectance wavelength dependent. This way, if the wavelength range in the middle of the gain band can be made highly reflective and provide strong feedback while the facets are nearly transparent at the edges of the gain band, only the cavity modes in the center of the band can support lasing. A common way to accomplish this kind of wavelength dependence is to use distributed feedback, where, instead of a single highly reflective interface, the mirror consists of multiple periodical interfaces with low reflectances. In a grating with two periodically stacked materials with differing refractive indices $n_1$ and $n_2$, the wavelength $\lambda$ exhibiting in-phase reflectance

is

$$\lambda = \frac{2\overline{n}\Lambda}{l}, \tag{2.4}$$

where $\overline{n}$ is the average refractive index of the grating, $\Lambda$ is the period of the grating and $l$ is the order of the grating [85]. $\lambda$ is called the Bragg wavelength and eq. (2.4) the Bragg condition.

The strength of the interaction of the grating and the mode can be characterized by a coupling constant (also called coupling coefficient) $\kappa$: [86]

$$\kappa L_g = \frac{L_g}{\Lambda}\left(\frac{\Delta\overline{n}}{\overline{n}}\right), \tag{2.5}$$

where $L_g$ is the length of the grating, $\Lambda$ is the grating period, $\Delta\overline{n} = |\overline{n_2} - \overline{n_1}|$ is the refractive index difference and $\overline{n} = (\overline{n_2} + \overline{n_1})/2$ is the average refractive index.

With a low total grating reflectance, the width of the reflectance band can be calculated as [87]

$$\Delta\lambda = \frac{\lambda^2}{2\overline{n}_g L_g}\frac{3.76}{\pi}, \tag{2.6}$$

where $\Delta\lambda$ is the reflectance band FWHM and $\overline{n}_g$ is the group refractive index of the material.

## 2.4 Surface grating DBR lasers

All DBR lasers in this thesis are fabricated using a regrowth free surface grating technology that requires deeply etched gratings penetrating the top cladding layer in order to interact with the optical field deep inside the semiconductor stack. A simple surface grating DBR-LD structure, shown in Fig. 2.4, comprises a passive DBR grating to provide the emission wavelength selection and an active ridge waveguide (RWG) region to provide the gain. The RWG structure also filters out transverse modes and enables laterally single mode lasing. Moreover, RWG enables the confinement of the injection current to the region where the optical gain is needed. Laser diode chips are usually much wider than the actual laser beam due to practical reasons, and without current limiting most of the injection current would be wasted as heat or would result in photons being generated outside of the optical cavity.

Compared to buried grating structures, it is fairly challenging to fabricate first or-

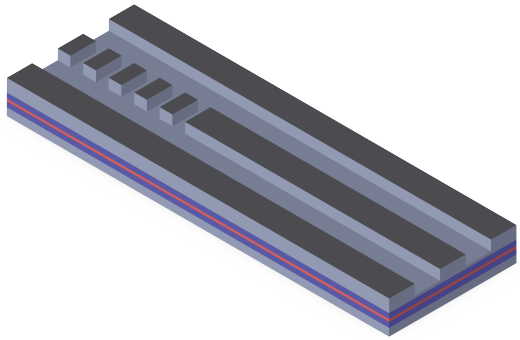

**Fig. 2.4** Schematic of a basic DBR-LD. Injection current flows through the narrow ridge in the middle creating a high current density. The active region, shown in red, is situated below the ridge. The DBR grating is etched to the back of the component. The refractive index difference between the ridge and the surrounding trench limits the transversal modes that the cavity supports.

der surface gratings since they require approximately 100 nm wide structures etched deeply into the semiconductor with an aspect ratio between 10 and 20. For this reason we chose to utilize 3rd order gratings that allow more manageable aspect ratios. Higher order gratings introduce a loss term associated with the energy transfer between the propagating mode and the radiating modes that are orthogonal to the direction of propagation [88]. However, it possible to choose the grating geometry in a way that allows high reflection and low losses [89]. Rather un-intuitively even very high order gratings allow sufficient reflections for operation as long as the etched lines are suitably narrow. For example, reference [90] has demonstrated the use of 80th order gratings in DFB lasers.

In this thesis, DBR technology was selected over DFB due to the used grating fabrication methods. With buried gratings, fabricated with epitaxial regrowth, high power DFBs have been routinely demonstrated, but with surface gratings the effect the grating has on carrier injection makes obtaining high power difficult. With DBR the grating is passive so no carrier injection is required.

The geometry and order of the grating affect the coupling coefficient $\kappa$ and, through it, the width of the reflectance band. [91] By etching the grating lines deeper, a larger fraction of the optical field inside the laser cavity overlaps the refractive index step between the semiconductor and the filling material, and the feedback provided by an individual grating element pair is increased. To optimize the grating reflectivity profile, a balance must be found between $\kappa$ and $L_g$; a large $\kappa$ enables shorter

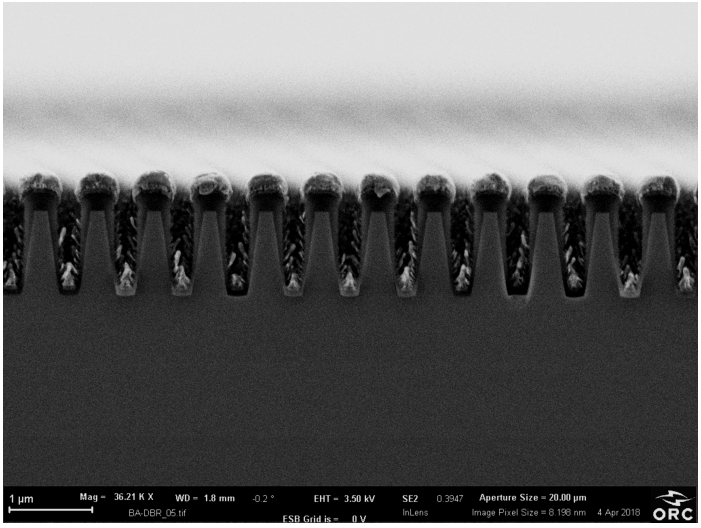


**Fig. 2.5** Cross-sectional scanning electron microscope (SEM) image of a 1.5 µm BA-DBR grating. [PubII]

gratings but wider reflectance band and a longer grating enables narrower reflectance band but is impractical in device fabrication and operation. Also the grating profile, especially the angle between the grating walls and the surface and the rounding of the edges at the bottom of the grating line, affect the $\kappa$. [92] An example of a V-shaped grating used in [PubII] is shown in Fig. 2.5.

Since the point of a DBR cavity mirror is to provide wavelength-dependent feedback, it is necessary to reduce the non-wavelength-dependent reflection originating from the facet on the side of the DBR grating. This is performed by applying a suitable antireflection (AR) coating on the facet. The coating consists of one or more dielectric layers with suitable refractive indices to attenuate the reflectance in a certain wavelength band through destructive interference, much like the DBR grating is designed to provide increased reflectance through constructive interference. The width of the efficient antireflectance band is related to the number of dielectric layer pairs, but in many cases a single pair provides a wide enough AR band to cover enough of the gain bandwidth to suppress modes not supported by the DBR grating.

The mode selected by a DBR-LD depends on the mode suppression ratio (MSR), determined from the gain and mirror loss difference between the lasing mode and the next strongest mode, assuming all other conditions for the modes are equal. The

MSR can be estimated by [93]

$$MSR \approx \frac{\Delta\alpha + \Delta g}{\delta_G} + 1, \tag{2.7}$$

where $\Delta\alpha = \alpha_m(\lambda_1) - \alpha_m(\lambda_0)$ is the difference between the mirror losses at the two wavelengths, $\Delta g = \Gamma g(\lambda_0) - \Gamma g(\lambda_1)$ is the difference between the modal gain at the two wavelengths, and $\delta_G = \alpha_m(\lambda_0) - [\Gamma g(\lambda_0) - \alpha_i]$ is the difference between the mirror loss and the net modal gain for the primary mode. The gain difference results from the shape of the gain bandwidth provided by the active region and the mirror loss difference results from the reflectivity of the grating and the longitudinal mode spacing of the cavity. The mirror loss is related to the threshold gain and the internal losses of the laser by [94]

$$\Gamma g_{th} = \langle \alpha_i \rangle + \frac{1}{L_{DBR}} \ln\left[\frac{1}{r_1 |r_g'|}\right], \tag{2.8}$$

where $\Gamma$ is the confinement factor, $g_{th}$ is the threshold gain, $\langle \alpha_i \rangle$ is the internal losses of the laser, $L_{DBR}$ is the length of the laser cavity using the effective length of the grating, and $r_1$ and $r_g'$ are the reflectivities of the cleaved facet and the grating, respectively. A simulated mirror loss is sketched in Fig. 2.6 for a 5 mm long cavity with a 2 mm long DBR grating, showing best feedback for a mode at 1164 nm. The front facet reflectivity, if flat, has no effect on the mirror loss difference of the adjacent cavity modes. The front facet can thus be used, for example, to increase the tolerance to external feedback and to narrow the linewidth of a DBR laser when it is increased [95] or to improve the output power when decreased, as in this thesis. However, in the case of tapered RWG lasers, increasing the front facet reflection reduces the beam quality [96].

The distinctive characteristic of a DBR-LD is that when the pumping of the gain region is increased, due to heating, the gain spectrum red-shifts independent of the DBR spectrum. This also means that the laser undergoes longitudinal mode hops during pumping ramp-up. The lasing mode is typically the one with the highest DBR reflection over the whole operation range of the DBR-LD, up to the thermal roll-over of the gain.

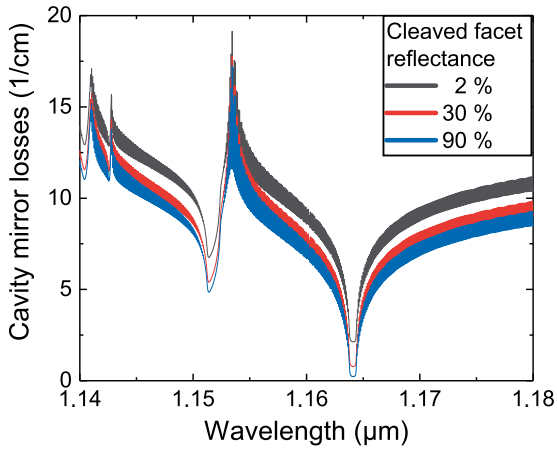


**Fig. 2.6** Simulated cavity mirror losses with one cleaved facet and one DBR mirror with multiple cleaved facet reflectances shown. The DBR grating period is 511 nm, the length of the grating 2 mm, the total length of the cavity 5 mm and the etching depth of the grating 50 nm above the waveguide. Simulation by Dr. Topi Uusitalo using CAMFR software [97].

## 2.5 Power and brightness scaling with tapered lasers

While the narrow ridge is good at suppressing unwanted horizontal modes, it limits the power scaling of the laser for several reasons, including spatial and spectral hole burning [98], catastrophic optical damage (COD), and thermal roll-over. Spatial hole burning, meaning that at high power levels the gain is depleted at certain spatial locations inside the cavity, is the result of a limited rate at which electron-hole pairs can be injected into the active region. Spectral hole burning means that gain at a certain wavelength range is depleted. COD is thermally induced damage to the laser facet due to the absorption of high-intensity light at the laser facet. Thermal roll-over is the effect that in CW mode the active region heats up due to pumping and the absorption of light, giving carriers more thermal energy to escape from QWs, which decreases the slope efficiency of the laser until the output power no longer increases even if pumping is increased. All these effects relate to the small transverse size of the gain region. In the growth direction, the beam is anyway quite narrow, since significantly increasing the vertical waveguide height would make the beam vertically multi-mode. Making the RWG wider would similarly make the beam horizontally multi-mode.

A solution to this problem, applied in this thesis, is to add a tapered section to

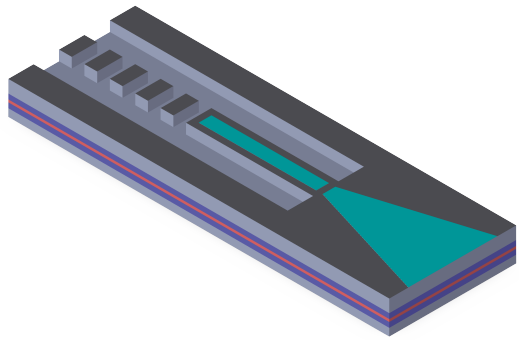

**Fig. 2.7** Schematic of a tapered DBR-LD. An unetched tapered region is situated in front of the RWG. Current is injected through the area highlighted with light blue colour. Separate injection currents may be applied to the RWG section and the tapered section to have more control over the operation of the device. The DBR grating at the back is unpumped, as in regular DBR-LD.

the front of the laser diode. The tapering is implemented by limiting the tapered section injection current to a wedge-shaped area. The structure is depicted in Fig. 2.7. Since there is no horizontal waveguiding in the tapered section to keep the beam confined, the beam exiting the waveguide expands horizontally inside the tapered section so that its width is increased by the time it reaches the facet, often by as much as hundred-fold, depending on the opening angle of the taper and the length of the tapered section. If designed and fabricated appropriately, the taper should maintain the beam quality provided by the RWG [99] making it, in this regard, superior compared to BA-LDs which are transversely multi-mode. On the other hand, the expanded mode size at the output facet allows more output power before COD becomes an issue, the larger mode size inside the tapered section pushes back the gain saturation power level since the optical field intensity is reduced, and thermal management reduces thermal roll-over effect due to increased surface area of the tapered section enabling higher heat conductivity.

From a beam optics point of view, the tapered DBR-LD forms an unstable resonator [99]. Only the optical field hitting close to the optical axis at the tapered facet contributes to feedback into the cavity, and rest of the reflected light dissipates off-axially into the component. The light transmitted at the facet on the other hand refracts further away from the optical axis due to the semiconductor having a higher refractive index than the surrounding air, making the far-field angle wider than the angle inside the tapered section. The result is that in the horizontal direction, the

divergence point of the emitted light appears to be inside the tapered section [100], while in the vertical direction the beam starts to diverge at the facet, making the beam astigmatic. The amount of astigmatism can vary at different operating conditions of the laser, complicating the design of optical systems using a tapered laser as the source.

A tapered laser provides a perfectly Gaussian beam only if the mode exiting the RWG section is resonating solely in the fundamental transverse mode and it expands in the tapered section without any perturbations in its wave front caused by variations of the refractive index. Issues with lasers containing tapered sections include self-focusing and filamentation that deteriorate beam quality. At high optical field intensities, spatial hole burning occurs which alters the refractive index of the material locally. This variation in the refractive index causes self-focusing of the optical wave and leads to filamentation [101]. Filamentation reduces the beam quality and thus is detrimental for the properties of the laser from application point of view. It has been reported that filamentation can be reduced by using a semiconductor layer structure with a low QW confinement factor resulting in low modal gain [101].

## 2.6 Beam quality and its influence to applications

The beam quality factor of a laser quantifies how well the laser beam can be collimated and focused. A Gaussian laser beam has the best possible beam quality and is called diffraction limited. The beam parameter product (BPP) of a Gaussian beam is constant and defined as

$$\theta\omega_0 = \frac{\lambda}{\pi}, \tag{2.9}$$

where $\theta$ is the beam divergence half-angle, $\omega_0$ is the beam waist radius, and $\lambda$ is the wavelength [55]. For non-Gaussian beams, the BPP is higher:

$$\theta\omega_0 = M^2\frac{\lambda}{\pi}, \tag{2.10}$$

where $M^2$ is the beam quality factor. For Gaussian beams, $M^2 = 1$. In case of beams with differing slow and fast axes, the slow and fast axis beam quality parameters can be presented separately as $M_x^2$ and $M_y^2$, respectively. The definition of the aforementioned parameters at the beam waist is shown in Fig. 2.8.

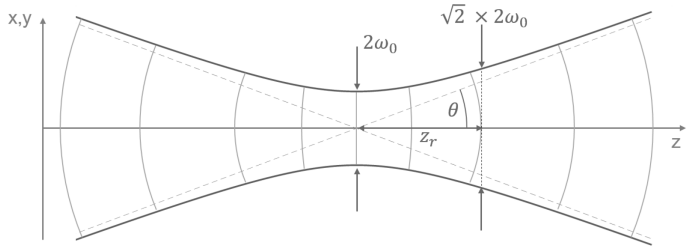


**Fig. 2.8** Schematic [102] of a laser beam around the beam waist and the parameters used to define beam properties. $z_r$ is the Rayleigh length defined as $z_r = \pi\omega_0^2/\lambda$.

In LIDAR applications, the beam quality is most critical for point-scanning implementations [37], and if a semiconductor laser is used as a seed laser for a fiber amplifier although in this case a high beam quality may not alone be sufficient [103]. In line scanning, a bar of BA-LDs is often used with multiple emitters side by side. This way the beam quality is vertically good (if the separate emitters are vertically single-mode), and the horizontal beam quality is not much of an issue because it only needs limited collimation due to the shape of the scanning line. In flash LIDAR the point is to illuminate the whole target area at once, so no tight focusing or collimation is needed.

For SHG, increased $M^2$ both reduces the nonlinear conversion efficiency and changes the optimal focusing conditions inside the nonlinear medium [104]. An estimate has been presented to calculate the obtained frequency doubled power $P_{SH}$ based on the slow and fast axis beam quality factors

$$P_{SH} = \eta_{bulk} L \frac{P_0^2}{M_x^2 M_y^2}, \tag{2.11}$$

where $\eta_{bulk}$ is the bulk crystal conversion efficiency (i.e. without any waveguide in the crystal) and $P_0^2$ is the injected optical power at the fundamental wavelength [105].

## 2.7 Power scaling with wavelength locked BA-DBR lasers

In some applications requiring wavelength locking but not high beam quality, a broad-area DBR (BA-DBR) laser diode is a viable option. With only one contact, its

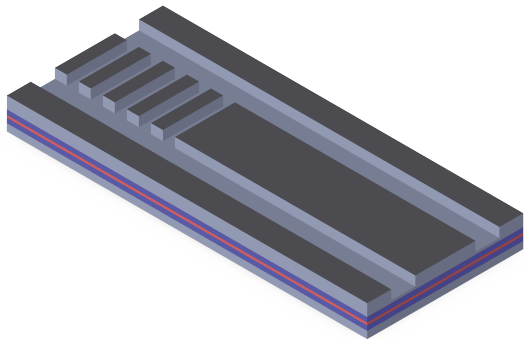

**Fig. 2.9** Schematic of a BA-DBR. The geometry is similar to the regular DBR-LD, except that the ridge is tens or hundreds of micrometers wide and thus transversely multi-mode.

packaging and operation is simpler than that of the tapered DBR-LD, and the wide cavity enables high output power. Since there is no need for lateral mode confinement as in regular DBR-LD, the RWG structure can be much wider increasing the mode volume and therefore the output power without a separate mode expansion section.

The far-field shapes of both the tapered DBR the BA-DBR are highly elliptical. Since the far-field width in one direction is primarily the result of diffraction, a narrow exit aperture results in a large divergence angle. For all lasers discussed in this thesis, the vertical size of the optical mode inside the laser follows from the waveguiding provided by the semiconductor layer structure. As a result, inside the laser the mode is very narrow in the vertical direction and thus the vertical (also known as fast axis) far field is wide. In the horizontal direction, the optical field width results from the geometry of the horizontal waveguide or the area where the current is injected if no waveguide is present. In the case of tapered DBR and BA-DBR, the optical field is approximately as wide as the current injection area, resulting in a narrow horizontal (i.e. slow axis) far field.

# 3 METHODS

Laser diode development is in many ways an iterative process, where initial components are usually designed based on simulations and previous experience, and then refined in successive development iterations until the desired performance level has been obtained. The components reported in peer-reviewed publications represent the tip of the iceberg in terms of the number of fabricated devices, with a large number of better or worse intermediary components left unreported.

An important aspect of laser diode development and research is characterizing the fabricated devices. In the research presented in this thesis, a semi-automated testing system was used to run a standard set of characterization methods that are generally applied to most fabricated laser samples. Besides the standardized measurements, special measurement setups were constructed when needed. This chapter outlines the standard measurement procedures and describes the advanced measurements that had to be designed specially for the diodes discussed in this thesis. Additionally, other aspects of the work that the author had a major contribution in are discussed.

## 3.1 Standard characterization methods

The basic characterization set that most devices undergo consists of three measurements: current–power–voltage (ILV), far field (FF) and spectrum. For these measurements, a dedicated, custom-built testing setup ("LDC5000") was used. It can perform these three tests automatically on any chip that is mounted on a compatible submount or heatsink, based on the parameters input by the operator. The measurements can be performed either in continuous wave (CW) or in pulsed mode, with a CW current limit of about 10 A to 12 A, a pulsed current limit of 15 A, and a minimum pulse length of 1 $\mu$s. With multiple integrated photodiodes and the option to use different spectrum analyzers the wavelength range spans from visible to over 2 $\mu$m.

The ILV curve describes how the output power and the operating voltage of the laser diode behave when the injection current is varied. The voltage behaviour can be used to assess the quality of the semiconductor structure or the metal-semiconductor junction, while the output power is often the most interesting parameter of the laser, and e.g. the roll-over point can be used to evaluate the gain saturation and thermal properties of the material and/or the ability of the packaging to provide sufficient cooling. Four-terminal sensing [106] is used in CW measurements in order to obtain more accurate voltage readings. The optical power is measured with calibrated photodiodes connected to a 100 mm integrating sphere by Labsphere. The available current sources are Keithley 2400 SMU, Arroyo 4320 LaserSource, Newport model 6000 laser diode controller, DEI PCX-7420 CW / Pulsed Laser Diode Driver, and Keithley 2520 Pulsed Laser Diode Test System. Research activities linked to tapered lasers required the development of new hardware and software interfaces and connection methods to the equipment in order to control the multi section lasers accordingly.

FF describes the angular distribution of the output power from the laser diode. In LDC5000 this is measured using a photodiode attached to a sweeping arm that rotates around the front hemisphere of the laser diode. Usually a single vertical and horizontal sweep is performed to obtain the FF of two orthogonal directions (along and perpendicular to the pn-junction), but the system also has the capability to measure a full hemisphere FF.

The spectrum measurement is based on the light hitting a diffraction grating that separates the different wavelengths, and then measuring the optical power in the spatial region corresponding to the desired wavelength. LDC5000 has an integrated optical spectrum analyzer Anritsu MS9710C for measurements in the wavelength range from 600 nm to 1750 nm and also an external interface that enables the connection of other spectrum analyzers as required.

## 3.2 Special characterization methods for this thesis

### 3.2.1 Higher pulse currents, shorter pulses, pulse measurements

One limitation of the LDC5000 measurement system is the maximum pulsed injection current. DEI PCX-7420 driver provides pulsed current up to 15 A, but BA-LDs

and tapered LDs can handle much higher injection currents in pulsed mode. Also in LDC5000 the current injection circuit is not optimized for short pulses which means that in the case of large, short pulses the shape of the pulse is distorted due to the inductance of the circuit.

The solution to this was to perform the measurements requiring short and/or high pulsed current in a tabletop setup using specialized drivers, Dr. Heller Elektronik HLD-500-30 and HLD-500-50. These drivers reach up to 50 A pulsed current and down to 5 ns pulse length. The drivers are originally designed to operate TO-can packaged components, so an adapter circuit board had to be constructed as an interposer between the driver and the submount-mounted LD. To avoid the issue with circuit induction ruining the pulse shape, the mounting of the driver was made as close to the chip as possible so that the printed circuit board (PCB) lead length was minimized, and the trace shape was optimized for low inductance. Also the operation of the driver itself was nontrivial, requiring two voltage sources, a signal generator to set the repetition rate, and an oscilloscope to monitor the output. The width of the pulses was set by rotating a miniature potentiometer on the driver. Fig. 3.1 shows the pulsed driver mounted on the tabletop characterization setup.

Another limitation of the LDC5000 system is the measurement of optical power in pulsed mode. In the standard setup, average optical power is measured and then the peak pulse power is approximated using the target duty cycle of the laser. This method becomes inaccurate with short pulses and high currents, when shape of the electrical and optical pulse is far from square-wave. When a more accurate measurement is desired, such as in [PubII], the measurement process is twofold: First, the average optical power is measured just as in the standard measurement procedure. Then, using the same laser parameters, the shape of the optical pulse is measured using a fast photodiode (in this thesis, a Thorlabs DET08CL 5 GHz detector was used) and an oscilloscope. The photodiode measurement gives the power profile in arbitrary units that can then be calibrated using the corresponding average optical power.

### 3.2.2 Characterization of multi-section diodes

Originally, LDC5000 was designed to characterize up to 2mm long single section chips. However, with increasing power targets and the goal to study multi-section ta-

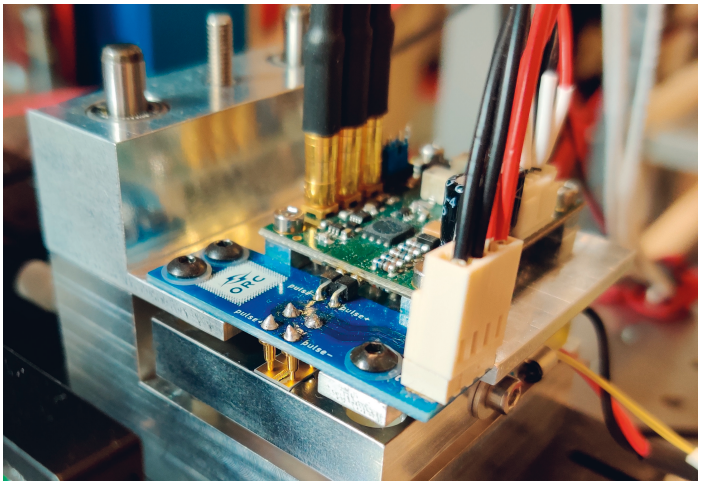

**Fig. 3.1** Dr. Heller Elektronik HLD-500-50 pulsed laser driver connected to a laser diode on submount using interposer PCB. The laser and the submount are visible on the bottom left side, held in place by four contact pins from the interposer PCB. Dr. Heller Elektronik PCB is in the back. On the right front side of the interposer PCB, DC connector for secondary laser contact is visible. The pulsed laser driver has five connectors: operating voltage, high voltage for output current adjustment, signal generator input for pulse triggering, trigger output for pulse frequency monitoring, and current output monitor.

pered devices, support for longer cavities and separate injection contacts was needed. For this end, in order to minimize the changes needed to the LDC5000's thermal management system, new heatsinks and current injection PCBs were designed and implemented to accommodate submounts supporting longer chips and the capability to inject multiple contacts with separate currents. Most of the designed tapered LDs and DBR-LDs use two contacts, one for the tapered section and one for the RWG section. The updated current injection design of LDC5000 enables either one of the contacts to be controlled programmatically during the measurement, and the other contact is DC biased manually with an external current driver. This capability was used to measure the data in Fig. 3 (variable RWG section current) and Fig. 4 (variable tapered section current) of [PubIII], for example. A selection of similar PCBs designed for multi-section laser tabletop characterization setups is shown in Fig. 3.2.

Multi-section measurement capability was also required in table top setups, and in this context a different challenge presented itself. The Dr. Heller driver that was used to inject short pulses failed to function when the tapered section of the laser was grounded, and since both the tapered section and the RWG section share a common

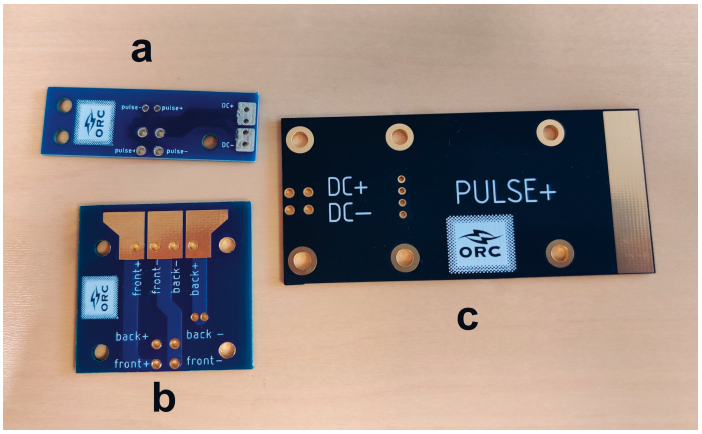


**Fig. 3.2** PCBs designed for multi-section laser tabletop characterization, compatible with the same laser mounting block system. a) Interposer PCB designed for Dr. Heller Elektronik HLD-500-50 pulsed laser driver with minimized lead lengths. b) DC injection PCB with soldered wire or Molex connector connectivity. c) PCB designed for future pulsed operation with currents up to 120 A. In all PCBs the connection with the laser diode submount is done with four contact pins whose mounting holes are visible on all boards.

n-side terminal, typical lab DC current laser drivers ground also the tapered section of the laser. This issue was circumvented by building a current source using Analog Technologies ATLS1A103D driver module in combination with the corresponding evaluation board. This module was driven using a floating voltage power supply to prevent grounding, enabling the DC bias of the RWG section while the Dr. Heller driver was used to operate the tapered section.

### 3.2.3 Robust tabletop laser mounting blocks

In tabletop measurements, the laser diode has to be mounted securely in place and since the contact areas of the used AlN submounts are small (especially in multi-contact operation), the spatial tolerances for mounting the submount and connecting the current injection circuit are small. Also the thermal management of the diode must be considered in case high current CW measurements are performed. To this end, a new design of a laser mounting block acting as a heat sink to the submount was created. The platform on which the laser was connected is modular, allowing the attachment of both heatsink and submount mounted chips, and only the alignment sheet metal piece has to be redesigned in case a new submount design is taken into

use. For thermal management a thermoelectric cooler in combination with AD590 temperature sensor is used for fine tuning, while a closed water loop and chiller are used to remove the excess heat from the laser and TEC. For the current injection, a twin bearing mounted lid is used to lower a PCB with contact pins on the submount. With Dr. Heller drivers, the whole driver is mounted on the lid to minimize the lead distance and induction, while with regular drivers the PCB has Molex connectors for easy usability. Compared to previous metal-on-metal or metal-on-plastic sliding designs, the bearings provide a smoother range of motion that helps to ensure that the contact pins hit their designated pads and do not damage the chip or the bonding wires. Finally, if a heatsink-mounted laser is used with the block, there is an alignment screw that allows the operator to adjust the lateral position of the heatsink to compensate for the mounting tolerances that arise from the manual mounting of the submount on the heatsink. A mounting block with submount measurement configuration is shown on the left side in Fig. 3.3.

### 3.2.4 Beam quality measurement

Perhaps the single most challenging characterization setup involved was the beam quality measurement system. The methodology for beam quality measurement of various beam types is standardized in [107–109].

Apparently the simplest way that the beam quality could be characterized would be to use a photosensitive pixel array such as a CCD. The detector would be moved along the beam axis, on both sides of a focused beam (or often in practice the detector stays in place and the beam focus is moved), and the pixel intensity corresponding to the spatial power distribution perpendicular to the optical axis would be measured. From this distribution, the beam quality could be calculated using the second order moments method.

The issue in this case was that since the 1.5 μm wavelength region is far above the silicon band gap wavelength, the beam from these lasers is invisible to inexpensive CCD cameras. InGaAs arrays on the other hand, as explained before, are highly expensive. We tested Bobcat 320 InGaAs beam profiler from Xenics NV for beam characterization, but this camera had an uncoated glass window sealing the detector array, and it resulted in an interference pattern shown in Fig. 3.4 around the beam waist that ruined the measurement.

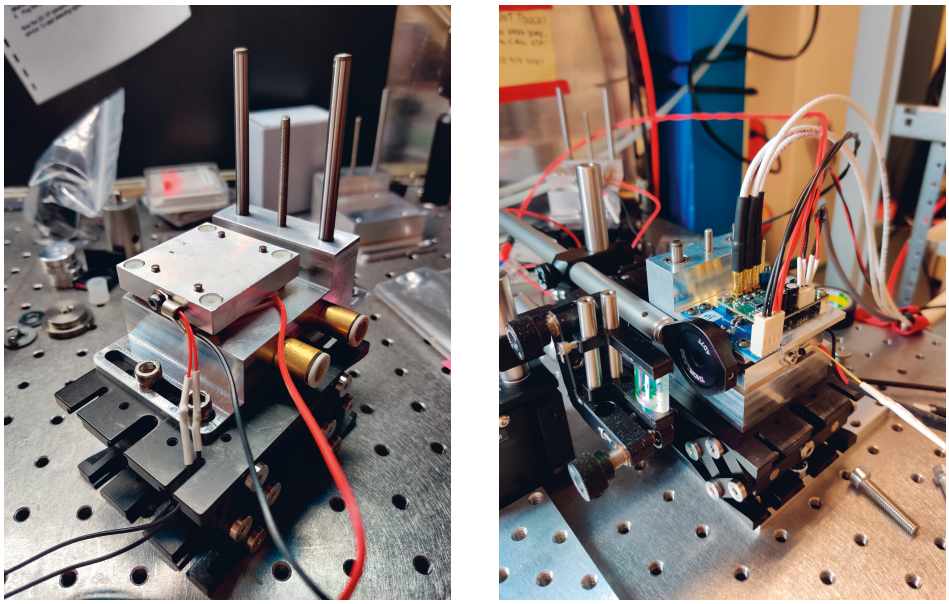

**Fig. 3.3** Left: Laser mounting block with top part removed. The block is mounted on a lab jack for coarse height adjustment. Water cooling connectors are shown on the bottom right side, AD590 temperature sensor on the top left side. Wires going to a thermoelectric element, used for temperature fine tuning, are shown in the middle. On the back there are two guide rods for the upper, bearing mounted part and a threaded rod for fastening. Right: Mounting block positioned for M2 measurement. Dr. Heller Elektronik HLD-500-50 laser diode driver is mounted on top. In front of the block there is first an aspheric lens for fast axis collimation and a larger acylindrical lens for slow axis collimation.

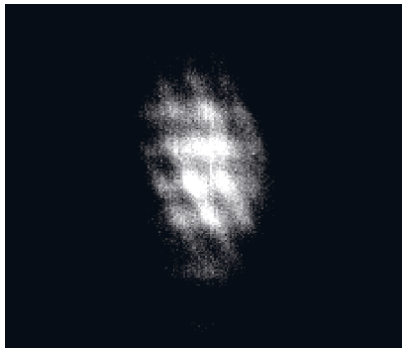

**Fig. 3.4** Interference around beam waist preventing beam quality measurement using Bobcat 320 InGaAs camera from Xenics. Image taken with beam perpendicular to the camera detector. The height of the pattern is about 2.5 mm and the width about 1.5 mm.

Next, a pyroelectric camera Pyrocam III from Spiricon was tried, but this attempt failed due to a more trivial issue. The camera hardware was somewhat outdated, and while the pyroelectric array was perfectly functional, no way was found to interface it with the measurement PC due to its obsolete IEEE 1394 Firewire connector.

Finally we settled on Thorlabs BP209-IR/M scanning slit beam profiler in conjunction with Thorlabs M2MS M2 measurement system. This posed some limitations on the measurement parameters, such as a lower limit of 200 kHz for the pulse repetition rate. The scanning slit system with two perpendicular slits also only provides intensity distribution data on two perpendicular axes, and not in full 2D array as a camera would. The benefit of the system was that Thorlabs' automatic motorized stage control and data acquisition could be used. However, for some reason Thorlabs' system only had the option to perform $1/e^2$ M2 analysis, so manual analysis was required to obtain the desired D4$\sigma$ results. Besides the measurements, we simulated the measurement set-up in BeamXPert optics simulation software that could be used to design the system in a way that the beam is correctly focused in the beam profiler with an acceptable beam size and waist but also to check if the selected lenses or their imperfect placement could deteriorate the beam quality.

The beam quality measurement setup consisted of the following parts, and is depicted in Fig. 3.5 along with an example M2 measurement:

- Laser and mount. Dr. Heller Elektronik HLD 500-50 pulsed current driver, Analog Technologies ATLS1A103 DC laser driver, thermoelectic cooler and water cooling circulation for temperature control.
- Fast axis collimation. C-coated aspheric lens with 3.10 mm effective focal length (EFL), AMS Technologies (note: circular lens so also slow axis was affected). Short EFL to limit beam expansion in fast axis direction and in order to have a high numerical aperture (NA[1]) to limit the effect of the optics on the measurement.
- Slow axis collimation. C-coated acylindrical lens with 15 mm EFL from Asphericon GmbH. Long EFL so that there was enough space for the lens and the beam had comparable size both in slow and fast axis directions after collimation. The first three parts of the setup are shown on the right side in Fig. 3.3.

[1]NA $= n \sin\theta$, where $n$ is the refractive index of the medium and $\theta$ is the maximum acceptance half-angle of the lens.

- Beam expander (if needed). In some cases, the beam diameter was too small for the Thorlabs M2 measurement system, so Thorlabs GBE05-C 5X beam expander was placed in path of the collimated beam. On the other hand, in some other cases using the expander caused the beam to clip.
- Focusing lens. C-coated achromatic doublet lens with 150 mm EFL, Thorlabs, was used instead of the supplied 200 mm EFL lens. Achromatic lenses were used even though chromatic aberration is not an issue, since the manufacturer specifications for the off-axial performance of the specific lens type was better than for comparable aspherical lenses. Reduction of the EFL makes the focus tighter so it was possible to use smaller input beam diameters.
- Variable length optical path unit. Thorlabs M2MS measurement system. Able to sweep the optical path between the input and output apertures from 50 mm to 250 mm.
- Detector. Thorlabs BP209-IR/M scanning slit detector with wavelength range from 900 nm to 1700 nm.

The M2 measurement followed these steps:

1. Collimate the beam. This was done by first adjusting the aspheric lens so that the fast axis direction was collimated, and then adjusting the second lens so that also slow axis direction was collimated, using an IR card. The secondary lens was cylindrical, so it did not affect the fast axis collimation.
2. Roughly align the M2MS system. The collimated beam aimed at the input aperture, and the system was set for continuous sweep. The M2MS system was adjusted until the detector showed that the spot remained roughly stationary throughout the sweep cycle.
3. Insert focusing lens and tune alignment. Inserting the focusing lens in front of the input aperture often had a large impact on the alignment, so it had to be redone. However, the focusing lens was mounted on an X–Y-stage in a plane perpendicular to the optical axis, so this made adjustment easier.
4. Adjust the optical path limits so that the beam waist is roughly in the center of the sweep.

Although these steps sound simple and straightforward, measuring the M2 was often a struggle. Sometimes two successive measurements without seemingly any dif-

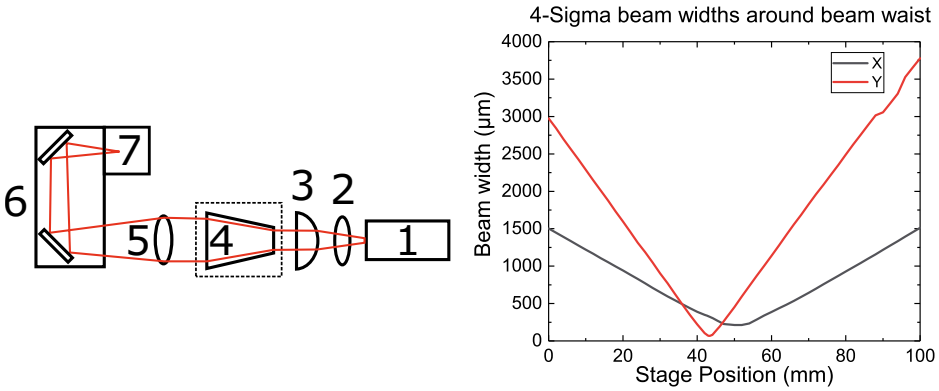


**Fig. 3.5** Left: M2 measurement setup schematic: 1) laser; 2) fast axis collimator lens; 3) slow axis collimator lens; 4) beam expander (if needed); 5) focusing lens; 6) variable length optical path system; 7) detector. Right: Beam width measurement of 1500 nm tapered DBR laser in CW mode with 3 A taper injection current and 200 mA RWG injection current. M2 values calculated from this are $M_X^2 = 3.6$ and $M_Y^2 = 2.3$. Astigmatism, as seen in the figure, was a common problem while performing these measurements.

ference in the alignment or collimation yielded different results, and compared with e.g. ILV measurement it was much more difficult to feel satisfied that a particular measurement was done in a comprehensive and satisfactory way. Usually the same measurement was done iteratively until no better result could be obtained, and this was the result that was assumed to be correct. This approach assumes that the misalignment of optical components may result in a reduction of the beam quality but not an improvement. This hypothesis we also studied empirically with BeamXPert-software, and it appears valid. In this respect the reported M2 values should be considered worst case estimates.

## 3.3 Other developed methods

### 3.3.1 Photolithography and nanoimprint lithography mask design

Lithography is a common tool used in semiconductor processing. It denotes a number of techniques for manipulating the surface topography of a semiconductor wafer in order to create desired surface structures, such as waveguides or grating lines for

optical functionality and contact pads and insulators for electrical interfacing. All lithography used in the fabrication of the devices reported in this thesis involves optically active polymer spread on top of the wafer. The polymer is then either selectively irradiated with ultraviolet (UV) light (photolithography) or mechanically distributed and hardened with UV light (nanoimprint lithography, NIL) to create a mask that is then used in an etching process. The lithography method of choice for each case depends on the size of the target features: the wavelength of the UV light presents a resolution limit on the feature size for photolithography, and smaller features, such as grating lines, have to be fabricated using NIL.

Both photolithography and NIL utilize lithography masks in the laser fabrication process. Photolithography masks are glass plates coated with a thin metal layer corresponding to the shape of the target etching pattern: the metal blocks the UV light from interacting with the photosensitive polymer in the chosen positions. NIL masks, or templates, are silicon wafers with a desired surface geometry fabricated using electron beam lithography. These masks are used to create a polymer-on-glass stamp, that is then used to perform the actual contact lithography in the semiconductor process. In fabrication processes involving DBR gratings both lithography methods are used in combination.

The lithography masks can contain a very large number of features. Especially NIL masks, depending on the layout, the grating period, and component size, may contain hundreds of thousands or even millions of individual grating lines. Also photolithography masks have great complexity, since each separate photolithography step is associated with a separate mask layer, and during semiconductor processing all consecutive layers have to be aligned closely. For these reasons, special care has to be taken while designing and implementing the masks. For the masks used in this thesis, Autocad software by Autodesk Inc. was used in the drawing or the masks, LinkCAD by Bay Technology for logical layer operations, and KLayout by Matthias Köfferlein for mask inspection.

The author of this thesis participated in the mask design and was primarily responsible for mask file design and mask procurement. The mask design decisions, such as taper opening angle and length, RWG width and length, current limiting opening width, and cavity spoiling elements, were made initially based on simulations, previous experience and/or research published by others, and refined iteratively if necessary. The design also factors in considerations related to different as-

pects of manufacturing including, for example, optical parameters, wafer fabrication technology constraints, and mask manufacturing limits and tolerances. Usually each fabrication batch contained DBR components with slightly differing grating periods due to uncertainty in effective refractive index or peak gain wavelength. Since the masks, especially NIL masks, were rather expensive and often had long lead times, the mask drawings had to be implemented without errors. For this, a workflow of first designing all the mask layers of the individual component variants and then tiling these variants to fill the target mask area was developed. Due to a minimum length of about 500 μm required between neighbouring cleaved semiconductor facet planes and inaccuracy in the cleaving position, special overlapped tiling between adjacent component rows on the wafer was used to maximize the number of components that could be fabricated from the limited wafer supply. Improvements were made in the mask alignment markers to facilitate processing, and also Vernier scale [110] and Moiré patterns [111] were tested to improve alignment accuracy (with credit to Mr. Joel Salmi for first bringing the concept up). Various mask drawing innovations are depicted in Fig. 3.6. Symbolic array tiling was also required due to the large number of individual grating elements and limited computer memory. After drawing, the masks were checked for errors by both the author and others involved in the mask design process. The photolithography masks were purchased from Compugraphics International Ltd. The NIL masks were fabricated by the University of Eastern Finland, partly in collaboration under the program PREIN – The Flagship on Photonics Research and Innovation. The quality inspection of incoming masks was done by the same people who performed the semiconductor processing.

### 3.3.2 Antireflection coatings

AR coatings are an important part of many optical devices, including semiconductor lasers. The as-cleaved semiconductor facet reflects about 30 % of the light. When using DBR gratings, the facet on the side of the DBR grating has to reflect very little or the near-uniform reflectance of the facet ruins the wavelength-sensitive reflectance of the grating. Also the reflectance of the non-DBR side facet should be reduced so that more light can be extracted from the cavity and that most of the exiting light will be emitted from the front instead of the DBR side. However too small front facet reflectivity provides insufficient feedback to the cavity which raises the threshold


**Fig. 3.6** The mask pictures are not to scale relative to each other. Top left: Row and column numbers next to alignment markers on each mask layer. Masks often have (partial) translational symmetry on some layers, and sometimes alignment markers from a wrong row or column might be used accidentally in device processing, resulting in the failure of the outermost components on the mask or even the whole wafer. Indexing the alignment markers prevents this kind of mistake. Top right: Vernier scale and Moiré rings on mask layers to increase alignment accuracy. The success of these approaches was not tested conclusively. Bottom: Border between two adjacent component bars on the mask. NIL layer shown in red, metallization layer shown in yellow. The bars can be separated by cleaving anywhere between the top and bottom metals, and the overlap between the DBR grating (top bar) and RWG (bottom bar) ensures that both bars remain functional. This way a wasted spacer region of about 500 µm can be avoided between adjacent bars.

current too high.

At the start of the work included in this thesis, there were two available AR coating methods available for our group: crude plasma enhanced chemical vapour deposition (PECVD) system and more elegant electron beam evaporation based dielectric coating system. PECVD was primarily used in semiconductor processing e.g. to create etching masks, and was quite poor for accurate optical coatings due to high anisotrophy and feature size dependent growth rates, but it could be used to create inexact coatings when the tolerance for the reflectivity was large. The dielec-

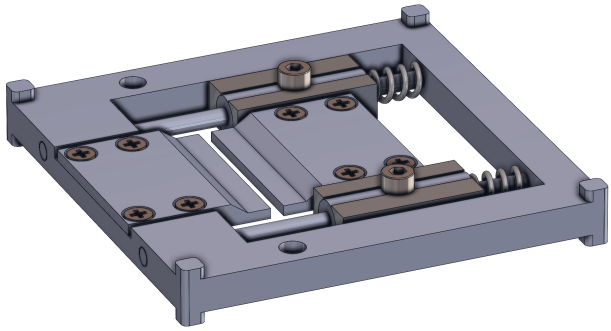

**Fig. 3.7** Spring-loaded, bearing mounted laser bar holder for the IBS system. Bars are mounted vertically between the clamps shown in the middle. The clamps are interchangeable to accommodate bars of different lengths. The bars are loaded using a robust loading block for convenience, and up to four of these holders can be inserted simultaneously in the IBS system for coating. The size of the frame is 75 mm by 75 mm by 10 mm.

tric coater, on the other hand, could be used even in complex vertical cavity surface emitting laser (VCSEL) top DBR mirrors with high accuracy, but its operation was difficult, calibration coatings were needed before every coating run, and it required constant operator attention and skill during the long coating runs. For these reasons new coating methods had to be found.

First, atomic layer deposition [112] was tested in collaboration with Prof. Mika Valden's surface science group [PubI]. While slow, it had the promise of highly isotropic growth rate and the coating process could be automated. However, the refractive index of the grown layers changed over time and thus calibration coatings were required, and it was only possible to coat packaged components due to the physical constraints of the system and the lack of the ability to only focus the film growth on the facets.

By the time the components used in [PubII] were being fabricated, we had access to NAVIGATOR 700 ion beam sputtering (IBS) system by Cutting Edge Coatings GmbH. This system had the advantage that the film growth could be monitored optically in real time, largely eliminating the need for constant calibration coatings. It was also much faster compared to the ALD system, and due to the anisotrophy of the growth and size of the process chamber, bar stacks could be coated with ease. This has been the primary coating method since.

While the author of this thesis did not operate the coating instruments, he designed most of the used coatings (Essential Macleod software by Thin Film Center

Inc.), measured the calibration coatings used in the ALD processes (Lambda 1050 spectrophotometer by PerkinElmer Inc.), and designed and procured most of the CNC-machined mounted device and bar stack holder assemblies used in the ALD and IBS coating systems. A schematic of the finished design for the IBS bar holder is shown in Fig. 3.7. The used 3D design software was SolidWorks by Dassault Systèmes.

# 4 RESULTS

## 4.1 Wavelength locked 1180 nm laser diodes

The motivation and application drive behind 1180 nm laser diode research was the use of SHG to gain access to the yellow–orange light around 590 nm which is challenging to obtain through direct emission due to limitations in available semiconductor materials. Since efficient SHG requires high power, good beam quality, and narrow emission linewidth for the pump beam, DBR-LD and tapered DBR-LD were the chosen approaches. BA-DBR was not chosen due to its fundamentally poor lateral beam quality.

Often gain below 1.2 μm is achieved using the GaInAs/GaAs material system. However, as the wavelength becomes longer, the In content of the active region has to be increased which increases the strain and lowers the efficiency and life time of the laser. Our key advantage for this wavelength range was the use of the dilute nitride GaInNAs material system where a small amount of nitrogen reduces the strain and increases the carrier confinement. Lifetime studies of the 1180 nm DBR lasers that this thesis focuses on are not presented in this thesis but this topic has been reported by our group [113]. Here preliminary tests showed that structures allowed 2000 h operation at high power without degradation.

### 4.1.1 1180 nm DBR-LD results

DBR-LD laser diodes emitting at 1180 nm and based on GaInNAs material system were first presented in [PubIV] and further improved in [PubI]. The original motivation for using the dilute nitride material system in [PubIV] was to prove it as a viable alternative to the more common InGaAs material system that has disadvantages near 1.2 μm wavelength due to high strain. The material used in [PubI] was

almost identical to the one in [PubIV] with only minor fine tuning of the emission wavelength to more closely match the desired grating resonance wavelength.

[PubIV] focused on the procedures and parameters of the epitaxial growth of the GaInNAs material, characterization of the basic material properties through the use of oxide-stripe laser diodes, performance of the material at elevated operating temperatures, and the spectral and current–power–voltage (ILV) characterization of the fabricated DBR-LDs. The key material characteristics for laser applications were a threshold current density of 220 A cm$^{-2}$ (83 μm x 1600 μm uncoated oxide-stripe laser) and characteristic temperatures $T_0 = 110$ K and $T_1 = 160$ K.[1] The key DBR-LD characteristics were 340 mW CW output power at 20 °C operating temperature, only 30 % drop in output power when the temperature was increased to 80 °C, 50 pm spectrum FWHM (limited by the spectrum analyzer), and a temperature-induced center wavelength shift of 0.1 nm °C$^{-1}$.

While [PubI] was mainly focused on tapered devices, it also reported improvements to untapered DBR-LD performance. The main difference between the DBR-LDs in [PubI] and [PubIV] were that in the components reported in [PubI] the QW gain was shifted closer to the grating resonance by increasing the In content. The closer the gain maximum and the grating resonance wavelength are, the higher gain is available at the emission wavelength and performance is increased. [PubI] showed 655 mW maximum CW output power for the DBR-LD, significantly higher than the 340 mW in [PubIV]. Also the output power at equivalent injection current 1200 mA is higher at 435 mW. The trade-off, however, is that having the gain at a shorter wavelength than the grating resonance frequency provides tolerance to temperature increase although it might not provide highest efficiency at room temperature. This is because the gain shifts in wavelength with roughly five times higher rate than the grating resonance, minimizing the detuning between the gain and resonance, and the laser is most efficient when this detuning is zero. This effect also showed in the results: the DBR-LD devices in [PubI] showed 39 % decrease in output power already at 60 °C, while the devices in [PubIV] showed 30 % decrease at 80 °C. Measured spectral FWHM and temperature induced center wavelength shift were alike in both publications. A later publication, not included in this thesis, showed that the linewidth of these lasers was in 100 kHz to 250 kHz range [113].

[1] $T_0$ describes the relationship between the threshold current $I_{th}$ and the operating temperature as $I_{th}(T) = I_0 \exp(T/T_0)$ and $T_1$ is analogous for slope efficiency $SE = \Delta P_{opt}/\Delta I$.

### 4.1.2 1180 nm tapered DBR-LD results

Tapered 1180 nm DBR-LDs were studied in [PubI]. For the measurements, they were operated in CW mode by injecting a constant current 350 mA in the RWG section and the injection current of the tapered section was swept up to 10 A. As expected, the output power (4.04 W) exceeded the output power of the untapered component (655 mW). At the maximum power, the spectral FWHM of the tapered DBR-LD was 270 pm.

The beam quality factor of the 1180 nm tapered DBR lasers has not been reported in the publications included in this thesis, but they have been included in the M.Sc. thesis of Samu-Pekka Ojanen [114]. In the tapered section injection current range from 2 A to 12 A the slow axis M2 values were in the range from 6 to 30. These beam qualities are insufficient e.g. for effective coupling into fiber or SHG crystal. The primary cause for the high values lies in the epilayer structure of the material that was not originally optimized for tapered laser diodes. The used material had a relatively high QW confinement factor $\Gamma = 1.00\%$ which results in self-focusing and filamentation of the beam in the tapered section [101]. Later, unpublished measurements from tapered DBR components fabricated from a different 1150 nm material, designed specifically with tapered components in mind, have provided much better M2 values in the range from 1.5 to 2.0. The comparison between the structure of the two materials is shown in table 4.1. The QW confinement factor of the newer material is 0.5 % and it has an asymmetric waveguide structure, explaining the improved beam quality. Additionally, introduction of asymmetry in the waveguide structure steers the optical intensity away from the p-side and brings the active region closer to the p-side. The former reduces the optical losses caused by the light coupling with holes (that have heavier effective mass compared to electrons), and the latter reduces the electrical resistance. [115] Another improvement included in the 1150 nm lasers are current confining shallow etches around the tapered section, reducing the spread of current and improving the efficiency. Some other groups have used ion implantation to limit current in a similar context [116].

**Table 4.1** The 1180 nm epilayer structure used in [PubI, PubIV] and a newer 1150 nm design with focus on good tapered laser performance.

| | Thickness in nm | |
|---|---|---|
| layer | 1180 nm epi | 1150 nm epi |
| p-GaAs contact | 200 | 200 |
| p-AlGaAs cladding | 1200 | 1400 |
| p-GaAs waveguide | 500 | 1010 |
| GaIn(N)As QW | 1 x 7 | 2 x 6.5 |
| n-GaAs waveguide | 500 | 1970 |
| n-AlGaAs cladding | 1300 | 1850 |
| n-GaAs buffer | 200 | 1000 |

## 4.2 Wavelength locked 1500 nm laser diodes

The main motivation behind 1500 nm lasers was their intended use in eye-safe LIDAR applications. Unlike in common LIDAR systems operating at submicron wavelengths, light around 1500 nm wavelength is absorbed before the retina of the eye and thus has relaxed radiation safety power limits. The increased output power would enable a greater operating range and performance in challenging weather conditions such as rain or fog. By making the emission wavelength band narrower using integrated gratings, the signal-to-noise ratio could be improved by using narrow band filters in the LIDAR receiver side to block most of the ambient solar radiation.

### 4.2.1 1500 nm BA-LD results

As with 1180 nm lasers, the development of 1500 nm lasers started off with untapered components. [PubII] focuses on the development of the BA-DBR-LD and compares it with corresponding BA-FP-LD at the same wavelength. The broad area component was selected as the starting point due to its applicability in LIDAR systems since it offers increased emission power compared to narrow waveguide DBR-LD. The lasers were fabricated using InGaAsP large optical cavity (LOC) material that was designed with high saturation power levels and pulsed operation in mind. Most of the characterization was done using sub-μs pulsing, since also in actual LI-

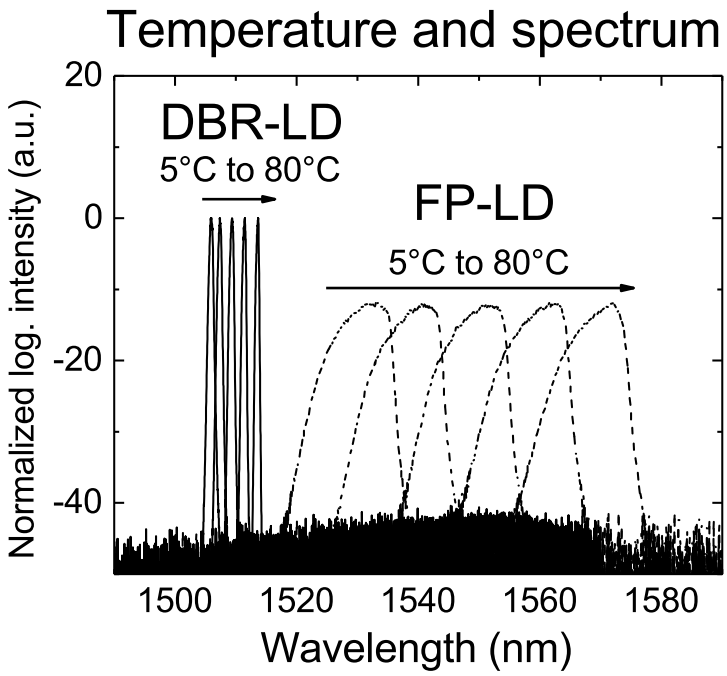


**Fig. 4.1** Effect of the DBR grating on the emission wavelength under changing mount temperature using the same semiconductor material, same ridge width and same cavity length. With the DBR as one of the end mirrors, the emission wavelength shifts at a rate of 0.1 nm/°C while in the case of two cleaved facet mirrors the rate of shift is 0.5 nm/°C. The grating also offsets the emission wavelength by up to tens of nanometres from the gain maximum. Both the DBR-LDs and RWG-LDs were operated with 15 kA pulsed current at 1 % duty cycle and 1 µs pulse length and the spectra were measured with the same system. Adapted from [PubII].

DAR systems nanosecond scale pulses would be used due to the relationship between LIDAR depth resolution and the length of the pulse. A peak output power of 6.1 W was reached with the BA-DBR-LD. A corresponding BA-FP-LD reached 6.6 W output power, showing that the penalty for using a grating end mirror was not too great, especially when the benefits are considered: the DBR laser had 0.3 nm spectral FWHM and 0.1 nm/°C peak emission wavelength shift, compared to corresponding values 6.9 nm and 0.5 nm/°C for the FP laser. Fig. 4.1 shows the stabilizing effect the grating provides to the center emission wavelength when the mount temperature is changed.

### 4.2.2 1500 nm tapered DBR-LD results

Tapered 1500 nm DBR-LDs were studied in [PubIII]. They were fabricated using a high modal gain InAlGaAs/InP material that was originally designed primarily for tapered component CW mode operation. In CW mode the lasers reached an output power of 770 mW and in pulsed mode a peak output power of 4.6 W with a FWHM spectral linewidth of 250 pm was achieved. The temperature change induced peak wavelength shift was the same as in 1180 nm DBR lasers, 0.1 nm/°C.

The material used for these lasers suffers from the same issue as the 1180 nm material that it was not originally designed for use in high power tapered devices, and its confinement factor is quite high. This results in high M2 values both in CW (measured $M_X^2$ up to 10) and pulsed mode (measured $M_X^2$ up to 45). The structure of the material is outlined in table 4.2.

**Table 4.2** The 1500 nm epilayer structure used in [PubIII].

| layer | thickness / nm |
|---|---|
| p-InGaAs contact | 150 |
| p-InP cladding | 1570 |
| n-InAlAs barrier | 50 |
| p-InAlGaAs waveguide | 85 |
| Active region | 4x InAlGaAs QW à 7 nm<br>3x InAlGaAs barrier à 10 nm |
| n-InAlGaAs waveguide | 85 |
| n-InAlAs barrier | 100 |
| n-InP buffer/cladding | 500 |

Improved results in both power and beam quality have been obtained using recently developed [117] epi material with asymmetric structure to reduce the optical losses and the gain region confinement factor ($\Gamma_{asym} = 4.1\,\%$ compared to previous $\Gamma_{\mathrm{PubIII}} = 4.6\,\%$). This material has an increased waveguide thickness 1.8 μm compared to 0.17 μm of the material in [PubIII], and a bulk active region instead of MQW. We also proved that this structure allows state-of-the-art broad area lasers reaching up to 18 W of peak power [118]. When applied in a tapered RWG laser, an improved beam quality of about 7 at 15 A injection current was obtained [119] (see Fig. 4.2,

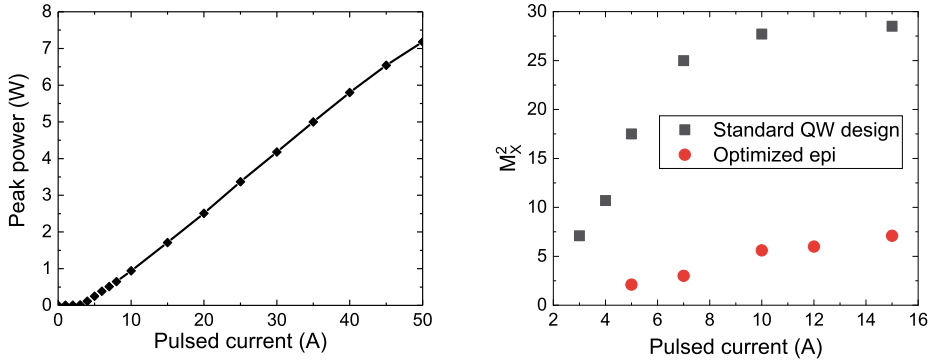


**Fig. 4.2** Left: Peak pulsed output power from 1.5 µm tapered RWG lasers with optimized epitaxial structure. Right: Comparison between pulsed beam quality of tapered RWG lasers with standard QW design (as used in [PubIII]) and optimized structure.

right side). Moreover, we later demonstrated up to 7.5 W power with 50 A pulsed current from these tapered RWG sources (see Fig. 4.2, left side). We also studied these lasers at higher temperatures under high current conditions. Results indicated that, due to typical carrier leakage, the output power was reduced but the beam quality improved. This supports the idea that beam quality degradation at high power is mostly linked to high optical power rather than to high current.

# 5 CONCLUSIONS

They key motivators behind the research presented in this thesis were the need for compact, high-power, high-brightness, wavelength locked laser diodes for eye-safe automotive LIDAR (light detection and ranging) and frequency doubled yellow–orange light. For LIDAR, 1.5 μm wavelength range was selected due to its relaxed radiation safety power limits compared to more commonly used 900 nm wavelength band and because this wavelength band allows easy amplification with erbium-doped fiber amplifier (EDFA). For frequency doubling applications, the biggest field of interest was medical use which would benefit from 590 nm laser sources, setting our seed laser target at 1180 nm before frequency doubling.

Various LIDAR implementations have different requirements on the laser source, especially the beam quality. For this reason, tapered distributed Bragg reflector (tapered DBR) lasers and broad-area distributed Bragg reflector (BA-DBR) lasers were studied at 1.5 μm wavelength. Tapered DBR lasers provide good beam quality for point scanning approaches, while BA-DBR lasers have higher output power and more simple operation for line scanning or flash illumination. Frequency doubling requires good beam quality, so tapered DBR lasers were studied at 1180 nm.

The focus of this thesis was in device characterization. This presented some unique challenges compared to "simple" diode lasers, that are commonly characterized. The components are quite large in size and may have multiple electrical contacts, requiring novel engineering solutions to facilitate characterization processes. Also the maximum injection currents were relatively large, and combined with the need for short pulses, presented technical challenges to overcome. The 1.5 μm wavelength range was difficult to characterize, especially regarding the beam quality, since silicon based CCD cameras were not an option and the tested InGaAs based arrays did not perform properly. Besides this, commercially available scanning slit beam profilers imposed restrictions on the pulse parameters that could be characterized.

Once challenges were overcome, state-of-the-art results were obtained from DBR,

tapered DBR and BA-DBR lasers. 1180 nm DBR laser without power scaling produced up to 0.65 W of continuous-wave (CW) power while tapered DBRs produced a CW output power of 4.04 W with a spectral full width at half-maximum (FWHM) of 270 pm. 1.5 μm tapered DBRs and BA-DBRs produced pulsed output powers of 4.6 W and 6.1 W and spectral FWHMs of 250 pm and 0.3 nm, respectively. Wavelength locking functioned as expected, reducing temperature induced wavelength shift to 0.1 nm/°C, while e.g. in unlocked 1.5 μm broad-area Fabry-Perot (BA-FP) lasers it was 0.5 nm/°C.

It was challenging to demonstrate high beam quality from tapered lasers. The first demonstrated $M_X^2$ beam quality of the 1.5 μm tapered DBR lasers was up to 10 in CW mode and up to 45 in pulsed mode, and also 1180 nm tapered DBR lasers were found to be sub-optimal at up to 30. A major limitation in these lasers was linked to the epi-design that was later improved resulting in much better results. Enhanced epi-designs allowed nearly perfect CW $M_X^2$ values at 1150 nm and ns-pulses at 1.5 μm with a beam quality factor around 7. The improved 1.5 μm epi-design was also able to mitigate the optical losses of the cavity, allowing current source limited output powers up to 7.5 W from tapered ridge waveguide (RWG) lasers. Achieved beam quality factor of 7 allows much higher spatial resolution scanning than comparable broad area lasers but it is still impossible to couple this beam into a single mode EDFA fiber with high efficiency. The future plan is to further improve the beam quality by testing shorter cavity designs, and to test different types of cavity layouts that could further suppress the formation of higher order modes in the tapered cavity while operating in the ns-domain.

In general, research in the field of high-power and high-brightness laser diodes, especially at these wavelengths, is bound to expand due to the development of the applications. The automotive industry is undergoing rapid changes, and while the largest hype may be in the field of electric vehicles, there is also great interest in autonomous driving and LIDAR. On the other hand, the aging population in first world countries and the development of genetic medicine present the need for compact and cost-effective yellow–orange laser sources e.g. in the fields of dermatology and DNA sequencing.

# REFERENCES


[1] T. Maiman. Stimulated optical radiation in ruby. *Nature* 187 (1960), 193–194. DOI: 10.1038/187493a0.

[2] J. Mazumder. Laser Welding: State of the Art Review. *The Journal of The Minerals, Metals & Materials Society* 34 (1982), 16–24. DOI: 10.1007/BF03338045.

[3] M. Arumugam. Optical fiber communication–An overview. *The Journal of The Minerals, Metals & Materials Society* 57 (2001), 849–869. DOI: 10.1007/s12043-001-0003-2.

[4] Q. Peng, A. Juzeniene, J. Chen, L. O. Svaasand, T. Warloe, K.-E. Giercksky and J. Moan. Lasers in medicine. *Reports on Progress in Physics* 71.5 (2008), 056701. DOI: 10.1088/0034-4885/71/5/056701.

[5] R. F. Curl and F. K. Tittel. Tunable infrared laser spectroscopy. *Annual Reports Section "C" (Physical Chemistry)* 98 (2002), 219–272. DOI: 10.1039/B111194A.

[6] Z. Xu and Y. Bi. Large laser projection displays utilizing all-solid-state RGB lasers. *Light-Emitting Diode Materials and Devices*. Ed. by G. Yu, C. Chen and C. Lee. Vol. 5632. International Society for Optics and Photonics. SPIE, 2005, 115–122. DOI: 10.1117/12.604542.

[7] G. O'Regan. Xerox PARC. *Pillars of Computing: A Compendium of Select, Pivotal Technology Firms*. Cham: Springer International Publishing, 2015, 225–229. ISBN: 978-3-319-21464-1. DOI: 10.1007/978-3-319-21464-1_35.

[8] M. Bachmann, A. Gumenyuk and M. Rethmeier. Welding with High-power Lasers: Trends and Developments. *Physics Procedia* 83 (2016), 15–25. DOI: 10.1016/j.phpro.2016.08.003.

[9] M.-F. Huang, H.-C. Lee, J.-K. Ho, H.-C. Lin, C.-S. Cheng, C.-C. Kuo and Y.-K. Kuo. Laser diode for DVD pickup head. *Optoelectronic Materials and*

*Devices*. Ed. by M. Osinski and Y.-K. Su. Vol. 3419. International Society for Optics and Photonics. SPIE, 1998. DOI: 10.1117/12.310997.

[10] M. Ikeda and S. Uchida. Blue–Violet Laser Diodes Suitable for Blu-ray Disk. *physica status solidi (a)* 194.2 (2002), 407–413. DOI: 10.1002/1521-396X(200212)194:2<407::AID-PSSA407>3.0.CO;2-N.

[11] M. P. Minitti, J. M. Budarz, A. Kirrander, J. S. Robinson, D. Ratner, T. J. Lane, D. Zhu, J. M. Glownia, M. Kozina, H. T. Lemke, M. Sikorski, Y. Feng, S. Nelson, K. Saita, B. Stankus, T. Northey, J. B. Hastings and P. M. Weber. Imaging Molecular Motion: Femtosecond X-Ray Scattering of an Electrocyclic Chemical Reaction. *Physical Review Letters* 114 (25 2015), 255501. DOI: 10.1103/PhysRevLett.114.255501.

[12] M. A. Wulder, J. C. White, R. F. Nelson, E. Næsset, H. O. Ørka, N. C. Coops, T. Hilker, C. W. Bater and T. Gobakken. Lidar sampling for large-area forest characterization: A review. *Remote Sensing of Environment* 121 (2012), 196–209. ISSN: 0034-4257. DOI: 10.1016/j.rse.2012.02.001.

[13] J. H. Churnside. Review of profiling oceanographic lidar. *Optical Engineering* 53.5 (2013), 1–13. DOI: 10.1117/1.OE.53.5.051405.

[14] K. Sassen. The Polarization Lidar Technique for Cloud Research: A Review and Current Assessment. *Bulletin of the American Meteorological Society* 72.12 (1991), 1848–1866. DOI: 10.1175/1520-0477(1991)072<1848:TPLTFC>2.0.CO;2.

[15] M. Jaboyedoff, T. Oppikofer, A. Abellán, M.-H. Derron, A. Loye, R. Metzger and A. Pedrazzini. Use of LIDAR in landslide investigations: a review. *Natural Hazards* 61 (2012), 5–28. DOI: 10.1007/s11069-010-9634-2.

[16] J. S. Deems, T. H. Painter and D. C. Finnegan. Lidar measurement of snow depth: a review. *Journal of Glaciology* 59.215 (2013), 467–479. DOI: 10.3189/2013JoG12J154.

[17] R. Wang. 3D building modeling using images and LiDAR: a review. *International Journal of Image and Data Fusion* 4.4 (2013), 273–292. DOI: 10.1080/19479832.2013.811124.

[18] M. Himmelsbach, A. Mueller, T. Lüttel and H.-J. Wünsche. LIDAR-based 3D object perception. *Proceedings of 1st international workshop on cognition for technical systems*. Vol. 1. 2008.

[19] G. Vosselman and H.-G. Maas. *Airborne and terrestrial laser scanning*. CRC press, 2010.

[20] C. Jamet, A. Ibrahim, Z. Ahmad, F. Angelini, M. Babin, M. J. Behrenfeld, E. Boss, B. Cairns, J. Churnside, J. Chowdhary, A. B. Davis, D. Dionisi, L. Duforêt-Gaurier, B. Franz, R. Frouin, M. Gao, D. Gray, O. Hasekamp, X. He, C. Hostetler, O. V. Kalashnikova, K. Knobelspiesse, L. Lacour, H. Loisel, V. Martins, E. Rehm, L. Remer, I. Sanhaj, K. Stamnes, S. Stamnes, S. Victori, J. Werdell and P.-W. Zhai. Going Beyond Standard Ocean Color Observations: Lidar and Polarimetry. *Frontiers in Marine Science* 6 (2019), 251. DOI: 10.3389/fmars.2019.00251.

[21] Apple Inc. *Apple unveils new iPad Pro with breakthrough LiDAR Scanner and brings trackpad support to iPadOS*. 2020. URL: https://www.apple.com/newsroom/2020/03/apple-unveils-new-ipad-pro-with-lidar-scanner-and-trackpad-support-in-ipados/ (Accessed: 4 June 2020).

[22] R. H. Rasshofer and K. Gresser. Automotive Radar and Lidar Systems for Next Generation Driver Assistance Functions. *Advances in Radio Science* 3 (2005). DOI: 10.5194/ars-3-205-2005.

[23] J. Kocić, N. Jovičić and V. Drndarević. Sensors and sensor fusion in autonomous vehicles. *2018 26th Telecommunications Forum (TELFOR)*. IEEE. 2018, 420–425. DOI: 10.1109/TELFOR.2018.8612054.

[24] P. A. Franken, A. E. Hill, C. W. Peters and G. Weinreich. Generation of optical harmonics. *Physical Review Letters* 7.4 (1961), 118. DOI: 10.1103/PhysRevLett.7.118.

[25] R. Boyd. *Nonlinear optics. 3rd Edition*. Academic press, 2008. ISBN: 978-0-08-048596-6.

[26] H. Yu, Z. Pan, H. Zhang and J. Wang. Recent advances in self-frequency-doubling crystals. *Journal of Materiomics* 2.1 (2016), 55–65. DOI: 10.1016/j.jmat.2015.12.001.

[27] R. Trebino. *Frequency-Resolved Optical Gating. The Measurement of Ultrashort Laser Pulses*. Springer, 2003, 101–115. DOI: 10.1007/978-1-4615-1181-6_5.

[28] P. F. Curley, A. I. Ferguson, J. G. White and W. B. Amos. Application of a femtosecond self-sustaining mode-locked Ti:sapphire laser to the field of laser scanning confocal microscopy. *Optical and Quantum Electronics* 24 (1992), 851–859. DOI: 10.1007/BF00620198.

[29] *IEC 60825-1:2014 - Safety of laser products - Part 1: Equipment classification and requirements*. Standard. International Electrotechnical Commission, 2014.

[30] B. Schwarz. Mapping the world in 3D. *Nature Photonics* 4 (2010), 429–430. DOI: 10.1038/nphoton.2010.148.

[31] S. Royo and M. Ballesta-Garcia. An Overview of Lidar Imaging Systems for Autonomous Vehicles. *Applied Sciences* 9.19 (2019), 4093. DOI: 10.3390/app9194093.

[32] A. Samman, L. Rimai, J. R. McBride, R. O. Carter, W. H. Weber, C. Gmachl, F. Capasso, A. L. Hutchinson, D. L. Sivco and A. Y. Cho. Potential use of near, mid and far infrared laser diodes in automotive LIDAR applications. *Vehicular Technology Conference Fall 2000. IEEE VTS Fall VTC2000. 52nd Vehicular Technology Conference (Cat. No.00CH37152)*. Vol. 5. IEEE, 2000. DOI: 10.1109/VETECF.2000.883239.

[33] European Center for Information and Communication Technologies. *DENSE - 24/7 automotive sensing system*. 2021. URL: https://www.dense247.eu/home/index.html (Accessed: 2 Feb. 2021).

[34] *Solar energy — Reference solar spectral irradiance at the ground at different receiving conditions — Part 1: Direct normal and hemispherical solar irradiance for air mass 1.5*. Standard. International Organization for Standardization, 1992.

[35] *Standard Tables for Reference Solar Spectral Irradiances: Direct Normal and Hemispherical on 37° Tilted Surface*. Standard. The American Society for Testing and Materials, 2012. DOI: 10.1520/G0173-03R12.

[36] G. M. Williams. Optimization of eyesafe avalanche photodiode lidar for automobile safety and autonomous navigation systems. *Optical Engineering* 56.3 (2017), 031224. DOI: 10.1117/1.OE.56.3.031224.

[37] Y. Zhang and X. Shen. Quantitative Analysis on Geometric Size of LiDAR Footprint. *IEEE Geoscience and Remote Sensing Letters* 11.3 (2014), 701–705. DOI: 10.1109/LGRS.2013.2276126.

[38] R. J. Mears, L. Reekie, I. M. Jauncey and D. N. Payne. Low-noise erbium-doped fibre amplifier operating at 1.54 μm. *Electronics Letters* 23.19 (1987), 1026–1028. DOI: 10.1049/el:19870719.

[39] B. Desthieux, R. Laming and D. Payne. 111 kW (0.5 mJ) pulse amplification at 1.5 μm using a gated cascade of three erbium-doped fiber amplifiers. *Applied physics letters* 63.5 (1993), 586–588. DOI: 10.1063/1.109957.

[40] V. V. Ter-Mikirtychev. *Fundamentals of Fiber Lasers and Fiber Amplifiers*. Ed. by H. K. V. Lotsch and W. T. Rhodes. Springer, 2019. Chap. Fiber Laser Physics Fundamentals, 89–90. ISBN: 978-3-030-33890-9.

[41] J.-M. Delavaux and J. Nagel. Multi-stage erbium-doped fiber amplifier designs. *Journal of lightwave technology* 13.5 (1995), 703–720. DOI: 10.1109/50.387788.

[42] V. V. Ter-Mikirtychev. *Fundamentals of Fiber Lasers and Fiber Amplifiers*. Ed. by H. K. V. Lotsch and W. T. Rhodes. Springer, 2019. Chap. Fiber Laser Physics Fundamentals, 87–88. ISBN: 978-3-030-33890-9.

[43] D. Jedrzejczyk, P. Asbahr, M. Pulka, B. Eppich and K. Paschke. High-Power Single-Mode Fiber Coupling of a Laterally Tapered Single-Frequency Diode Laser. *IEEE Photonics Technology Letters* 26.8 (2014), 845–847. DOI: 10.1109/LPT.2014.2309177.

[44] T. J. Van Den Berg and H. Spekreijse. Near infrared light absorption in the human eye media. *Vision Research* 37.2 (1997), 249–253. DOI: 10.1016/S0042-6989(96)00120-4.

[45] S. Nakamura, T. Mukai and M. Senoh. Candela-class high-brightness InGaN/AlGaN double-heterostructure blue-light-emitting diodes. *Applied Physics Letters* 64 (13 1994), 1687–1689. DOI: 10.1063/1.111832@apl.2019.APLCLASS2019.issue-1.

[46] S. Nakamura. InGaN-based blue laser diodes. *IEEE Journal of Selected Topics in Quantum Electronics* 3.3 (1997), 712–718. DOI: 10.1109/2944.640626.

[47] Nobel Media AB. *The Nobel Prize in Physics 2014 - Press Release*. 2014. URL: https://www.nobelprize.org/prizes/physics/2014/press-release/ (Accessed: 17 June 2020).

[48] T. Tanaka, K. Uchida, Y. Ishitani and S. Minagawa. Lasing operation up to 200 K in the wavelength range of 570–590 nm by GaInP/AlGaInP double-heterostructure laser diodes on GaAsP substrates. *Applied Physics Letters* 66.7 (1995), 783–785. DOI: 10.1063/1.114187.

[49] R. Bohdan, A. Bercha, W. Trzeciakowski, F. Dybała, B. Piechal, M. B. Sanayeh, M. Reufer and P. Brick. Yellow AlGaInP/InGaP laser diodes achieved by pressure and temperature tuning. *Journal of Applied Physics* 104.6 (2008), 063105. DOI: 10.1063/1.2978359.

[50] L. Toikkanen, A. Härkönen, J. Lyytikäinen, T. Leinonen, A. Laakso, A. Tukiainen, J. Viheriälä, M. Bister and M. Guina. Optically Pumped Edge-Emitting GaAs-Based Laser With Direct Orange Emission. *IEEE Photonics Technology Letters* 26.4 (2014), 384–386. DOI: 10.1109/LPT.2013.2294726.

[51] O. T. Tan, J. M. Carney, R. Margolis, Y. Seki, J. Boll, R. R. Anderson and J. A. Parrish. Histologic responses of port-wine stains treated by argon, carbon dioxide, and tunable dye lasers: a preliminary report. *Archives of Dermatology* 122.9 (1986), 1016–1022. DOI: 10.1001/archderm.1986.01660210066020.

[52] M. Mainster. Continuous-wave and micropulse 577 nm yellow–orange laser photocoagulation: a laser for all reasons. *Retina Today* (2010), 1–8. URL: http://retinatoday.com/2010/04/insert2/continuous-wave-and-micropulse-577-nm-yellow-laser-photocoagulation-a-laser-for-all-reasons/ (Accessed: 18 June 2020).

[53] N. Farahani, M. J. Schibler and L. A. Bentolila. Stimulated emission depletion (STED) microscopy: from theory to practice. *Microscopy: Science, Technology, Applications and Education*. Ed. by A. Méndez-Vilas and J. Díaz. Vol. 3. Formatex Research Center Badajoz, 2010, 1539–1547. ISBN: 978-84-614-6191-2.

[54] E. Kantola, T. Leinonen, S. Ranta, M. Tavast and M. Guina. High-efficiency 20 W yellow VECSEL. *Optics express* 22.6 (2014), 6372–6380. DOI: 10.1364/OE.22.006372.

[55] R. Paschotta. *Field Guide to Lasers*. SPIE Press, 2008. ISBN: 9780819478269.

[56] G. D. Boyd and D. A. Kleinman. Parametric Interaction of Focused Gaussian Light Beams. *Journal of Applied Physics* 39.8 (1968), 3597–3639. DOI: 10.1063/1.1656831.

[57] M. M. Fejer, G. Magel, D. H. Jundt and R. L. Byer. Quasi-phase-matched second harmonic generation: tuning and tolerances. *IEEE Journal of Quantum Electronics* 28.11 (1992), 2631–2654. DOI: 10.1109/3.161322.

[58] J. Alda. Laser and Gaussian Beam Propagation and Transformation. *Encyclopedia of Optical and Photonic Engineering, 2nd Edition*. Ed. by C. Hoffman and R. Driggers. CRC Press, 2015, 999–1013. ISBN: 9781351247184.

[59] P. D. Maker, R. W. Terhune, M. Nisenoff and C. M. Savage. Effects of dispersion and focusing on the production of optical harmonics. *Physical review letters* 8.1 (1962), 21–23. DOI: 10.1103/PhysRevLett.8.21.

[60] M. Houe and P. D. Townsend. An introduction to methods of periodic poling for second-harmonic generation. *Journal of Physics D: Applied Physics* 28.9 (1995), 1747. DOI: 10.1088/0022-3727/28/9/001.

[61] O. Gayer, Z. Sacks, E. Galun and A. Arie. Temperature and wavelength dependent refractive index equations for MgO-doped congruent and stoichiometric LiNbO3. *Applied Physics B* 91.2 (2008), 343–348. DOI: 10.1007/s00340-008-2998-2.

[62] VECSEL-based 590-nm laser system with 8 W of output power for the treatment of vascular lesions. *IEEE Journal of Selected Topics in Quantum Electronics* 25.1 (2018), 7202108. DOI: 10.1109/JSTQE.2018.2873493.

[63] Polarization dependence of quasi-phase-matched second-harmonic generation in bulk periodically poled LiNbO3. *Journal of Optics A: Pure and Applied Optics* 4.3 (2002), 324–328. DOI: 10.1088/1464-4258/4/3/319.

[64] N. E. Yu, J. H. Ro, M. Cha, S. Kurimura and T. Taira. Broadband quasi-phase-matched second-harmonic generation in MgO-doped periodically poled LiNbO3 at the communications band. *Optics Letters* 27.12 (2002), 1046–1048. DOI: 10.1364/OL.27.001046. URL: http://ol.osa.org/abstract.cfm?URI=ol-27-12-1046.

[65] O. B. Jensen, P. E. Andersen, B. Sumpf, K.-H. Hasler, G. Erbert and P. M. Petersen. 1.5 W green light generation by single-pass second harmonic generation of a single-frequency tapered diode laser. *Optics Express* 17.8 (2009), 6532–6539. DOI: 10.1364/OE.17.006532.

[66] A. K. Hansen, M. Tawfieq, O. B. Jensen, P. E. Andersen, B. Sumpf, G. Erbert and P. M. Petersen. Concept for power scaling second harmonic generation using a cascade of nonlinear crystals. *Optics Express* 23.12 (2015), 15921–15934. DOI: 10.1364/OE.23.015921.

[67] D. Jedrzejczyk, R. Güther, K. Paschke, W.-J. Jeong, H.-Y. Lee and G. Erbert. Efficient high-power frequency doubling of distributed Bragg reflector tapered laser radiation in a periodically poled MgO-doped lithium niobate planar waveguide. *Optics Letters* 36.3 (2011), 367–369. DOI: 10.1364/OL.36.000367.

[68] R. Bege, D. Jedrzejczyk, G. Blume, J. Hofmann, D. Feise, K. Paschke and G. Tränkle. Watt-level second-harmonic generation at 589 nm with a PPMgO:LN ridge waveguide crystal pumped by a DBR tapered diode laser. *Optics Letters* 41.7 (2016), 1530–1533. DOI: 10.1364/OL.41.001530.

[69] D. Feise, F. Bugge, M. Matalla, A. Thies, P. Ressel, G. Blume, J. Hofmann and K. Paschke. Distributed Bragg reflector tapered diode lasers emitting more than 10 W at 1154 nm. *High-Power Diode Laser Technology XVI*. Ed. by M. S. Zediker. Vol. 10514. International Society for Optics and Photonics. SPIE, 2018, 188–195. DOI: 10.1117/12.2290658.

[70] K. Paschke, F. Bugge, G. Blume, D. Feise and G. Erbert. High-power diode lasers at 1178 nm with high beam quality and narrow spectra. *Opt. Lett.* 40.1 (2015), 100–102. DOI: 10.1364/OL.40.000100.

[71] A. Mathur, M. Fisher, M. Ziari, M. Hagberg and E. Kolev. Very high power 1.48 μm semiconductor lasers. *Electronics Letters* 35 (12 1999), 983–985(2). DOI: 10.1049/el:19990665.

[72] J. P. Donnelly, J. N. Walpole, S. H. Groves, R. J. Bailey, L. J. Missaggia, A. Napoleone, R. E. Reeder and C. C. Cook. 1.5-μm tapered-gain-region lasers with high-CW output powers. *IEEE Photonics Technology Letters* 10.10 (1998), 1377–1379. DOI: 10.1109/68.720266.

[73] TOPTICA eagleyard. *Multimode laser diodes - High brightness broad area laser*. 2021. URL: https://www.toptica-eagleyard.com/products/multimode-laser-diodes/ (Accessed: 2 Feb. 2021).

[74] Innolume GmbH. *Products - Broad-area Laser Diodes*. 2021. URL: https://innolume.com/products/BA_HPLD.htm (Accessed: 2 Feb. 2021).

[75] D. Garbuzov, L. Xu, S. Forrest, R. Menna, R. Martinelli and J. Connolly. 1.5 μm wavelength, SCH-MQW InGaAsP/InP broadened-waveguide laser diodes with low internal loss and high output power. *Electronics Letters* 32 (18 1996), 1717–1719(2). DOI: 10.1049/el:19961098.

[76] Freedom Photonics LLC. *15xx nm High Power Diode Laser — FP3915*. 2021. URL: https://freedomphotonics.com/freedom-photonics-products/lasers-and-laser-sources/15xx-nm-high-power-diode-laser-fp3915/ (Accessed: 2 Feb. 2021).

[77] Seminex corporation. *C-Mount with Seminex laser diode*. 2021. URL: https://seminex.com/product/c-mount-with-seminex-laser-diode-31/ (Accessed: 2 Feb. 2021).

[78] A. T. Aho. *Optimization of semiconductor optical amplifier length for minimum power consumption*. Tampere University of Technology. M.Sc. thesis. 2016.

[79] L. A. Coldren, S. W. Corzine and M. L. Mashanovitch. *Diode Lasers and Photonic Integrated Circuits*. Wiley, 2012. Chap. A phenomenological approach to diode lasers, 59. ISBN: 9780470484128.

[80] L. A. Coldren, S. W. Corzine and M. L. Mashanovitch. *Diode Lasers and Photonic Integrated Circuits*. Wiley, 2012. Chap. Dynamic effects, 292. ISBN: 9780470484128.

[81] A. L. Schawlow and C. H. Townes. Infrared and Optical Masers. *Physical Review* 112 (6 1958), 1940–1949. DOI: 10.1103/PhysRev.112.1940.

[82] optique-ingenieur.org. *Hermite-Gaussian modes*. Public domain dedication (CC0). URL: http://www.optique-ingenieur.org/en/courses/OPI_ang_M01_C03/co/Contenu_13.html (Accessed: 8 July 2020).

[83] L. A. Coldren, S. W. Corzine and M. L. Mashanovitch. *Diode Lasers and Photonic Integrated Circuits*. Wiley, 2012. Chap. Mirrors and resonators for diode lasers, 141. ISBN: 9780470484128.

[84] L. A. Coldren, S. W. Corzine and M. L. Mashanovitch. *Diode Lasers and Photonic Integrated Circuits*. Wiley, 2012. Chap. Mirrors and resonators for diode lasers, 123. ISBN: 9780470484128.

[85] L. A. Coldren, S. W. Corzine and M. L. Mashanovitch. *Diode Lasers and Photonic Integrated Circuits*. Wiley, 2012. Chap. Perturbation, coupled mode theory and applications, 344. ISBN: 9780470484128.

[86] L. A. Coldren, S. W. Corzine and M. L. Mashanovitch. *Diode Lasers and Photonic Integrated Circuits*. Wiley, 2012. Chap. Mirrors and resonators for diode lasers, 121. ISBN: 9780470484128.

[87] L. A. Coldren, S. W. Corzine and M. L. Mashanovitch. *Diode Lasers and Photonic Integrated Circuits*. Wiley, 2012. Chap. Mirrors and resonators for diode lasers, 119. ISBN: 9780470484128.

[88] W. Streifer, D. Scifres and R. D. Burnham. Coupled wave analysis of DFB and DBR lasers. *IEEE Journal of Quantum Electronics* 13.4 (1977), 134–141. DOI: 10.1109/JQE.1977.1069328.

[89] H. Wenzel, R. Guther, A. M. Shams-Zadeh-Amiri and P. Bienstman. A comparative study of higher order Bragg gratings: coupled-mode theory versus mode expansion modeling. *IEEE Journal of Quantum Electronics* 42.1 (2006), 64–70. DOI: 10.1109/JQE.2005.859910.

[90] H. Wenzel, J. Fricke, J. Decker, P. Crump and G. Erbert. High-Power Distributed Feedback Lasers With Surface Gratings: Theory and Experiment. *IEEE Journal of Selected Topics in Quantum Electronics* 21.6 (2015), 352–358. DOI: 10.1109/JSTQE.2015.2429892.

[91] T. Uusitalo, H. Virtanen and M. Dumitrescu. Transverse structure optimization of distributed feedback and distributed Bragg reflector lasers with surface gratings. *Optical and quantum electronics* 49.6 (2017), 206. DOI: 10.1007/s11082-017-1039-y.

[92] W. Streifer, D. Scifres and R. Burnham. Coupling coefficients for distributed feedback single- and double-heterostructure diode lasers. *IEEE Journal of Quantum Electronics* 11.11 (1975), 867–873. DOI: 10.1109/JQE.1975.1068539.

[93] L. A. Coldren, S. W. Corzine and M. L. Mashanovitch. *Diode Lasers and Photonic Integrated Circuits*. Wiley, 2012. Chap. Mirrors and resonators for diode lasers, 140. ISBN: 9780470484128.

[94] L. A. Coldren, S. W. Corzine and M. L. Mashanovitch. *Diode Lasers and Photonic Integrated Circuits*. Wiley, 2012. Chap. Mirrors and resonators for diode lasers, 125. ISBN: 9780470484128.

[95] S. Spießberger, M. Schiemangk, A. Wicht, H. Wenzel and G. Erbert. DBR laser diodes emitting near 1064 nm with a narrow intrinsic linewidth of 2 kHz. *Applied Physics B* 104.4 (2015), 813. DOI: 10.1007/s00340-011-4644-7.

[96] S. N. Kaunga-Nyirenda, S. Bull, J. J. Lim, K.-H. Hasler, J. Fricke and E. C. Larkins. Factors influencing brightness and beam quality of conventional and distributed Bragg reflector tapered laser diodes in absence of self-heating. *IET Optoelectronics* 8.2 (2014), 99–107. DOI: 10.1049/iet-opt.2013.0082.

[97] P. Bienstman. Rigorous and efficient modelling of wavelenght scale photonic components. PhD thesis. Ghent University, 2001. URL: https://www.photonics.intec.ugent.be/publications/phd.asp?ID=104.

[98] J. Piprek and Z. Li. What Causes the Pulse Power Saturation of GaAs-Based Broad-Area Lasers?: *IEEE Photonics Technology Letters* 30.10 (2018), 963–966. DOI: 10.1109/LPT.2018.2826979.

[99] D. Mehuys, S. O'Brien, R. J. Lang, A. Hardy and D. F. Welch. 5W, diffraction-limited, tapered-stripe unstable resonator semiconductor laser. *Electronics Letters* 30.22 (1994), 1855–1856. DOI: 10.1049/el:19941272.

[100] M. T. Kelemen, J. Weber, S. Kallenbach, C. Pfahler, M. Mikulla and G. Weimann. Astigmatism and beam quality of high-brightness tapered diode lasers. *Semiconductor Lasers and Laser Dynamics*. Ed. by D. Lenstra, G. Morthier, T. Erneux and M. Pessa. Vol. 5452. International Society for Optics and Photonics. SPIE, 2004, 233–243. DOI: 10.1117/12.545221.

[101] M. Mikulla, P. Chazan, A. Schmitt, S. Morgott, A. Wetzel, M. Walther, R. Kiefer, W. Pletschen, J. Braunstein and G. Weimann. High-brightness tapered semiconductor laser oscillators and amplifiers with low-modal gain epilayer-structures. *IEEE Photonics Technology Letters* 10.5 (1998), 654–656. DOI: 10.1109/68.669231.

[102] P. Albrodt. Coherent beam combining of high-brightness tapered semiconductor optical amplifiers. PhD thesis. Jan. 2020.

[103] M. Uebernickel, B. Eppich, K. Paschke, G. Erbert and G. Trankle. Prediction of Single-Mode Fiber Coupling Efficiencies of a Tapered Diode Laser From Measured Wigner Distribution Functions. *IEEE Photonics Technology Letters* 24.14 (2012), 1248–1250. DOI: 10.1109/LPT.2012.2199746.

[104] M. Uebernickel, G. Blume, C. Fiebig, C. Kaspari, D. Feise, K. Paschke, A. Ginolas, R. Güther, B. Eppich and G. Erbert. Beam quality dependent SHG using edge-emitting lasers and a 50 mm bulk PPLN crystal. *Nonlinear Frequency Generation and Conversion: Materials, Devices, and Applications VIII*. Vol. 7197. International Society for Optics and Photonics. 2009, 71970F. DOI: 10.1117/12.807429.

[105] A. Jechow, R. Menzel, K. Paschke and G. Erbert. Blue-green light generation using high brilliance edge emitting diode lasers. *Laser & Photonics Reviews* 4.5 (2010), 633–655. DOI: 10.1002/lpor.200900023.

[106] All About Circuits. *Kelvin (4-wire) Resistance Measurement*. URL: https://www.allaboutcircuits.com/textbook/direct-current/chpt-8/kelvin-resistance-measurement/ (Accessed: 14 Apr. 2021).

[107] *ISO 11146-1:2005 - Lasers and laser-related equipment — Test methods for laser beam widths, divergence angles and beam propagation ratios — Part 1: Stigmatic and simple astigmatic beams*. Standard. International Organization for Standardization, 2005.

[108] *ISO 11146-2:2005 - Lasers and laser-related equipment — Test methods for laser beam widths, divergence angles and beam propagation ratios — Part 2: General astigmatic beams*. Standard. International Organization for Standardization, 2005.

[109] *ISO 11146-3:2005 - Lasers and laser-related equipment — Test methods for laser beam widths, divergence angles and beam propagation ratios — Part 3: Intrinsic and geometrical laser beam classification, propagation and details of test methods*. Standard. International Organization for Standardization, 2005.

[110] S. Kawashima, M. Imada, K. Ishizaki and S. Noda. High-Precision Alignment and Bonding System for the Fabrication of 3-D Nanostructures. *Journal of Microelectromechanical Systems* 16.5 (2007), 1140–1144. DOI: 10.1109/JMEMS.2007.904950.

[111] M. C. King and D. H. Berry. Photolithographic Mask Alignment Using Moiré Techniques. *Applied Optics* 11.11 (1972), 2455–2459. DOI: 10.1364/AO.11.002455.

[112] M. Ritala and M. Leskelä. Chapter 2 - Atomic layer deposition. *Handbook of Thin Films*. Ed. by H. Singh Nalwa. Academic Press, 2002, 103–159. ISBN: 978-0-12-512908-4. DOI: https://doi.org/10.1016/B978-012512908-4/50005-9.

[113] H. Virtanen, A. T. Aho, J. Viheriälä, V. Korpijärvi, T. Uusitalo, M. Koskinen, M. Dumitrescu and M. Guina. Spectral Characteristics of Narrow-Linewidth High-Power 1180 nm DBR Laser With Surface Gratings. *IEEE Photonics Technology Letters* 29.1 (2017), 114–117. DOI: 10.1109/LPT.2016.2629512.

[114] S.-P. Ojanen. *Brightness Analysis of High-Power Edge-Emitting Lasers*. Tampere University of Technology. M.Sc. thesis. 2018.

[115] P. Crump, G. Erbert, H. Wenzel, C. Frevert, C. M. Schultz, K. H. Hasler, R. Staske, B. Sumpf, A. Maaßdorf, F. Bugge and et al. Efficient High-Power Laser Diodes. *IEEE Journal of Selected Topics in Quantum Electronics* 19.4 (2013), 1501211–1501211. ISSN: 1077-260X. DOI: 10.1109/JSTQE.2013.2239961.

[116] S. N. Kaunga-Nyirenda, S. Bull, J. J. Lim, K.-H. Hasler, J. Fricke and E. C. Larkins. Factors influencing brightness and beam quality of conventional and distributed Bragg reflector tapered laser diodes in absence of self-heating. *IET Optoelectronics* 8.2 (2014), 99–107. DOI: 10.1049/iet-opt.2013.0082.

[117] L. Hallman, B. S. Ryvkin, E. A. Avrutin, A. T. Aho, J. Viheriälä, M. Guina and J. T. Kostamovaara. Double asymmetric structure 1.5 μm high power laser diodes. *2019 IEEE High Power Diode Lasers and Systems Conference (HPD)*. IEEE. 2019, 19–20. DOI: 10.1109/HPD48113.2019.8938671.

[118] L. W. Hallman, B. S. Ryvkin, E. A. Avrutin, A. T. Aho, J. Viheriälä, M. Guina and J. T. Kostamovaara. High Power 1.5$\mu$ m Pulsed Laser Diode With Asymmetric Waveguide and Active Layer Near p-cladding. *IEEE Photonics Technology Letters* 31.20 (2019), 1635–1638. DOI: 10.1109/LPT.2019.2940231.

[119] A. Aho, J. Viheriälä, H. Virtanen, T. Uusitalo, M. Koskinen, J. Reuna and M. Guina. High peak power laser diodes at 1.5 um with integrated wavelength locking element (Conference Presentation). *High-Power Diode Laser Technology XVIII*. Ed. by M. S. Zediker. Vol. 11262. International Society for Optics and Photonics. SPIE, 2020. DOI: 10.1117/12.2542095.

# PUBLICATIONS

# PUBLICATION

# I

**High-Power 1180-nm GaInNAs DBR Laser Diodes**

A. T. Aho, J. Viheriälä, V.-M. Korpijärvi, M. Koskinen, H. Virtanen,
M. Christensen, T. Uusitalo, K. Lahtonen, M. Valden and M. Guina

*IEEE Photonics Technology Letters* 29.23 (2017), 2023–2026
DOI: 10.1109/LPT.2017.2760038

# High-Power 1180-nm GaInNAs DBR Laser Diodes

Antti T. Aho, Jukka Viheriälä, Ville-Markus Korpijärvi, Mervi Koskinen, Heikki Virtanen, Mathias Christensen, Topi Uusitalo, Kimmo Lahtonen, Mika Valden, and Mircea Guina

***Abstract*— We report high-power 1180-nm GaInNAs distributed Bragg reflector laser diodes with and without a tapered amplifying section. The untapered and tapered components reached room temperature output powers of 655 mW and 4.04 W, respectively. The diodes exhibited narrow linewidth emission with side-mode suppression ratios in the range of 50 dB for a broad range of operating current, extending up to 2 A for the untapered component and 10 A for the tapered component. The high output power is rendered possible by the use of a high quality GaInNAs-based quantum well gain region, which allows for lower strain and better carrier confinement compared with traditional GaInAs quantum wells. The development opens new opportunities for the power scaling of frequency-doubled lasers with emission at yellow–orange wavelengths.**

***Index Terms*— High power, distributed Bragg reflector lasers, frequency doubling, antireflection coatings.**

## I. Introduction

LASERS emitting in the yellow–orange spectral range have many applications for example in dermatology [1], DNA sequencing [2], and spectroscopy [3]. However, this wavelength range cannot be reached directly with semiconductor lasers, which are the most practical and compact laser solutions whenever available. One viable approach for reaching the visible spectral range is frequency doubling from infrared (IR) laser radiation, which in turn, requires sources with high output power and narrow linewidth emission [4]. The frequency doubling scheme and the development of corresponding diodes with infrared emission has been vigorously addressed for blue–green spectral ranges where mature GaInAs quantum well (QW) gain materials can be used [4]. Several watts of green frequency-doubled radiation have been obtained using 1064 nm laser diodes [5]. However, the results for yellow frequency-doubled diodes have been more modest. This is largely due to the fact that it becomes increasingly difficult to reach high power close to 1.2 $\mu$m when using the standard materials. For example, using GaInAs QWs the maximum single-mode power obtained from untapered LDs at 1180 nm is about 230 mW [6] and about 3.2 W for tapered LDs [7]. Using quantum dots with an untapered design, a power of 80 mW has been reported [8]. As an alternative solution to achieve narrow linewidth emission in this wavelength range we have developed GaInNAs QWs and recently demonstrated an untapered distributed Bragg reflector laser diode (DBR-LD) emitting about 500 mW at 1180 nm and exhibiting a linewidth below 250 kHz over the entire operation range [9]. The addition of a small amount of nitrogen makes it possible to extend the wavelength range of the regular GaInAs QW and at the same time reduce the strain linked to In incorporation. Moreover, it also improves the carrier confinement resulting in improved temperature stability; in fact, we demonstrated a variation of the output power of only 30% for a temperature range extending from 20 °C to 80 °C [10].

In this letter we report further power scaling of the untapered 1180 nm DBR-LD with an output power as high as 655 mW at room temperature. Furthermore, by implementing a tapered design we demonstrate a room temperature output power of 4.04 W.

## II. Laser Structure and Fabrication

The semiconductor structure was grown by plasma-assisted molecular beam epitaxy (MBE). The substrate was n-GaAs(100) and the active region comprised a single $Ga_{0.67}In_{0.33}N_{0.005}As$ QW. The QW was surrounded by a GaAs waveguide and $Al_{0.25}Ga_{0.75}As$ claddings. The semiconductor layers and the band gap structure are depicted in Fig. 1.

Compared to the previously reported structure [10], the In content of the QW was increased to shift the material gain to a longer wavelength, closer to the mode supported by the DBR grating. The photoluminescence wavelength of the wafer at room temperature was 1151 nm.

For the untapered design, the processed waveguide comprised a passive (unbiased), third-order DBR grating section with a length of 1.8 mm and an active ridge waveguide (RWG) section with a length of 2.9 mm. The DBR section selects a single longitudinal mode and the RWG section defines a single transversal mode. The width of both the DBR and the RWG was 3.2 $\mu$m.

Manuscript received August 28, 2017; revised September 21, 2017; accepted October 2, 2017. Date of publication October 6, 2017; date of current version October 30, 2017. This work was supported in part by the Academy of Finland under Grant 141481, in part by the FP7 Project RAPIDO under Grant 619806, in part by the H2020-ECSEL-2015 Project DENSE, in part by the HPY Research Foundation, in part by the Finnish Foundation for Technology Promotion, and in part by the KAUTE Foundation. *(Corresponding author: Antti T. Aho.)*

A. T. Aho, J. Viheriälä, M. Koskinen, H. Virtanen, T. Uusitalo, K. Lahtonen, M. Valden, and M. Guina are with the Optoelectronic Research Centre, Tampere University of Technology, 33101 Tampere, Finland (e-mail: antti.t.aho@tut.fi; jukka.viheriala@tut.fi; mervi.koskinen@tut.fi; heikki.a.virtanen@tut.fi; topi.uusitalo@tut.fi; kimmo.lahtonen@tut.fi; mika.valden@tut.fi; mircea.guina@tut.fi).

V.-M. Korpijärvi was with the Optoelectronic Research Centre, Tampere University of Technology, 33101 Tampere, Finland. He is now with Okmetic Oyj, 01301 Vantaa, Finland (e-mail: ville.korpijarvi@hotmail.com).

M. Christensen is with Norlase ApS, DK-4000 Roskilde, Denmark, and also with the Department of Photonics Engineering, Technical University of Denmark, DK-4000 Roskilde, Denmark (e-mail: mac@norlase.com).

Color versions of one or more of the figures in this letter are available online at http://ieeexplore.ieee.org.

Digital Object Identifier 10.1109/LPT.2017.2760038

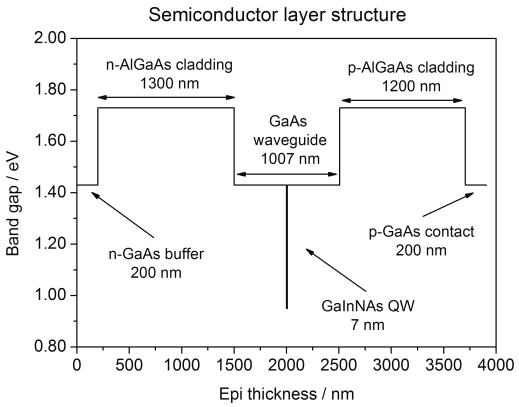


Fig. 1. Semiconductor layer structure revealing the band gap profile.

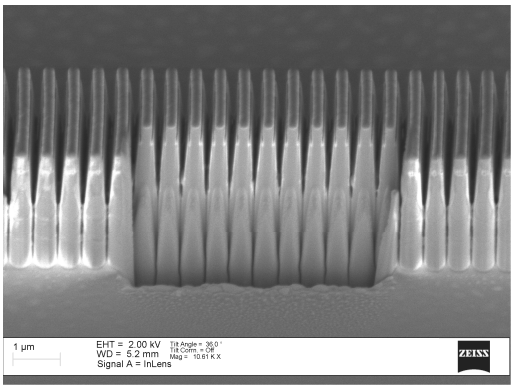


Fig. 2. Scanning electron microscope picture of the grating side profile. Focused ion beam (FIB) has been used to cut into the grating in order to better see the cross-section in the middle.

The grating and the ridge were fabricated without regrowth, using low-cost and high-throughput soft-stamp ultraviolet nanoimprint lithography [11]. The basic fabrication steps of the gratings have been presented in [10]. In this work, the side profile of the grating was tuned by adjusting the etching recipe in order to reach a grating filling factor of approximately 0.85 leading to a higher reflection coefficient and lower radiative losses [12]. The etching was performed using $Cl_2/N_2$-based inductively coupled plasma reactive ion etching (ICP-RIE). The etching depths of the grating and the RWG were 1200 nm and 1350 nm, respectively. The achieved grating side profile can be seen in Fig. 2.

The design of the tapered DBR-LD comprises a 2 mm long passive DBR section, a 1 mm long active RWG section and a 4 mm long gain-guided tapered amplifying section with a tapering angle of 5°. The DBR and RWG widths were 3.2 $\mu$m, and the DBR and RWG etching depths were 1500 nm and 1350 nm, respectively.

The components were packaged by first soldering the chips p-side down on ceramic AlN submounts with AuSn solder and

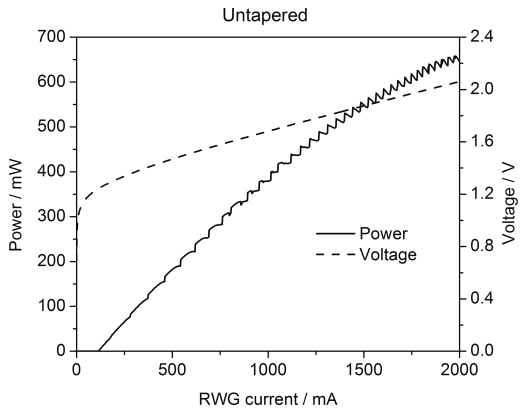


Fig. 3. The output power and voltage of the untapered LD from 0 mA to 2000 mA at 20 °C.

then bonding the submounts on gold plated copper heatsinks with indium solder. The chips were antireflection (AR) coated to suppress unwanted Fabry-Perot operation and to improve the outcoupling from the front facet. Traditionally thin-film AR coatings have been prepared by methods such as electron beam and thermal evaporation, ion assisted deposition, ion beam sputtering, or magnetron sputtering. In the work presented here, atomic layer deposition (ALD) was used as an alternative method to fabricate the AR coatings on laser facets. A two-layer $Al_2O_3$ (128.7 nm)/$TiO_2$ (77.6 nm) AR design was fabricated on the untapered component and a single-layer $Al_2O_3$ (146.8 nm) design on the tapered component using Picosun Sunale ALD R200 Advanced reactor. The two-layer and single-layer coatings were grown at substrate temperatures of 100 °C and 200 °C, respectively. Trimethylaluminium, tetrakis-(dimethylamino)titanium, and deionized water were used as precursors. At 100 °C, refractive indices of 1.595 and 2.401 were determined for $Al_2O_3$ and $TiO_2$ layers, respectively. The refractive index of $Al_2O_3$ grown at 200 °C was determined to be 1.665. The performance of the AR coatings was assessed using reference substrates and reflectance spectroscopy with Perkin Elmer Lambda 1050 UV/Vis/NIR Spectrophotometer. The ALD growth processes yielded an $Al_2O_3/TiO_2$ two-layer thin film and an $Al_2O_3$ single-layer thin film with reflectances below 1% and approximately 3% at 1180 nm, respectively.

## III. Results

The CW ILV (current, power, voltage) characteristics of an untapered and tapered DBR-LD at 20 °C mount temperature are shown in Fig. 3 and Fig. 4, respectively. The untapered component was measured up to a current of 2 A and the tapered component up to a taper current ($I_{TA}$) of 10 A with a constant 350 mA RWG injection current ($I_{RWG}$). The kinks in the untapered component output power are related to the lasing longitudinal mode changing to match the maximum DBR reflectivity, when the temperature of the active

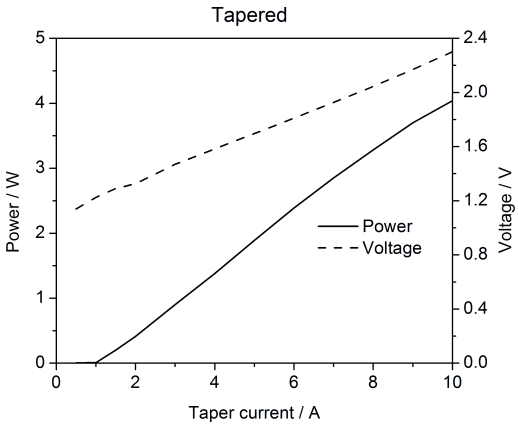


Fig. 4. The output power and voltage of a tapered LD from 0 A to 10 A tapered section current at 20 °C. The RWG section current was held at constant 350 mA.

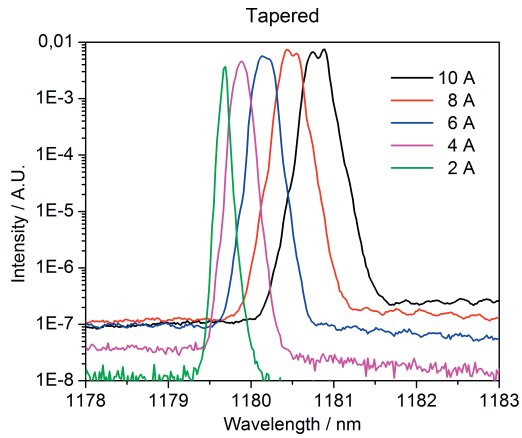


Fig. 6. Spectra from the tapered component at 20 °C mount temperature with various $I_{TA}$ while $I_{RWG}$ was constant 350 mA. The spectral resolution is 0.05 nm.

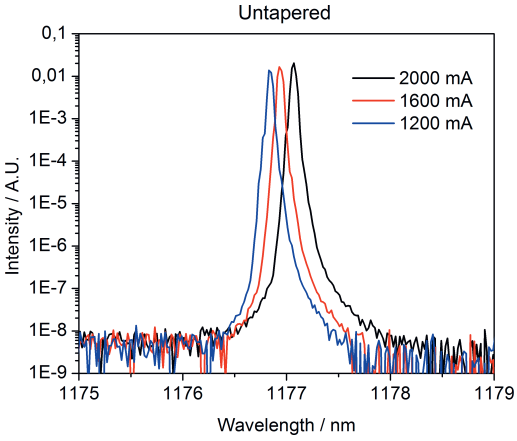


Fig. 5. Spectra from the untapered component at 20 °C mount temperature with various injection currents. The spectral resolution is 0.05 nm.

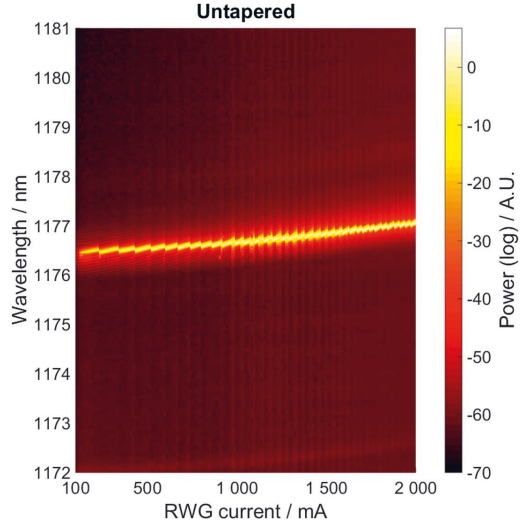


Fig. 7. Spectra of the untapered component from 100 mA to 2000 mA.

region increases [13]. At 20 °C the untapered and tapered components reached output powers of about 655 mW and 4.04 W, respectively (limited by the current range used for the measurements). We note that the power curve for the tapered LD does not show significant signs of roll-off at the maximum current available for the measurement.

The emission wavelength of the components could be tuned by changing the mount temperature or the injection current. The tuning rates for the untapered and tapered components were about 90 pm/°C for temperature and about 0.30 pm/mA and 0.14 pm/mA for current, respectively. The emission spectra with various injection currents are shown in Fig. 5 and Fig. 6. The mode hops between adjacent DBR modes and the shift in the emission wavelength with increasing current can be seen in Fig. 7 and Fig. 8. The temperature stability of the components was good: the untapered and tapered components reached output powers of over 400 mW and over 1500 mW at 60 °C, respectively.

The spectrum full width at half maximum (FWHM) at 20 °C mount temperature was 50 pm for the untapered component with 2000 mA injection current and 270 pm for the tapered component with $I_{TA} = 10$ A, $I_{RWG} = 350$ mA. The spectral width of the untapered component was limited by the resolution of the used Anritsu MS9710C optical spectrum analyzer [14], but self-homodyne linewidth measurements from previous generation components with similar structure have yielded fitted Lorentzian FWHM below 250 kHz [9].

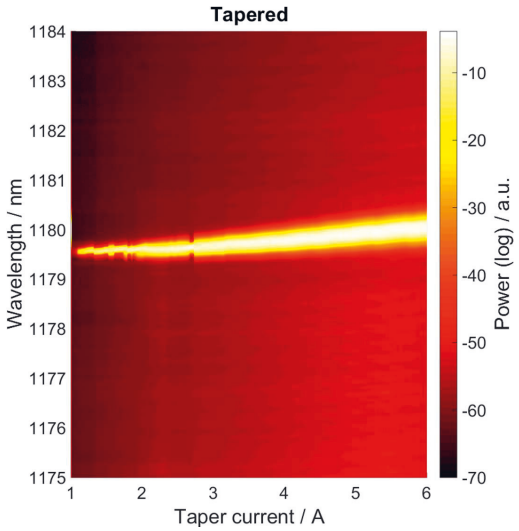


Fig. 8. Spectra of the tapered component from 1 A to 6 A with $I_{\mathrm{RWG}} = 350$ mA.

We expect that the FWHM of the tapered component can be significantly reduced by using an AR coating with a smaller reflectance. A preliminary test showed that, at a power level of 1.7 W, applying a two-layer $Al_2O_3/TiO_2$ AR coating to a tapered DBR (similar to the coating we applied to the untapered DBR) resulted in a spectral peak FWHM of 70 pm, which is close to the resolution limit of the spectrum analyzer, while the single-layer $Al_2O_3$ AR coating resulted in a FWHM of 220 pm.

The far-field (FF) fast axis and slow axis FWHM of the untapered component at 2000 mA injection current were $\sim 40°$ and $\sim 7°$, respectively. For the tapered component at 10 A injection current, the FF fast axis and slow axis FWHM were $\sim 40°$ and $\sim 6°$, respectively.

## IV. Conclusions

We reported the highest power to date for narrow-linewidth untapered DBR laser diodes emitting around 1180 nm and demonstrated for the first time GaInNAs tapered DBR laser diodes in this wavelength range. At room temperature the output power of the untapered and tapered DBR-LDs reached 655 mW and 4.04 W, respectively. The high output power is linked to the use of a GaInNAs-based QW structure which enables smaller strain and improved carrier confinement compared to traditional GaInAs material. The high output power and narrow linewidth make these kinds of components interesting for the development of frequency-doubled lasers with emission at yellow–orange wavelengths.

## References

[1] N. S. Sadick and R. Weiss, "The utilization of a new yellow light laser (578 nm) for the treatment of Class I red telangiectasia of the lower extremities," *Dermatolic Surg.*, vol. 28, no. 1, pp. 21–25, Jan. 2002.

[2] K. M. Murray, "DNA sequencing by mass spectrometry," *J. Mass Spectrometry*, vol. 31, no. 11, pp. 1203–1215, Nov. 1996.

[3] T. Nishikawa, A. Ozawa, Y. Nishida, M. Asobe, F. Hong, and T. W. Hänsch, "Efficient 494 mW sum-frequency generation of sodium resonance radiation at 589 nm by using a periodically poled Zn:$LiNbO_3$ ridge waveguide," *Opt. Exp.*, vol. 17, no. 20, pp. 17792–17800, 2009.

[4] A. Jechow, R. Menzel, K. Paschke, and G. Erbert, "Blue-green light generation using high brilliance edge emitting diode lasers," *Laser Photon. Rev.*, vol. 4, no. 5, pp. 633–655, Sep. 2010.

[5] A. K. Hansen *et al.*, "Concept for power scaling second harmonic generation using a cascade of nonlinear crystals," *Opt. Exp.*, vol. 23, no. 12, pp. 15921–15934, 2015.

[6] K. Paschke *et al.*, "Watt-level continuous-wave diode lasers at 1180 nm with InGaAs quantum wells," in *Proc. SPIE*, 2014, p. 896509. [Online]. Available: http://dx.doi.org/10.1117/12.2037752

[7] R. Bege *et al.*, "Watt-level second-harmonic generation at 589 nm with a PPMgO:LN ridge waveguide crystal pumped by a DBR tapered diode laser," *Opt. Lett.*, vol. 41, no. 7, pp. 1530–1533, 2016.

[8] J. Koeth, M. Fischer, M. Legge, J. Seufert, and R. Werner, "High performance quantum dot distributed feedback laser diodes around 1.15 $\mu$m," in *Proc. SPIE*, 2008, p. 690904. [Online]. Available: http://dx.doi.org/10.1117/12.763157

[9] H. Virtanen *et al.*, "Spectral characteristics of narrow-linewidth high-power 1180 nm DBR laser with surface gratings," *IEEE Photon. Technol. Lett.*, vol. 29, no. 1, pp. 114–117, Jan. 1, 2017.

[10] V.-M. Korpijärvi, J. Viheriälä, M. Koskinen, A. T. Aho, and M. Guina, "High-power temperature-stable GaInNAs distributed Bragg reflector laser emitting at 1180 nm," *Opt. Lett.*, vol. 41, no. 4, pp. 657–660, 2016.

[11] J. Viheriälä *et al.*, "Applications of UV-nanoimprint soft stamps in fabrication of single-frequency diode lasers," *Microelectron. Eng.*, vol. 86, no. 3, pp. 321–324, Mar. 2009.

[12] H. Wenzel, R. Guther, A. M. Shams-Zadeh-Amiri, and P. Bienstman, "A comparative study of higher order Bragg gratings: Coupled-mode theory versus mode expansion modeling," *IEEE J. Quantum Electron.*, vol. 42, no. 1, pp. 64–70, Jan. 2006.

[13] M. Achtenhagen, N. V. Amarasinghe, and G. A. Evans, "High-power distributed Bragg reflector lasers operating at 1065 nm," *Electron. Lett.*, vol. 43, no. 14, pp. 755–757, Jul. 2007.

[14] *MS9710C Optical Spectrum Analyzer Operation Manual*, 11th ed. Atsugi, Japan: Anritsu Corporation, 2008.

# PUBLICATION

# II

**High-Power 1.5- μm Broad Area Laser Diodes Wavelength Stabilized by Surface Gratings**

A. T. Aho, J. Viheriälä, H. Virtanen, T. Uusitalo and M. Guina

*IEEE Photonics Technology Letters* 30.21 (2018), 1870–1973
DOI: 10.1109/LPT.2018.2870304

# High-Power 1.5-$\mu$m Broad Area Laser Diodes Wavelength Stabilized by Surface Gratings

Antti T. Aho, Jukka Viheriälä, Heikki Virtanen, Topi Uusitalo, and Mircea Guina

***Abstract*— Wavelength stabilization against temperature variation of high-power broad area 1.5-$\mu$m InGaAsP/InP laser diodes is demonstrated by employing surface gratings. The development targets application in eye-safe automotive LIDAR systems, which would benefit from deploying narrowband receiver filters to block ambient solar radiation for improved signal-to-noise ratio. The surface grating is monolithically integrated on the laser chip using nanoimprint lithography. The peak power of the lasers exceeded 6 W in pulsed mode, for an FWHM spectral width of 0.3 nm and a peak wavelength drift of only 0.1 nm/°C. The wavelength shift with temperature is reduced by five times compared to broad area high-power Fabry–Perot laser diodes typically employed in LIDAR systems.**

***Index Terms*— Diode lasers, distributed Bragg reflector, high power, LIDAR.**

## I. Introduction

LIDAR applications are experiencing a fast rate of development owing to many high-value emerging needs, such as obstacle detection and avoidance for autonomous vehicles, robotics, and augmented reality. To this end, the 800 nm–900 nm wavelength range is commonly used since both high-power laser sources and low noise cheap and fast detectors are readily available [1]. However, a serious limitation in this wavelength range is the requirement for eye-safety, which limits the maximum permissible output power and thus the range of the LIDAR imaging. A higher output power can be used at longer wavelengths: for example, the maximum permissible exposure (MPE) of the human cornea for a 1 $\mu$s laser pulse is 1 Jcm$^{-2}$ at 1500 nm but only 32 $\times$ 10$^{-7}$ Jcm$^{-2}$ at 800 nm [2]. Additional benefits obtained by using longer wavelengths are reduced scattering by small particles, which enhances the operation capability in adverse weather conditions [3], and a low level of optical losses caused by the atmosphere, both limiting the visibility range of the LIDAR systems working at shorter wavelengths.

The wavelengths around 1.5 $\mu$m are commonly used in military LIDAR and range-finding applications [4], but since they are often based on a fiber laser [5], many current solutions are too bulky and unwieldy for compact applications. Since the output power of 1.5 $\mu$m diode lasers is lacking compared to 1.5 $\mu$m fiber lasers and 900 nm diode lasers, a precisely controlled narrow spectrum is advantageous in sensing applications because it enables the use of narrow passband optical filters in front of the sensor, reducing the solar background noise and improving the signal-to-noise ratio.

To address these application challenges, we demonstrate a 1.5 $\mu$m broad area laser diode with a monolithically integrated Bragg grating to act as a compact, cost-effective high-power laser source at an eye-safe wavelength and exhibiting a well-controlled and narrow spectrum. Recently, broad area distributed Bragg reflector laser diodes (DBR-LDs) have been demonstrated at 905 nm with 50 W output power in 10 ns pulsed operation [6]. Moreover, a broad area distributed feedback (DFB) laser has been demonstrated, exhibiting 5.5 W output power around 970 nm [7]. At 1.55 $\mu$m, a high-power DBR-LD has been demonstrated using a tapered power amplification section resulting in 0.6 W CW power [8], while we demonstrated pulsed operation from a similar kind of component with 1.6 W peak power [9].

We incidentally show that the wavelength locking with a DBR geometry eliminates the wavelength variation caused by the change in the gain spectrum over the semiconductor substrate, which typically causes a variation of emission spectrum in broad area Fabry-Perot (FP) high-power lasers, reducing the yield of components emitting at a specific peak wavelength. The gratings also provide wavelength stability against temperature variation, resulting in a wavelength drift reduced by about five times compared to the FP-LD, again enabling the use of narrow band-pass receiver filters. We elaborate the fabrication of the DBR-LD based on regrowth-free surface gratings patterned with soft-UV Nanoimprint Lithography (NIL) – a combination enabling cost-effective grating fabrication. Additionally, monolithically integrated gratings avoid the need to precisely assemble and adjust the external grating elements one-by-one as is the case with, for example, volume Bragg grating technology. Finally, the results show that the benefits of the DBR-LDs can be obtained without a significant performance penalty in power compared to FP-LDs.

## II. Fabrication Details

The semiconductor structure comprised three InGaAsP quantum wells (QWs) surrounded by 1.6 $\mu$m InGaAsP optical confinement layers and InP claddings, and was grown

Manuscript received August 24, 2018; accepted September 11, 2018. Date of publication September 17, 2018; date of current version November 6, 2018. This work was supported in part by the H2020-ECSEL-2015 Project DENSE under Grant 692449, in part by the HPY Research Foundation, in part by the Finnish Foundation for Technology Promotion, in part by the KAUTE Foundation, and in part by Emil Aaltonen's Foundation. *(Corresponding author: Antti T. Aho.)*

The authors are with the Optoelectronic Research Centre, Tampere University of Technology, 33720 Tampere, Finland (e-mail: antti.t.aho@tut.fi; jukka.viheriala@tut.fi; heikki.a.virtanen@tut.fi; topi.uusitalo@tut.fi; mircea.guina@tut.fi).

Color versions of one or more of the figures in this letter are available online at http://ieeexplore.ieee.org.

Digital Object Identifier 10.1109/LPT.2018.2870304

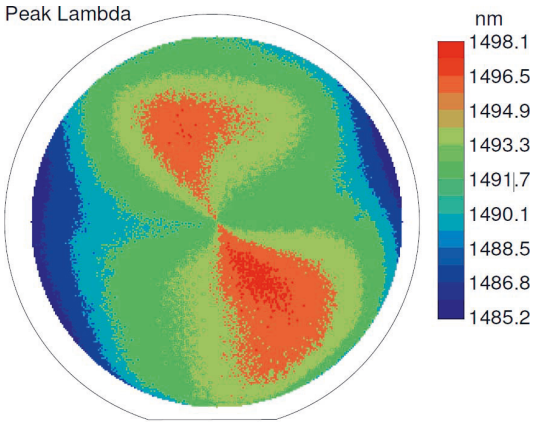


Fig. 1. Measured PL spectrum variation over the 2″ wafer used in the fabrication process.

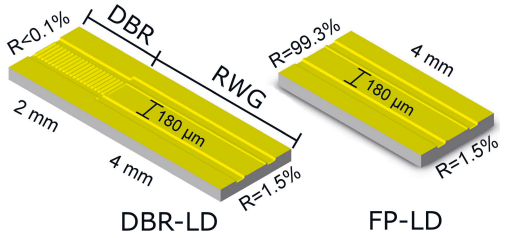


Fig. 2. Left side: drawing of the DBR-LD showing section lengths, RWG width and facet reflectivities after coating. Right side: drawing of the FP-LD showing the component length, RWG width and facet reflectivities after coating.

on 2″ n-InP(100) with metalorganic vapor phase epitaxy (MOVPE). The MOVPE system produces up to 12 wafers with 2″ size in a single batch and one of them was selected for the study. The QW photoluminescence (PL) correlating to FP-LD emission spectrum had a peak wavelength between 1485 nm and 1498 nm (13 nm variation) depending on the position on the substrate (see Fig. 1).

The DBR-LDs comprised two sections: a 2 mm long passive (un-pumped) third-order DBR grating section and a 4 mm long active (pumped) gain-guided ridge waveguide (RWG) section. An illustration of the component is shown on the left side in Fig. 2. A total of five different component variants were fabricated and tested with RWG and DBR widths of 180 $\mu$m and 170 $\mu$m, respectively, and five equally-spaced grating periods from 678.4 nm to 686.4 nm.

The DBR gratings were fabricated using soft-stamp nanoimprint lithography [10] with EVG620 mask aligner and a stamp area of 25 mm x 25 mm. The stamp was used to imprint a thin film of mr-UVCur06 photoresist (Micro resist technology GmbH) deposited on top of a SiN layer grown on the semiconductor. The photoresist was used to etch the SiN which in turn was used as a mask for etching the semiconductor. The semiconductor was etched using reactive ion etching (RIE) with $CH_4/H_2$ chemistry to a depth of 1010 nm from the surface

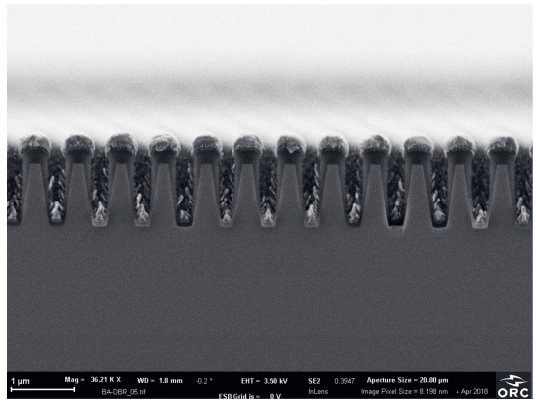


Fig. 3. Scanning electron microscope image of the grating cross-section.

of the semiconductor, 190 nm above the p-side waveguide. The etching process produced a V-shaped grating (see Fig. 3). The semiconductor filling factor was 67 % at the bottom of the grating and 24 % at the top of the grating. The walls of the grating were at an angle of 99.5°. The grating was simulated with the method outlined in [11]. This model assumes a rectangular grating with a constant filling factor, but a V-shaped grating with small sidewall angles can be approximated as a rectangular grating with a filling factor slightly smaller than at the bottom of the V-shaped grating [11]. To generate a suitable approximation, the vertically varying filling factor of the V-shaped grating was accounted for by calculating the grating parameters (coupling coefficient $\kappa$, radiative loss coefficient $\alpha_{\mathrm{rad}}$) as functions of the filling factor and then taking a weighted average in the vertical direction from the bottom of the grating to the top of the grating. The optical field intensity was used as the weighing function. This simulation yielded $\kappa = 4.8\ \mathrm{cm}^{-1}$, $\alpha_{\mathrm{rad}} = 4.6\ \mathrm{cm}^{-1}$, and peak grating reflectivity $R_{\mathrm{max}} = 0.44$.

The current confining RWG sections were fabricated using photolithography and RIE with $CH_4/H_2$ chemistry. They were etched to a depth of 500 nm from the surface of the semiconductor, reducing the unintentional current spreading in the heavily p-doped layers.

The injection current was limited to pass through the top of the ridge by covering the top of the wafer with $SiO_2$ and etching an opening on top of the ridges using photolithography and RIE. The p-side of the wafer was metallized using a Ti/Pt/Au layer stack and patterned using photolithography and a lift-off process. Finally, the wafer was thinned from n-side to a thickness of $\sim$110 $\mu$m by lapping with an $AlO_x$ abrasive, metallized with a Ni/Au/Ge/Au layer stack, and annealed at 430 °C.

The finished wafer was cleaved into DBR-LD bars, comprising both DBR and RWG sections, and FP-LD bars, comprising only the RWG section (shown on the right side in Fig. 2). The front facets of both types of bars were coated with a single layer of $Al_2O_3$ with a target reflectance of 1.5 %. The back facets of the DBR-LD bars were coated with an $Al_2O_3/TiO_2/Al_2O_3$ stack with a target reflectance below 0.01%, and the back facets of the FP-LD bars were coated

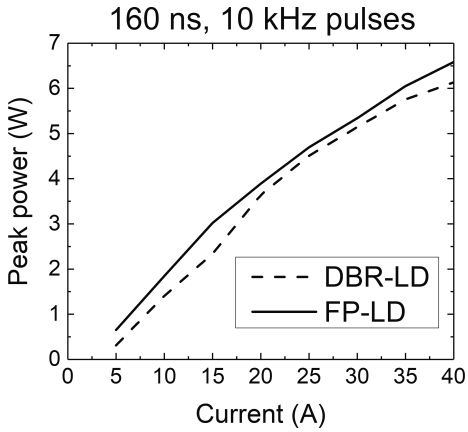


Fig. 4. The peak power of the DBR-LD and the FP-LD measured with 160 ns, 10 kHz pulses.

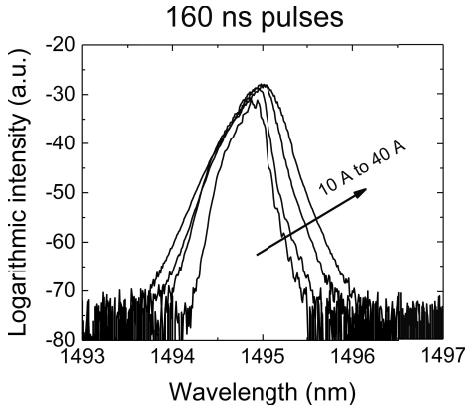


Fig. 5. Spectra from a DBR-LD with 160 ns pulses. The FWHM at 40 A injection current is 0.30 nm. The resolution is 0.05 nm.

with eight $Al_2O_3/TiO_2$ layer pairs with a target reflectance of 99.3 %. The coatings were performed with Cutting Edge Coatings NAVIGATOR 700 ion beam sputtering system. After the coating, the bars were scribed into individual chips with a width of 400 $\mu$m. The length of the DBR-LD components was 6 mm and the length of the FP-LD components was 4 mm. Finally, the chips were mounted p-side up on metallized AlN submounts with silver epoxy glue and wire-bonded.

## III. Laser Performance

The components were characterized in pulsed operation with 160 ns, 10 kHz pulses (Dr. Heller Elektronik HLD 500-50 pulsed laser driver) and 1 $\mu$s, 10 kHz pulses (DEI Scientific PCX-7420 pulsed laser driver). The peak power of the components was measured with 160 ns current pulses with an amplitude between 0 A to 40 A. An example current–peak power (IL) curve, recorded with a Thorlabs DET08CL/M 5 GHz InGaAs photodetector and Agilent DSO9254A 2.5 GHz oscilloscope, is shown in Fig. 4. The calibration of the fast photodiode was obtained by correlating the recorded oscilloscope waveform to the average power measured with a calibrated integrating sphere. The DBR-LDs reached a peak output power of 6.1 W, while the FP-LDs reached a peak output power of 6.6 W.

The spectra of the DBR-LDs was measured up to 40 A injection current with 160 ns pulses (Yokogawa AQ6375 optical spectrum analyzer) and up to 15 A with 1 $\mu$s pulses (Antritsu MS9710C optical spectrum analyzer). The resolution in both measurement setups was 0.05 nm. A typical full width at half-maximum (FWHM) spectral width of the DBR-LDs was 0.30 nm. As a reference, the FWHM of the FP-LD was 6.9 nm at 40 A current. The spectra from a DBR-LD at various injection currents are shown in Fig. 5.

The effect of the DBR grating on the emission wavelength stability at different mount temperatures was studied by comparing the peak wavelength shift of the DBR-LD components to the peak wavelength shift of the FP-LD components. The measured spectra are shown in Fig. 6.

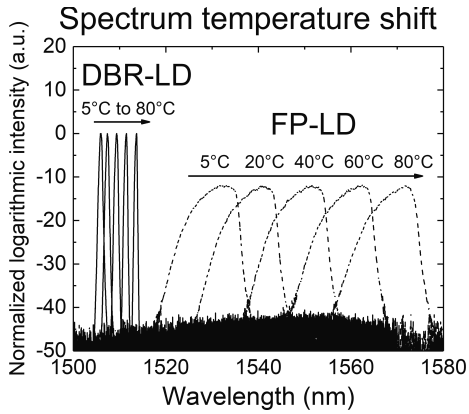


Fig. 6. The spectra of a DBR-LD chip (solid lines) and a FP-LD chip (dashed lines) at various temperatures measured in 1 $\mu$s pulsed operation. The DBR-LD peak wavelength shifts at a rate of 0.1 nm/°C and the FP-LD peak wavelength shifts at a rate of 0.5 nm/°C.

The DBR-LDs exhibited a peak wavelength shift of 0.1 nm/°C while the FP-LDs exhibited a peak wavelength shift of 0.5 nm/°C. This is expected, since in the DBR-LD the emission wavelength shift is dominated by the change in the refractive index of the DBR grating [12], and in the FP-LD the emission wavelength shift is caused by the change in the QW bandgap [13]. Furthermore, in the DBR-LDs, the peak wavelength was linearly dependent on the DBR grating period as shown in Fig. 7, demonstrating that the grating can be used to control the emission wavelength accurately even when the gain maximum is detuned by over 30 nm. Fig. 7 also shows the effective refractive index $n_{eff}$ calculated from the measured emission wavelengths $\lambda$, known grating periods $\Lambda$, and known grating order $l$ using the equation for the Bragg condition [14]

$$l\frac{2\pi}{\Lambda} = \frac{4\pi n_{eff}}{\lambda}. \tag{1}$$

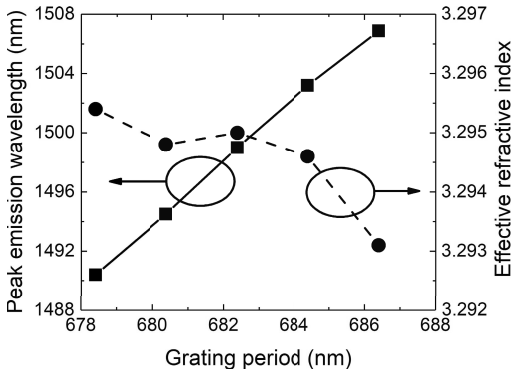


Fig. 7. The peak emission wavelength of the DBR-LD at 20 °C mount temperature and 10 A, 1 $\mu$s pulsed injection across multiple components with different DBR grating periods and corresponding effective refractive indices. The gain maximum of the components was at 1522 nm.

## IV. Conclusion

In conclusion, we reported high-power broad-area 1.5 $\mu$m InGaAsP DBR laser diodes with parameters targeting eye-safe LIDAR, range-finding, and flash illumination applications. The spectral properties provided by the DBR-LDs enable the implementation of systems with low noise receivers by employing narrow pass-band filters. The DBR locks the lasing to the grating even when the detuning between the gain and the grating is over 30 nm, enabling the fabrication of large batches of LDs with identical emission characteristics and high yield. With 160 ns, 40 A injection pulses, the components exhibited a peak output power of 6.1 W and 0.30 nm spectral FWHM. The peak emission wavelength drifted by 0.1 nm/°C, which is five times less than for the FP-LD component geometry.

## Acknowledgment

The authors wish to acknowledge the contribution of Modulight, Inc., which provided the epiwafer, and the work done by M.Sc. Mervi Koskinen in component fabrication, M.Sc. Jarno Reuna in thin film coating, and M.Sc. Heidi Tuorila in measurement setup construction.

## References

[1] B. Schwarz, "LIDAR: Mapping the world in 3D," *Nature Photon.*, vol. 4, no. 7, pp. 429–430, 2010.

[2] *Safety of Laser Products—Part 1: Equipment Classification and Requirements*, document IEC 60825-1:2014, International Electrotechnical Commission, 2014.

[3] A. Samman *et al.*, "Potential use of near, mid and far infrared laser diodes in automotive LIDAR applications," in *Proc. 52nd Veh. Technol. Conf. (VTC)*, Boston, MA, USA, Sep. 2000, pp. 2084–2089.

[4] O. Steinvall, R. Persson, F. Berglund, O. K. S. Gustafsson, and F. Gustafsson, "Using an eyesafe military laser range finder for atmospheric sensing," in *Proc. SPIE Def.+ Sec.*, Baltimore, MD, USA, vol. 9080, Jun. 2014, p. 90800W. [Online]. Available: https://www.spiedigitallibrary.org/conference-proceedings-of-spie/9080/90800W/Using-an-eyesafe-military-laser-range-finder-for-atmospheric-sensing/10.1117/12.2049044.short?SSO=1, doi: 10.1117/12.2049044.

[5] F. Amzajerdian, D. F. Pierrottet, G. D. Hines, L. Petway, and B. W. Barnes, "Fiber-based Doppler lidar for vector velocity and altitude measurements," in *Proc. Frontiers Opt.*, San Jose, CA, USA, Oct. 2015, Paper LTu3I.2.

[6] A. Knigge *et al.*, "Wavelength-stabilized high-pulse-power laser diodes for automotive LiDAR," *Phys. Status Solidi A*, vol. 215, no. 8, p. 1700439, 2018.

[7] J. Fricke *et al.*, "High-brilliance diode lasers with monolithically-integrated surface gratings as sources for spectral beam combining," in *Proc. High Power Diode Lasers Syst. Conf. (HPD)*, Coventry, U.K., Oct. 2013, pp. 2–3.

[8] S. R. Selmic *et al.*, "Single frequency 1550-nm AlGaInAs-InP tapered high-power laser with a distributed Bragg reflector," *IEEE Photon. Technol. Lett.*, vol. 14, no. 7, pp. 890–892, Jul. 2002.

[9] A. T. Aho *et al.*, "High-power 1550 nm tapered DBR laser diodes for LIDAR applications," in *Proc. Eur. Conf. Lasers Electro-Opt.*, Munich, Germany, 2017, Paper CB_7_4.

[10] J. Viheriälä *et al.*, "Applications of UV-nanoimprint soft stamps in fabrication of single-frequency diode lasers," *Microelectron. Eng.*, vol. 86, no. 3, pp. 321–324, Mar. 2009.

[11] H. Wenzel, J. Fricke, J. Decker, P. Crump, and G. Erbert, "High-power distributed feedback lasers with surface gratings: Theory and experiment," *IEEE J. Sel. Top. Quantum Electron.*, vol. 21, no. 6, pp. 352–358, Nov./Dec. 2015.

[12] L. A. Coldren, S. W. Corzine, and M. L. Mašanović, "Mirrors and resonators for diode lasers," in *Diode Lasers and Photonic Integrated Circuits*, 2nd ed. Hoboken, NJ, USA: Wiley, 2012, p. 135.

[13] K. P. O'Donnell and X. Chen, "Temperature dependence of semiconductor band gaps," *Appl. Phys. Lett.*, vol. 58, no. 25, pp. 2924–2926, 1991.

[14] L. A. Coldren, S. W. Corzine, and M. L. Mašanović, "Perturbation, coupled-mode theory, modal excitations, and applications," in *Diode Lasers and Photonic Integrated Circuits*, 2nd ed. Hoboken, NJ, USA: Wiley, 2012, p. 344.

# PUBLICATION

# III

**High-Power 1.5 μm Tapered Distributed Bragg Reflector Laser Diodes for Eye-Safe LIDAR**

A. T. Aho, J. Viheriälä, M. Koskinen, T. Uusitalo, J. Reuna and M. Guina

*IEEE Photonics Technology Letters* 32.19 (2020)
DOI: 10.1109/LPT.2020.3019845

# High-power 1.5 μm tapered distributed Bragg reflector laser diodes for eye-safe LIDAR

Antti T. Aho, Jukka Viheriälä, Mervi Koskinen, Topi Uusitalo, Jarno Reuna, and Mircea Guina

***Abstract*—A high-power InAlGaAs/InP tapered distributed Bragg reflector laser diode with narrow linewidth emission at 1.5 μm is reported. The laser has a monolithic waveguide architecture comprising a third-order grating section for longitudinal mode selection, an index-guided gain section for lateral mode filtering, and a gain-guided tapered section for power scaling. An output power of 770 mW is reported for continuous wave operation at room temperature. In pulsed mode, the laser delivered a peak power of 4.6 W with a full width at half-maximum spectral linewidth of only 250 pm. In addition to the narrow linewidth and high-power features, the emission wavelength exhibits a temperature dependent shift of only 0.1 nm/°C. The parameters achieved suggest that these laser diodes would enable the realization of compact LIDAR systems with improved signal-to-noise ratio, owing to the high output power and the possibility to use narrow passband filters at receiver side, which is enabled by the narrow and temperature-stable emission spectrum. The wavelength range around 1.5 μm also enables LIDAR systems with high output powers while maintaining eye safety, ultimately leading to improved system performance.**

***Index Terms*— Diode lasers, distributed Bragg reflector, high power, LIDAR.**

## I. Introduction

LIGHT detection and ranging (LIDAR), and 3D sensing applications in general, are currently receiving a high level of attention for being one of the key technologies for autonomous vehicles [1], systems for augmented reality [2], use of drones for security measures [3], and numerous other applications e.g. in agriculture [4], forestry [5], and meteorology [6]. Current LIDAR systems in automotive applications operate in the wavelength range around 900 nm where both high-power laser diodes and cost effective Si-based detectors are readily available [7]. On the other hand, the need to increase the detection range and enable operation in adverse weather conditions requires higher output powers at levels that approach the eye-safety limit. When considering eye safety, the wavelength range around 1.5 μm enables several orders of magnitude higher output power [8], while at the same time small particles in the air cause less scattering [9].

When it comes to LIDAR implementation, we should note that moving to 1.5 μm wavelength range typically involves the use of a scanning beam technique incorporating low-cost, low-noise, single-pixel InGaAs detectors at the receiver side. This is required in order to cope with the lack of cost-effective detector arrays, similar to those that Si-based technology offers at short-infrared wavelengths. On the other hand, the use of a scanning beam technique makes the requirements concerning beam quality more critical. In turn, this obstructs the use of high power broad area lasers, which are normally used in line scanning or flash illumination 3D imaging approaches at shorter wavelengths, due to their poor beam quality. Moreover, while InP-based laser diodes have been a mature technology for a long time, their emission power for continuous-wave (CW) single-mode operation is typically only tens of milliwatts, with the highest level of 100 mW reported for components without a tapered waveguide section [10]. When using tapered sections, the power has been scaled to about 0.6 W for CW operation [11], while we have reported pulsed operation with a peak power of 1.6 W [12]. The power levels should be significantly scaled up before this laser diode technology becomes a serious contender for the established LIDAR technology solutions. For generality, we should also note that the highest power reported for a distributed Bragg reflector (DBR) broad-area multi-mode laser diode is in the range of 6 W for pulsed operation [13].

In this paper, we address the power scaling using a tapered power amplifier in combination with a single-mode ridge waveguide (RWG) section [14]. Additionally, we use a DBR grating to narrow down the output spectrum and reduce the wavelength drift caused by changes in the device operating temperature, both features being essential for the use of narrow-band optical filters at the LIDAR receiver for improved signal-to-noise ratio and for reducing the solar blinding effect [15]. In particular, we report a tapered laser with a room temperature output power of 770 mW in CW mode and 4.6 W pulsed peak power, which is almost a three-fold increase compared to the previously reported highest power results [12]. Moreover, we demonstrate how the use of the DBR grating is beneficial also in reducing the output power decline at elevated temperatures.

Manuscript submitted June 23, 2020. This work was supported by H2020-ECSEL-2015 project DENSE (692449), Business Finland project "3D-LIDAR ecosystem" (1613/31/2018), and Academy of Finland project "Single photon detection based 2D/3D ranging in high background illumination conditions" (317145). This work is part of the Academy of Finland Flagship Programme PREIN (320168). A. T. Aho is acknowledging the support received from HPY Research Foundation, the Finnish Foundation for Technology Promotion, KAUTE Foundation, Emil Aaltonen's Foundation, and Jenny and Antti Wihuri Foundation.

A. T. Aho, J. Viheriälä, M. Koskinen, T. Uusitalo, J. Reuna, and M. Guina are with the Optoelectronics Research Centre, Tampere University, Korkeakoulunkatu 3, 33720 Tampere, Finland (email: antti.aho@tuni.fi, jukka.viheriala@tuni.fi, mervi.koskinen@tuni.fi, topi.uusitalo@tuni.fi, jarno.reuna@tuni.fi, mircea.guina@tuni.fi).

An analysis of the beam quality factor $M^2$ for CW and pulsed operation is also provided, pointing to the limitations of the design of the semiconductor epitaxial structure employed in the study.

## II. Fabrication Details

The semiconductor structure was grown on 2" n-InP wafer using MOCVD. It comprised four InAlGaAs quantum wells (QWs) surrounded by InAlGaAs barriers, InAlGaAs optical confinement layers, InAlAs barrier layers, and InP claddings. The measured peak photoluminescence wavelength was approximately at 1500 nm. The waveguide architecture of the tapered DBR lasers comprised three sections: a 2 mm long passive third order DBR grating section for longitudinal mode selection, a 1 mm long active index-guided RWG section for lateral mode filtering, and a 4 mm long active gain guided tapered power scaling section with a 5° opening angle. Fig. 1 shows an illustration of the waveguide design in the longitudinal direction. The width of the waveguide in the DBR and RWG sections was 1.5 µm, and they were surrounded on both sides by a 12 µm wide trench etched into the semiconductor. Five different component variants were fabricated with grating periods ranging from 721.7 nm to 727.4 nm to ensure that a device with a suitable detuning between the gain maximum and the DBR resonance wavelength was obtained. The grating duty cycle was 50 % at the surface and the etch depth was 560 nm above the waveguide layer.

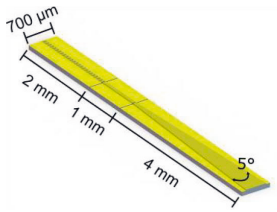


Fig. 1. A schematic drawing of the tapered DBR laser diode depicting the main features.

The DBR grating lines and the ridge were fabricated using soft-stamp nanoimprint lithography (NIL) [16] with EVG620 mask aligner and mr-UVCur06 photoresist (micro resist technology GmbH). SiN was used as the etching mask. The etching of the semiconductor was done using reactive ion etching (RIE) with $CH_4/H_2$ chemistry. After the etching step, the sample was planarized using benzocyclobutene (BCB) and covered with $SiO_2$. Then the dielectric layer was opened on top of the ridges and the tapered waveguides using photolithography and RIE with $CHF_3/O_2$ chemistry. Finally, the p-side was metallized with a Ti/Pt/Au layer stack, the wafer was thinned from the n-side to a thickness of about 130 µm, and the n-side was metallized with a Ni/Au/Ge/Au layer stack. The contacts were annealed at 370 °C. After the annealing, an additional Ni/Au layer pair was added to the n-side to facilitate wire bonding.

The wafer was cleaved into bars and the facets were coated using Cutting Edge Coatings NAVIGATOR 700 ion beam sputtering system. The target reflectance of the front and back facet were 1.5% and < 0.05%, respectively. A nonzero front facet reflectance was required to enable feedback to the cavity, while as small back facet reflectance as possible was beneficial to allow the DBR grating reflectance to dominate and filter the longitudinal modes. After coating, the bars were scribed into 700 µm wide chips and mounted p-side up on metallized AlN submounts with silver epoxy glue and wire bonded. Some of the devices were soldered p-down with AuSn on AlN-submount to allow a lower thermal resistance and to enable CW operation.

## III. Experimental Results

The initial characterization targeted the demonstration of high peak power operation with a pulse duration suitable for LIDAR. To this end, the RWG section was biased with 200 mA DC current using an Analog Technologies ATLS1A103 laser driver. The tapered section was driven with 160 ns long current pulses at a 10 kHz repetition rate and amplitude ranging from 5 A to 40 A using Dr. Heller Elektronik HLD 500-50 pulsed laser driver. The values chosen for the measurements are linked to the performance of the available current driver and connectors between the driver and the laser rather than the ability of the laser diode to handle shorter optical pulses. Although technically challenging, standard gain dynamics of laser diodes support operation in the range of a few nanoseconds if suitable drivers are employed [17]. The averaged optical power was measured using a calibrated UMBK-150 integrating sphere with an InGaAs photodiode from Gigahertz-Optik GmbH. The spectra were measured using Ando AQ-6315A optical spectrum analyzer with 0.05 nm resolution.

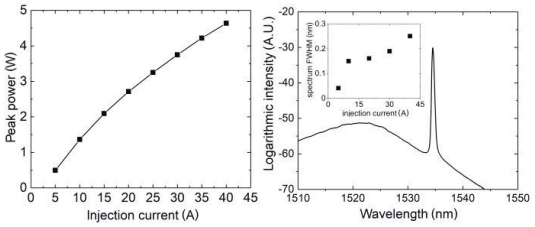


Fig. 2. Left: Peak output power of the tapered DBR laser diode as a function of the current amplitude injected into the tapered section at 20 °C mount temperature. The RWG section was biased with a 200 mA DC current, while the tapered section was driven in pulsed mode with 160 ns pulses at 10 kHz repetition rate. Right: Spectrum of a tapered DBR laser diode at 20 °C mount temperature, 200 mA DC bias to RWG section and 40 A, 160 ns, 10 kHz injection pulses to tapered section. The inset shows the spectral FWHM as a function of the tapered section injection current. The measured FWHM values show that although the devices exhibit narrow emission spectrum, they are not single mode.

At 20 °C mount temperature, the devices reached 4.6 W peak power. Fig. 2 shows the current–power (IL) -characteristic of a tapered DBR laser as a function of the injection current amplitude in the tapered section, as well as an exemplary spectrum of a component at 40 A injection current. The inset shows the spectral full width at half-maximum (FWHM) measured at various injection currents. At the maximum current

of 40 A, the spectral FWHM was 250 pm. Based on a 2D CAMFR simulation we estimate that the DBR has a reflection in the range of 40% and it is saturated with the used grating length. In light of earlier studies [18] the rear reflectivity has small impact on the slope efficiency with the main limitation arising from the relatively high internal losses estimated to be around 10 $cm^{-1}$.

The effect of the RWG section injection current was studied by applying a constant DC current to the taper section, sweeping the RWG section injection current, and measuring the output power. The result from this measurement is shown in Fig. 3. Depending on the taper section injection current, the effect of the RWG section current saturates at around 200 mA. Increasing the taper section current moves the saturation point to smaller RWG section injection current values.

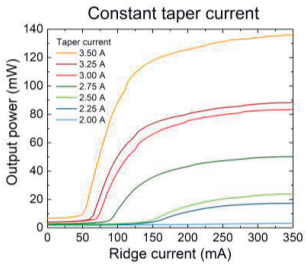


Fig. 3. Output power with constant DC tapered section current and varying the RWG section current at 20 °C mount temperature.

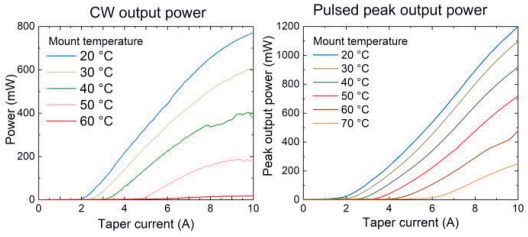


Fig. 4. Output power in CW and pulsed operation modes at various mount temperatures. Pulse parameters were 1 µs pulse length and 10 kHz repetition rate. The RWG section was biased with 200 mA DC current.

The effect of the mount temperature on the output power was studied in both CW and pulsed operation modes. The results are shown in Fig. 4. The power behaviour is as expected: The highest output powers are obtained at the lowest temperatures. However, since the DBR resonance wavelength is longer than the peak gain wavelength of the active region, as shown in Fig. 2, the detrimental effect of the increasing temperature is somewhat mitigated by the increased overlap of the gain and the grating resonance as the temperature is increased. In CW, some thermal roll-over is already showing at 10 A injection current, while in pulsed operation the output power increases steadily from the threshold current up to 10 A. There is some nonlinearity in both CW and pulsed mode at some currents and temperatures, which is attributable to either mode hopping in the DBR grating or filamentation in the tapered section.

Spectral measurements in pulsed mode at temperatures from 20 °C to 70 °C showed that the peak emission wavelength shifts at a rate of ~0.1 nm/°C, which demonstrates that the grating reduces the temperature induced wavelength shift of the emission. In a device without the grating and a similar material system, the peak gain wavelength shift was 0.5 nm/°C.

The beam quality factor $M^2$ was measured in pulsed and CW operating modes using Thorlabs M2MS measurement system with a Thorlabs BP209-IR dual scanning slit beam profiler. The beam astigmatism resulting from the tapered section was corrected using a C-coated aspheric lens with 3.10 mm effective focal length (EFL) from AMS Technologies for fast axis collimation and a C-coated acylindrical lens with 15 mm EFL from Asphericon GmbH for slow axis collimation. The collimated beam was focused using a C-coated achromatic doublet lens with 150 mm EFL from Thorlabs. In pulsed mode, the pulse length was 50 ns and the repetition rate was increased to 200 kHz to enable the measurement using the scanning slit system. Fig. 5 shows the measured beam quality factors at various tapered section injection currents. All reported values are calculated from second-moment beam widths (D4σ) according to the measurement standard [19], since the beam shape is very far from Gaussian especially in the slow axis direction. The side-lobes and their relative intensity changes compared to the main lobe in the beam profile would cause large discontinuous position-dependent fluctuations in the commonly used $1/e^2$ beam width, rendering it unusable for evaluating the beam quality.

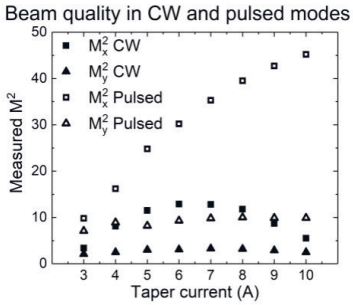


Fig. 5. Beam quality factor $M^2$ of the laser diodes measured in CW and pulsed operation with various taper currents at 20 °C mount temperature and 200 mA CW RWG section current.

It can be seen in Fig. 5 that at all currents, both in pulsed and CW mode, the $M^2$ value is quite high in both fast and slow axis directions. In pulsed mode, the $M^2$ is much higher than in CW, and in both operation modes, $M^2_X$ deteriorates quickly with increasing output power while $M^2_Y$ stays nearly constant. The poor beam quality in the slow axis direction can be attributed to the high modal gain of the structure resulting from a high confinement factor (simulated as $\Gamma = 3.6$ %), which may lead to spatial hole burning that causes self-focusing and filamentation of the beam inside the tapered section [20]. In CW operation mode, $M^2_X$ starts to decrease after 6 A injection current while in pulsed mode it increases monotonically. This is probably due to insufficient thermal conductivity of the mount in our $M^2$ measurement setup, leading to thermal roll over of the laser and reduction in the output power at high DC injection currents.

Stagnation of the optical output power after the roll over also limits the beam quality degradation caused by the spatial hole burning.

In the fast axis direction, the poor beam quality may be explained by the large leakage of the mode into the cladding layers and interaction with the contact layer. A simulation of the fundamental optical mode in the laser structure, done for 300 K material temperature with SimuLase software (Nonlinear Control Strategies Inc.), indicates that the optical field intensity at the p-side contact layer is ~4.8% of the maximum field intensity. This indicates that the interaction could be a reason for an increase in $M^2_Y$.

The difference between the pulsed beam quality and CW beam quality may also be explained to an extent by the high modal gain of the structure. High modal gain moves the lasing threshold towards lower injection current densities, where the effect of the change in the carrier density on the complex refractive index is higher than at high injection current densities [21], [22]. Thus, when the carrier density changes rapidly during the injection pulse, the refractive index profile of the tapered section is perturbed and the beam quality is reduced.

## IV. Conclusions

We have reported high-power 1.5 µm InAlGaAs tapered DBR laser diodes with the application target in eye-safe automotive LIDAR systems. At room temperature, the devices exhibited 4.6 W peak output power with 250 pm spectral FWHM in pulsed operation, and 770 mW output power in CW operation. The peak emission wavelength of the components is locked to the DBR grating, reducing the temperature change induced wavelength shift, which would enable the use of narrow passband receiver filters to block ambient radiation in a LIDAR system and improve the signal-to-noise ratio. The components exhibit almost a three-fold improvement in the pulsed output power compared to previously reported tapered components with a similar design, and comparable (although slightly lower) output power level with previously reported BA-DBR laser diodes. Although the beam quality of the lasers is far from perfect, they provide a better beam quality than conventional broad area lasers and therefore enable LIDAR systems with a better lateral resolution. In the future, we expect that by utilizing a gain material with a smaller confinement factor and modal gain we can fabricate components with a significantly better beam quality, further improving the lateral resolution and collimation capability. Finally, a system utilizing a monolithic DBR laser would have a reduced assembly cost and a smaller footprint compared to solutions exploiting gain switched laser diodes and 1.5 µm fiber amplifiers.

## References

[1] R. H. Rasshofer and K. Gresser, "Automotive Radar and Lidar Systems for Next Generation Driver Assistance Functions," *Adv. in Rad. Sci.,* vol. 3, pp. 205-209, 2005.

[2] R. Wang, "3D building modeling using images and LiDAR: a review," *Int J Image Data Fusion,* vol. 4, no. 4, pp. 273-292, 2013. DOI: 10.1080/19479832.2013.811124.

[3] N. M. Noor, A. Abdullah and M. Hashim, "Remote sensing UAV/drones and its applications for urban areas: a review," *IOP Conf. Ser.: Earth Environ. Sci.,* vol. 169, no. 1, pp. 012003, 2018. DOI: 10.1088/1755-1315/169/1/012003.

[4] H. Mousazadeh, "A technical review on navigation systems of agricultural autonomous off-road vehicles," *J Terramechanics,* vol. 50, no. 3, 2013. DOI: 10.1016/j.jterra.2013.03.004.

[5] M. A. Wulder, J. C. White, R. F. Nelson, E. Naesset, H. O. Orka, N. C. Coops, T. Hilker, C. W. Bater and T. Gobakken, "Lidar sampling for large-area forest characterization: A review," *Remote Sens. Environ.,* vol. 121, pp. 196-209, 2012. DOI: 10.1016/j.rse.2012.02.001.

[6] K. Sassen, "The Polarization Lidar Technique for Cloud Research: A Review and Current Assessment," *Bull. Amer. Meteor. Soc.,* vol. 72, no. 12, pp. 1848-1866, 1991. DOI: 10.1175/1520-0477(1991)0722.0.CO;2.

[7] B. Schwarz, "LIDAR: Mapping the world in 3D," *Nat. Photonics,* vol. 4, pp. 429-430, 2010. DOI: 10.1038/nphoton.2010.148.

[8] Safety of laser products - Part 1: Equipment classification and requirements, IEC 60825-1:2014, International Electrotechnical Commission, 2014.

[9] A. Samman, L. Rimai, J. R. McBride, R. O. Carter, W. H. Weber, C. Gmachl, F. Capasso, A. L. Hutchinson, D. L. Sivco and A. Y. Cho, "Potential use of near, mid and far infrared laser diodes in automotive LIDAR applications," in *Vehicular Technology Conference Fall 2000. IEEE VTS Fall VTC2000. 52nd Vehicular Technology Conference,* Boston, MA, USA, 2000, pp. 2084-2089.

[10] F. Delorme, S. Grosmaire, A. Gloukhian and A. Ougazzaden, "High power operation of widely tunable 1.55 µm distributed Bragg reflector laser," *Electron. Lett.,* vol. 33, no. 3, pp. 210-211, 1997. DOI: 10.1049/el:19970143.

[11] S. R. Selmic, G. A. Evans, T. M. Chou, J. B. Kirk, J. N. Walpole, J. P. Donnelly, C. T. Harris and L. J. Missaggia, "Single frequency 1550-nm AlGaInAs-InP tapered high-power laser with a distributed Bragg reflector," *IEEE Photon. Technol. Lett.,* vol. 14, no. 7, pp. 890-892, 2002. DOI: 10.1109/LPT.2002.1012375.

[12] A. T. Aho, J. Viheriälä, J. Mäkelä, H. Virtanen, S. Ranta, M. Dumitrescu and M. Guina, "High-power 1550 nm tapered DBR laser diodes for LIDAR applications," in *The European Conference on Lasers and Electro-Optics,* Munich, Germany, 2017, pp. CB_7_4.

[13] A. T. Aho, J. Viheriälä, H. Virtanen, T. Uusitalo and M. Guina, "High-Power 1.5-µm Broad Area Laser Diodes Wavelength Stabilized by Surface Gratings," *IEEE Photon. Technol. Lett.,* vol. 30, no. 21, pp. 1870-1873, 2018. DOI: 10.1109/LPT.2018.2870304.

[14] E. S. Kintzer, J. N. Walpole, S. R. Chinn, C. A. Wang and L. J. Missaggia, "High-power, strained-layer amplifiers and lasers with tapered gain regions," *IEEE Photon. Technol. Lett.,* vol. 5, no. 6, pp. 605-608, 1993. DOI: 10.1109/68.219683.

[15] N. S. Kopeika and J. Bordogna, "Background noise in optical communication systems," *Proc. IEEE,* vol. 58, no. 10, pp. 1571-1577, 1970.

[16] J. Viheriälä, J. Tommila, T. Leinonen, M. Dumitrescu, L. Toikkanen, T. Niemi and M. Pessa, "Applications of UV-nanoimprint soft stamps in fabrication of single-frequency diode lasers," *Microelectron. Eng.,* vol. 86, no. 3, pp. 321-324, 2009. DOI: 10.1016/j.mee.2008.10.010.

[17] A. Knigge, A. Klehr, H. Wenzel, A. Zeghuzi, J. Fricke, A. Maaßdorf, A. Liero and G. Tränkle, "High pulse power wavelength stabilized laser diodes for automotive LiDAR," in *2018 IEEE International Semiconductor Laser Conference (ISLC),* Santa Fe, NM, USA, 2018.

[18] C. Fiebig, B. Eppich, K. Paschke and G. Erbert, "High-Brightness 980-nm Tapered Laser— Optimization of the Laser Rear Facet," *IEEE Photon. Technol. Lett.,* vol. 22, no. 5, pp. 341-343, 2010.

[19] Lasers and laser-related equipment — Test methods for laser beam widths, divergence angles and beam propagation ratios — Part 1: Stigmatic and simple astigmatic beams, ISO 11146-1:2005, International Organization for Standardization, 2005.

[20] M. Mikulla, P. Chazan, A. Schmitt, S. Morgott, A. Wetzel, M. Walther, R. Kiefer, W. Pletschen, J. Braunstein and G. Weimann, "High-Brightness Tapered Semiconductor Laser Oscillators and Amplifiers with Low-Modal Gain Epilayer-Structures," *Photon. Technol. Lett.,* vol. 10, no. 5, pp. 654-656, 1998. DOI: 10.1109/68.669231.

[21] R. J. Lang, A. Hardy, R. Parke, D. Mehuys, S. O'Brien, J. Major and D. Welch, "Numerical Analysis of Flared Semiconductor Laser Amplifiers ," *IEEE J. Quantum Electron.,* vol. 29, no. 6, pp. 2044-2051, 1993. DOI: 10.1109/3.234467.

[22] H. Wenzel, G. Erbert and P. M. Enders, "Improved Theory of the Refractive-Index Change in Quantum-Well Lasers," *IEEE J. Sel. Top. Quantum Electron.,* vol. 5, no. 3, pp. 637-642, 1999. DOI: 10.1109/2944.788429.

# PUBLICATION

# IV

**High-power temperature-stable GaInNAs distributed Bragg reflector laser emitting at 1180 nm**

V.-M. Korpijärvi, J. Viheriälä, M. Koskinen, A. T. Aho and M. Guina

*Optics Letters* 41.4 (2016)
DOI: 10.1364/OL.41.000657

# High-power temperature-stable GaInNAs DBR laser emitting at 1180 nm

VILLE-MARKUS KORPIJÄRVI,[1,*] JUKKA VIHERIÄLÄ,[1] MERVI KOSKINEN,[1] ANTTI T. AHO,[1] MIRCEA GUINA[1]

[1]*Optoelectronics Research Centre (ORC), Tampere University of Technology, P.O. Box 692, FIN-33101, Tampere, Finland*
**Corresponding author: ville-markus.korpijarvi@tut.fi*

Received XX Month XXXX; revised XX Month, XXXX; accepted XX Month XXXX; posted XX Month XXXX (Doc. ID XXXXX); published XX Month XXXX

**We report a single-mode 1180 nm distributed Bragg reflector (DBR) laser diode with a high output power of 340 mW. For the fabrication we employed novel nanoimprint lithography (NIL) that ensures cost-effective, large area, conformal patterning and does not require regrowth. The output characteristic exhibited outstanding temperature insensitivity with a power drop of only 30 % for an increase of the mount temperature from 20 to 80 °C. The high temperature stability was achieved by using GaInNAs/GaAs quantum wells (QWs), which exhibit improved carrier confinement compared to standard InGaAs/GaAs QWs. The corresponding characteristic temperatures were $T_0$=110 K and $T_1$=160K. Moreover, we used a large detuning between the peak wavelength of the material gain at room temperature and the lasing wavelength determined by the DBR. In addition to good temperature characteristics, GaInNAs/GaAs QWs exhibit relatively low lattice strain with direct impact on improving the lifetime of laser diodes at this challenging wavelength range. The single-mode laser emission could be tuned by changing the mount temperature (0.1 nm/°C) or the drive current (0.5 pm/mA). Laser showed no degradation in a room-temperature lifetime test at 900 mA drive-current. These compact and efficient 1180 nm laser diodes are instrumental for the development of compact frequency doubled yellow–orange lasers, which have important applications in medicine and spectroscopy. © 2015 Optical Society of America**

***OCIS codes:*** *(140.2020) Diode lasers; (140.5960) Semiconductor lasers; (140.3570) Lasers, single-mode; (220.3740) Lithography; (230.1480) Bragg reflectors*

http://dx.doi.org/xxx

Many important applications in spectroscopy and medicine, such as treatments of vascular lesions, would benefit from availability of compact semiconductor diode lasers emitting at yellow–orange wavelengths. However, this wavelength range cannot be reached with compact and efficient directly emitting semiconductor lasers typically employed for red wavelengths (GaAs-based compounds) or for blue–green wavelengths (GaN-based materials). Moreover, the frequency doubling approaches, traditionally used for reaching green wavelength range, suffer from the lack of high-power narrow-linewidth frequency stable laser diodes with fundamental emission at 1170 -1200 nm. This is due to the fact that GaInAs/GaAs QWs system would require incorporation of a high amount of In leading to high strain, ultimately generating high amount of defects affecting the laser efficiency and life-time. To cope with this limitation, strain compensation technologies have been employed in external cavity lasers architectures [1, 2] . Recently, strain-compensated GaInAs/GaAs QWs have been used to demonstrate a high power tapered laser diode [3] operating near room temperature. While this recent result is indeed promising, the long-term life-time assessment of such gain structures remains questionable given the high intrinsic strain of the QWs.

Alternatively, 1180 nm wavelength range can be reached using, GaInAs/GaAs QDs [4, 5] or dilute nitrides, i.e. GaInNAs/GaAs QWs [6] . In particular the use of a small amount of N, in the range of 1 %, has been recognized for its benefits related to reduced strain and good carrier confinement enabling demonstration of power levels beyond 10 W in optically pumped vertical-external-cavity surface-emitting lasers (VECSELs) [6] . Adding a small fraction of N to GaInAs can relax the design constraints of the semiconductor structure by avoiding the need for strain compensation and enabling use of higher number of QWs, which could be beneficial for power scaling in integrated amplifiers. The improved carrier confinement translates to improved temperature stability of laser characteristics, a feature that has been recognized since the proposal of GaInNAs/GaAs QWs for uncooled telecom lasers at 1.3 μm [7] . Improved temperature stability is expected to benefit especially miniaturization of frequency-doubled lasers and in general the development of photonic integration approaches, which are currently limited by thermal management issues. For example, ability of lasers to operate at elevated temperatures will reduce the constrains of mounting them close to frequency doubling crystals, which often require elevated operation temperatures [8] .

The single-mode operation with stable wavelength and narrow spectrum, which are essential features for efficient frequency doubling and spectroscopic applications [8] , can be achieved using a distributed

Bragg reflector (DBR) integrated to a narrow ridge waveguide (RWG). To this end, we have developed a process based on using soft stamp UV nanoimprint lithography (NIL) for patterning of the DBR. As compared with other patterning methods (such as electron beam lithography or steppers) NIL is a low-cost and high throughput method, which can imprint features at wafer scale [9].

In this article we report on the NIL-based development of a temperature-stable single-mode GaInNAs/GaAs DBR laser diode emitting an output power as high as 340 mW at 1180 nm. This was enabled by employing GaInNAs/GaAs QW with improved carrier confinement and low intrinsic strain. The highest power reported so far for a DBR laser operating at 1180 nm, without amplifier or tapering, is ~230 mW [10].

The semiconductor structure was grown by plasma-assisted molecular beam epitaxy (MBE) on an n-GaAs(100) substrate and consisted of a single $GaIn_{0.31}N_{0.005}As$ QW embedded in a 1 µm GaAs waveguide surrounded by $Al_{0.25}GaAs$ claddings, as illustrated in Fig. 1. The QW was grown at low temperature of 380 °C in order to kinetically limit phase separation of metastable GaInNAs [11, 12]. We used an excess arsenic pressure corresponding to a beam equivalent pressure ratio of As/III = 14. A high growth rate of 1.4 µm/h was chosen to keep the nitrogen composition low [13]. On the p-side, thinner cladding was used for alleviating possible problems due to high aspect ratio etching of the DBR and to maximize thermal conductivity towards p-contact.

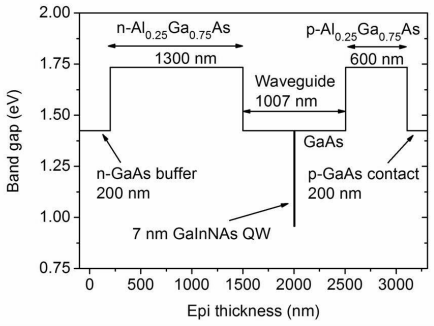


Fig. 1. Semiconductor layer structure grown by plasma-assisted MBE and used for the DBR laser.

In addition to precisely controlled growth conditions, post-growth annealing is of high-importance in GaInNAs device fabrication. Annealing reduces the amount of point defects related to low-temperature growth and nitrogen incorporation and affects nitrogen-induced short range ordering. This improves the luminescence intensity but also induces a blue shift of the emission wavelength. However, the unwanted blue shift is saturable and thus, easily controlled assuming that annealing temperature is not increased above 750 °C [12, 14]. In order to improve material quality for the lasers reported here, we grew three test structures with different annealing temperatures: ~695, ~705 and ~720 °C. The only difference between the test structures and the DBR laser structure was a thinner 900 nm n-AlGaAs cladding used in the test structures. As a result of increased annealing temperature, photoluminescence (PL) intensity of the laser wafers increased by an order of magnitude, and threshold current density of broad area test lasers decreased to one third of the original value (Fig. 2). The best wafer showed PL wavelength of 1173 nm and lasing wavelengths above 1190 nm, which are too high for the targeted 1180 nm DBR laser wavelength. For the DBR laser, we chose an annealing temperature of ~720 °C, fine-tuned the QW emission wavelength by slightly reducing In and N compositions, and increased the n-cladding thickness for suppressing mode-leakage to substrate.

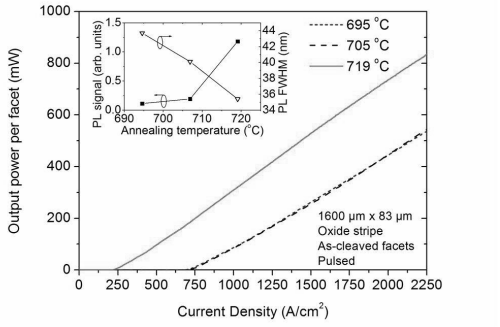


Fig. 2. Output power characteristics of 1600 µm x 83 µm oxide stripe test lasers annealed at different temperatures. Inset shows PL characteristics for the same wafers.

For testing the material characteristics, the heterostructure made for DBR laser was first processed into 83 µm x 1600 µm broad-area oxide stripe lasers without facet coatings. The lasers were mounted p-side up, which leads to poor thermal conductivity from the quantum well region through the substrate to the copper mount. Thus, these lasers were not optimized for high-power continuous wave (CW) operation. Still, they had low threshold current density of 220 A/cm$^2$ and reached maximum output of 1.2 W (0.6 W per as-cleaved facet) in CW mode at driving current of 2.8 A and voltage of 1.4 V. This corresponds to electrical to optical conversion efficiency of 31 % and shows clear improvement as compared with characteristics of InGaAs/GaAs QW lasers at the same wavelength and mounted p-side down for efficient cooling [10]. Lasing wavelength shifted from 1160 nm to 1188 when increasing the driving current from 1 A to 3 A. One reason for the good CW results can be the high thermal stability of the GaInNAs/GaAs QWs. Thermal properties can be characterized by characteristic temperatures $T_0 = \ln(I_{th})/\Delta T$ and $T_1 = \ln(slope)/\Delta T$ describing the exponential increase of threshold current $I_{th}$ and decrease of slope efficiency, respectively, with increasing temperature T. The temperature dependence of the output power in pulsed mode is summarized in Fig. 3; the pulsed mode operation enabled to decouple the thermal behavior of the diodes from the heating related to the use of un-optimized mounting scheme (i.e. p-side up). The determined characteristics temperatures were $T_0$ = 110 K and $T_1$ = 160 K. For comparison, typical $T_0$ values for InGaAs/GaAs QWs with similar wavelength are around 80 K [10, 15]. In fact we measured a $T_0$ = 80 K and $T_1$ = 130 K for our InGaAs/GaAs laser with similar structure but emitting at 1060 nm. Still, it should be noted that regardless of the QW material these values can be improved using higher number of QWs or AlGaAs barriers. Increasing the number of QWs using dilute nitrides should be easier than with GaInAs because of the smaller lattice mismatch. Wavelength of the broad-area lasers shifted at a rate of 0.41 nm/°C and was centered at 1180 nm at a mount temperature of 100 °C. The vertical far field had a full width at half maximum of 43°.

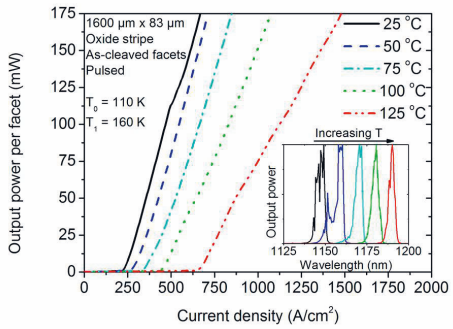


Fig. 3. Peak output power of a broad area laser in pulsed mode and at different mount temperatures. Inset shows output spectra corresponding to different mount temperatures.

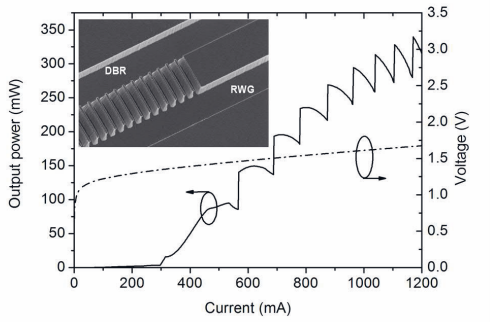


Fig. 4. Current-voltage and light output characteristics of the single-mode 1180 nm DBR laser in CW mode and at mount temperature of 20 °C. Inset shows a scanning electron microscope image taken from a DBR laser.

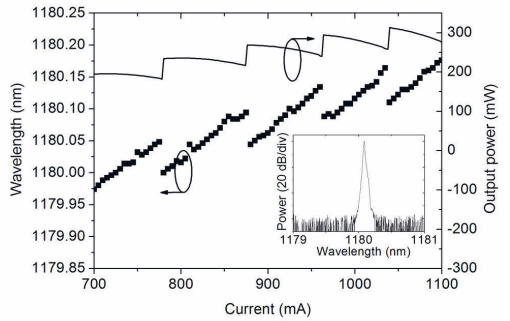


Fig. 5. Wavelength tuning with drive current. Changes between consecutive lasing modes are seen as abrupt changes in wavelength and output power. Inset shows the output spectrum measured at 800 mA.

The DBR laser comprised a 2-mm-long 3rd order DBR section with a reflectivity estimated to be about 15 %. The passive DBR section selected a single longitudinal mode and stabilized the emission wavelength. A 3-mm-long RWG section with a width of 3.2 µm provided gain for lasing in a single transversal mode. DBR and RWG sections were imprinted by soft UV-NIL in one step and etched into semiconductor using inductively coupled plasma (ICP) etching system. Dielectric layer was then deposited on the wafer and removed from top of the ridge waveguide section to define the area where current is injected. P-side metallization (Ti/Pt/Au) was deposited and the wafer was thinned to 150 µm to allow facet cleaving. After thinning, n-metallization (Ni/Au/Ge/Au) was deposited and the metal was annealed to form ohmic contact. Both of the cleaved laser facets were antireflection coated with single layer $Al_2O_3$ for suppressing Fabry-Perot modes and to increase output power from the front facet. Heat extraction from the DBR lasers was improved by mounting them p-side down. Chips were first soldered with AuSn to AlN submount with thermal conductivity of 170 W/mK. Submount was then bonded on a conductively cooled copper mount with indium solder.

The DBR laser was characterized in continuous wave mode at mount temperature of 20 °C. The corresponding characteristics are presented in FIG. 4. Laser had a threshold current of 300 mA and reached a maximum output power of 340 mW, which was measured at a driving current of 1170 mA and forward voltage of 1.67 V (Fig. 4). This corresponds to electrical-to-optical power efficiency of 17 % whereas the maximum efficiency of 20 % was reached at driving current of 876 mA and output power of 269 mW. This record-high output power is an excellent basis for further increase of the output power using a tapered configuration.

Output spectrum of the DBR laser was centered at 1180 nm and had a full width at half maximum (FWHM) of 0.05 nm. The measured spectrum width was likely limited by the resolution of the optical spectrum analyzer (0.05 nm FWHM) used for the measurement. The wavelength could be adjusted at an average rate of 0.5 pm/mA. Tuning was characterized by abrupt changes due to changing of longitudinal lasing mode, which was observed also in the output power (Fig. 5). Between the mode hops, tuning rate was about 1.1 pm/mA. Although tuning was not continuous, emission wavelength could be tuned to any value in the tuning range of the laser owing to overlap between lasing wavelength ranges of consecutive longitudinal modes.

DBR lasers were also measured at different mount temperatures. It was observed that threshold current decreased from 450 mA to 125 mA with increasing temperature from 10 to 50 °C (Fig. 6). This unusual behavior is explained by large detuning between the lasing wavelength and QW gain spectrum. Large detuning is illustrated by amplified spontaneous emission spectrum centered at 1142 nm at 500 mA driving current (inset of Fig. 6). The wavelength tuning rate with temperature was of 0.1 nm/°C. At high current levels output power was relatively insensitive to changes in mount temperature. For example, output powers measured at 1000 mA driving current were 255, 213 and 181 mW for mount temperatures of 20, 50 and 80 °C, respectively. This shows that excellent laser characteristics at high temperatures can be obtained by using high-confinement GaInNAs QWs together with large detuning between lasing wavelength and room-temperature QW gain wavelength.

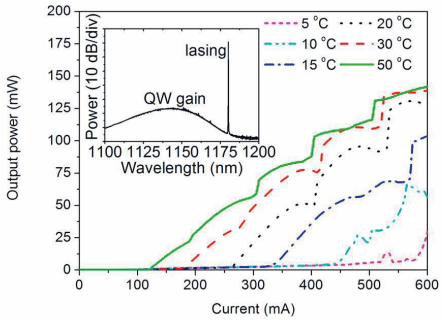


Fig. 6. Output power of DBR laser with respect to driving current measured at different mount temperatures. Inset shows output spectrum at room temperature and current of 500 mA.

A preliminary lifetime test was also carried out by driving the component for 125 hours at 900 mA and mount temperature of 20 °C. Only slight improvement of threshold current and output power were observed after the test.

In conclusion, we have demonstrated an 1180 nm single-mode DBR laser diode with record-high output power of 340 mW. The laser exhibited excellent temperature-stability with only 30 % drop in output power when the mount temperature was increased from 20 to 80 °C. Good high temperature characteristics were enabled by high detuning between lasing wavelength and room-temperature gain wavelength and by temperature-stable GaInNAs/GaAs QWs. Temperature stability of GaInNAs QWs was confirmed by measuring high characteristic temperatures of $T_0$=110 K and $T_1$=160 K for broad area laser diodes without DBR. High-power single-mode operation is important for enabling efficient frequency doubling, whereas good laser operation at elevated temperatures is important for future miniaturization of the frequency-doubled lasers. Next development steps include scaling up the output power by fabricating tapered DBR lasers and demonstration of frequency doubling to yellow–orange wavelengths in compact architectures.

**Funding.** European Commission within the 7th Framework Program projects APACOS and RAPIDO. Project CLEEN funded by the Finnish Agency for Innovation (TEKES).

**Acknowledgment.** Riku Isoaho's assistance in the epitaxy is gratefully acknowledged.

## References

1. S. Ranta, T. Hakkarainen, M. Tavast, J. Lindfors, T. Leinonen, and M. Guina, J. Cryst. Growth 335, 4-9 (2011).
2. S. Ranta, M. Tavast, T. Leinonen, N. Van Lieu, G. Fetzer, and M. Guina, Electronics Letters 49, 59-60 (2013).
3. K. Paschke, F. Bugge, G. Blume, D. Feise, and G. Erbert, Opt. Lett. 40, 100-102 (2015).
4. R. L. Sellin, C. Ribbat, M. Grundmann, N. N. Ledentsov, and D. Bimberg, Appl. Phys. Lett. 78, 1207-1209 (2001).
5. D. Al Nakdali, M. Gaafar, M. Shakfa, F. Zhang, M. Vaupel, K. Fedorova, A. Rahimi-Iman, E. Rafailov, and M. Koch, IEEE Photonics Technology Letters, 27, 1128-1131 (2015).
6. V. Korpijärvi, T. Leinonen, J. Puustinen, A. Härkönen, and M. D. Guina, Optics express 18, 25633-25641 (2010).
7. M. Kondow, T. Kitatani, S. Nakatsuka, M. C. Larson, K. Nakahara, Y. Yazawa, M. Okai, and K. Uomi, IEEE Journal of Selected Topics in Quantum Electronics, 3, 719-730 (1997).
8. A. Jechow, R. Menzel, K. Paschke, and G. Erbert, Laser & Photonics Reviews 4, 633-655 (2010).
9. J. Viheriälä, J. Tommila, T. Leinonen, M. Dumitrescu, L. Toikkanen, T. Niemi, and M. Pessa, Microelectronic Engineering 86, 321-324 (2009).
10. K. Paschke, F. Bugge, G. Blume, D. Feise, W. John, S. Knigge, M. Matalla, H. Wenzel, and G. Erbert, Proc.SPIE 8965, 896509-896509-7 (2014).
11. W. McGee, R. Williams, M. Ashwin, T. Jones, E. Clarke, J. Zhang, and S. Tomić, Physical Review B 76, 085309 (2007).
12. V.-M. Korpijärvi, A. Aho, P. Laukkanen, A. Tukiainen, A. Laakso, M. Tuominen, and M. Guina, J. Appl. Phys. 112, 023504 (2012).
13. A. Aho, V.-M. Korpijärvi, A. Tukiainen, J. Puustinen, and M. Guina, J. Appl. Phys. 116, (2014).
14. M. Hugues, B. Damilano, J. Chauveau, J. Duboz, and J. Massies, Physical Review B 75, 045313 (2007).
15. T. K. Sharma, M. Zorn, F. Bugge, R. Hulsewede, G. Erbert, and M. Weyers, IEEE Photonics Technology Letters, 14, 887-889 (2002).